Hybrid and Monolithic Active Quasi-Optical Grids

Thesis by

Michael Peter De Lisio

In Partial Fulfillment of the Requirements

for the Degree of

Doctor of Philosophy

California Institute of Technology

Pasadena, California

1996

(Submitted December 8, 1995)

To my Family, Old and New

Acknowledgements

First and foremost, I would like to thank my advisor, David Rutledge, for his guidance, support, advice, and patience. I feel both honored and privileged to have been a part of his research group.

My stay at Caltech was funded by fellowships from the National Science Foundation and the Army Research Office, for which I am grateful. The Lockheed Martin Corporation also supported much of this work, most notably through several generous fabrication runs at their Baltimore Labs. I would especially like to thank Sandy Weinreb, Scott Duncan, Erich Schlecht, and Norm Byer. In addition, Peter Smith at JPL and Mark Rodwell at UCSB deserve thanks for providing the impetus behind the tunnel diode grid project.

I have had the opportunity to work with many talented people in the MMIC group at Caltech. But it is their camaraderie, rather than their ability, that I treasure the most. I owe a lot to Gabriel Rebeiz—it was through his urging that I came to Caltech in the first place. I want to thank Kent Potter for his skillful technical help, which leads one to wonder if there is anything he cannot do. Irene Loera also deserves thanks for the many last-minute requests and birthday parties. David Haub made that difficult first year much more pleasant. Yong Guo and Scott Wedge provided valuable advice and an "existence proof" that graduation is indeed possible. I will always remember the many hiking and ski trips with my "absent friends," Phil Stimson and Bobby Weikle, and I look forward to many more to come. Moonil Kim made my early years more enjoyable and also laid much of the groundwork for the research presented here. I have met two of my best friends through this group: Jon Hacker and Victor Lubecke. Jon's unerring technical ability coupled with his razor wit always kept things interesting. Victor is one of those rare people who puts others before himself, and I'm thankful for all his help, especially for assisting with our computer network. I've had five years to cultivate my friendship with Jung-Chih Chiao, who is one

of the kindest people I've ever met. I'm also happy to have met Alina Mousessian, and I will fondly remember our many late night philosophical discussions. Shi-Jie Li's quiet diligence, gentle humor, and class notes are much appreciated. Cheh-Ming Liu masterminded the automated data acquisition setup, which made my life much easier. I'd like to thank the newer members of the group, Polly Preventza and John Davis, and wish them all the best in the new building. I am fortunate to have had the opportunity of meeting and working with the many visitors to the MMIC group, including Erik Kolberg, Ashley Robinson, and Minoru Saga. Finally, I'd like to thank Jim Rosenberg, MMIC group member by association, for all his suggestions, advice, and interesting conversation.

There are many others whose friendship I am grateful for, including Olga Borić-Lubecke, the entire Stimson family, and (R)Andal Salvatore, who deserves an award for the most tolerant roommate. Finally, I want to express my gratitude to my family, to whom this thesis is dedicated, both "old"—my parents, Michael and Rita, and my sister, Suzanne—and "new"—my wife, Lisa. If anything has made this endeavor possible, it has been their support, understanding, and love.

We must keep repeating to ourselves that, at no time and in no place, will nature ever ask for our permission.

—Fyodor Dostoyevsky, Notes from Underground, 1864

In philosophy, or religion, or ethics, or politics, two and two might make five, but when one was designing a gun or an airplane they had to make four.

—George Orwell, 1984, 1949

Hybrid and Monolithic Active Quasi-Optical Grids

Abstract

Quasi-optical grids combine the output powers of many solid-state sources in free space, eliminating the conductor losses associated with traditional waveguide or transmission-line combiners. This approach shows most promise at millimeter-wave frequencies, where the outputs of thousands of devices could potentially be combined through wafer-scale integration. This thesis will detail three separate active quasi-optical grids. The first grid is a 16-element hybrid tunnel diode oscillator. This grid achieved a locked output frequency spectrum, with a peak Effective Radiated Power (ERP) of 1.3 mW at 1.9 GHz. This grid is a prototype for monolithic Resonant Tunneling Diode (RTD) grid oscillators, designed to operate from 200 to 500 GHz. The second grid is a 100-element hybrid pseudomorphic High Electron Mobility Transistor (pHEMT) amplifier. Modelling techniques, design procedure, and experimental results will be presented. This grid has a peak gain of 12 dB at 9 GHz, with a 15% 3-dB bandwidth. The output power, 3.7 W, increases with the number of devices, while the noise figure, 3 dB, is similar to that of a single device. The third grid is a 36-element monolithic pHEMT amplifier. This grid has a peak gain of 6.5 dB at 44 GHz. By changing the positions of external polarizers and slabs, the grid can be tuned to operate up to 60 GHz with 2.5 dB gain. In addition, theoretical discussions of two topics relevant to active grids will be discussed. The first is a technique employing the method of moments and the induced emf technique to determine the electromagnetic properties of periodic grating structures. The second explores some thermal properties of quasi-optical grids.

Contents

Chapter 1

Introduction

Microwaves (1–30 GHz), unlike optical and infrared waves, have the ability to penetrate fog, dust, and smoke. To a certain extent, millimeter-waves (30–300 GHz) share this property, but their shorter wavelength allows for greatly reduced equipment and antenna size. For these reasons, the military has long been interested in developing these technologies. Much of the pioneering microwave research was performed while developing radar during World War II. The Department-of-Defense-sponsored MMIC program has fueled the recent rapid development of millimeter-wave technology—integrated circuits operating over 94 GHz are readily available today. Applications include passive and active imaging systems, fire-control radar, friend-or-foe identification, and seekers for smart weapons.

Traditionally, commercial applications have accounted for only a small fraction of the high-frequency market. Over the past few years, however, this has changed dramatically. The commercial and consumer market has experienced tremendous growth. Avenues being explored include automotive radar and collision-avoidance systems, wireless local area networks, personal communication systems, and inclement weather landing and navigational aids for aircraft and ships [1–3]. No less than six multi-user satellite communication systems offering voice, data, fax, and video services have been proposed or are being developed, with a total estimated cost of over 15 billion dollars [4].

For both military and consumer applications, there is a need for low-cost, reliable sources with reasonable power-handling capability. Quasi-optics is a possible way to achieve this goal.

1.1. Quasi-Optical Power Combining

Fig. 1.1 shows the power-handling capability versus frequency for a number of solid-state and vacuum-tube sources. Vacuum devices are clearly more powerful, but their bulkiness and expense limit their application. Furthermore, they often require high-voltage power supplies and large cooling apparatus. Solid-state sources would be more attractive, but often a single device is incapable meeting the system power requirements. To overcome this, the outputs of many devices must be added together.

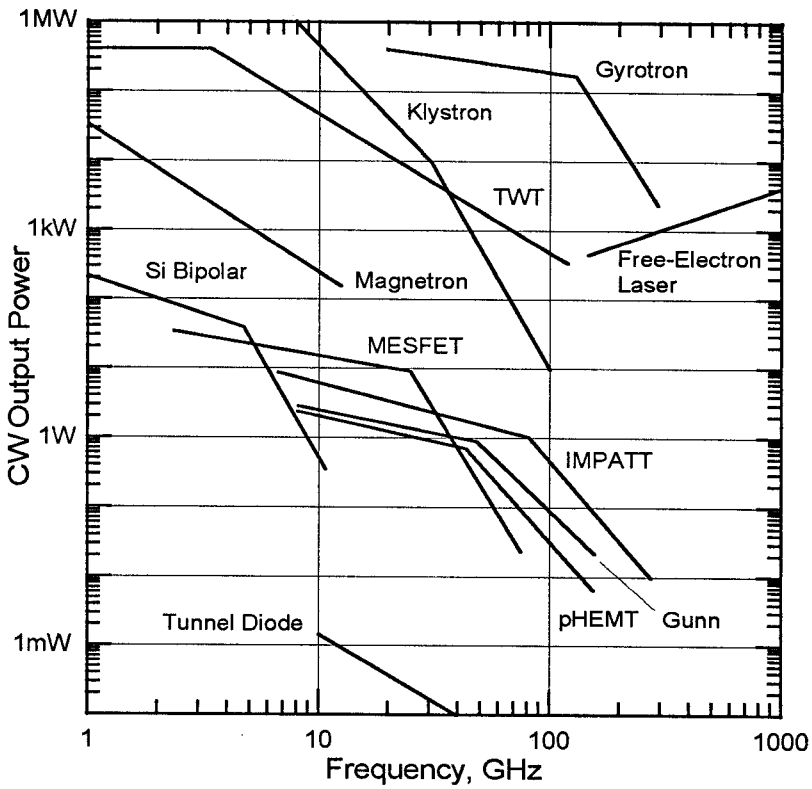

Fig. 1.1. Comparison of output power versus frequency for various microwave and millimeter-wave sources. Data collected from [5–7].

Power combining is typically done using resonant waveguide cavities or transmission-line feed networks [8]. These approaches, however, have a number of shortcomings that become especially apparent at higher frequencies. First, conductor losses in the waveguide walls or transmission lines tend to increase with frequency, eventually limiting the combining efficiency. Second, these combiners become increasingly difficult to machine as the wavelength gets smaller. Third, in waveguide systems, each device often must be inserted and tuned manually. This is labor-intensive and only practical for a relatively small number of devices. In what has become a classic paper, James Mink proposed quasi-optics as an elegant solution [9]. An array of millimeter-wave sources placed in a resonator could synchronize to the same frequency and phase, not unlike what happens in a laser. Their outputs would add in free space, minimizing conductor losses. Furthermore, a planar array could be fabricated monolithically; at shorter wavelengths, thousands of devices could be incorporated on a single wafer.

A number of quasi-optical devices have been developed, including detectors [10], multipliers [11,12], mixers [13], and phase shifters [14,15]. These passive devices continue to be the subject of ongoing research. Over the past five years, however, *active* quasi-optical devices—namely oscillators and amplifiers—have evolved. Active quasi-optics has attracted considerable attention in a short time, and the growth of the field has been explosive.

1.2. Grid Oscillators

Grid oscillators developed at Caltech were among the first active quasi-optical power combiners. A grid oscillator is a planar periodic array of closely-spaced solid-state sources, as shown in Fig. 1.2. When behaving properly, these devices will lock together in frequency and phase, producing a well-polarized beam of coherent radiation. The mirror provides feedback to help synchronize

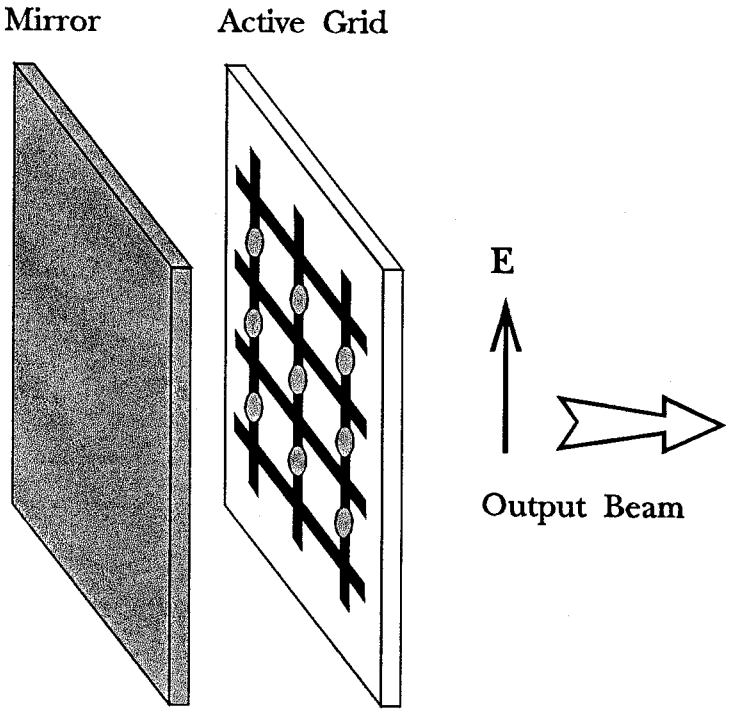

Fig. 1.2. A grid oscillator. The grid is a planar periodic array of microwave or millimeter-wave active devices.

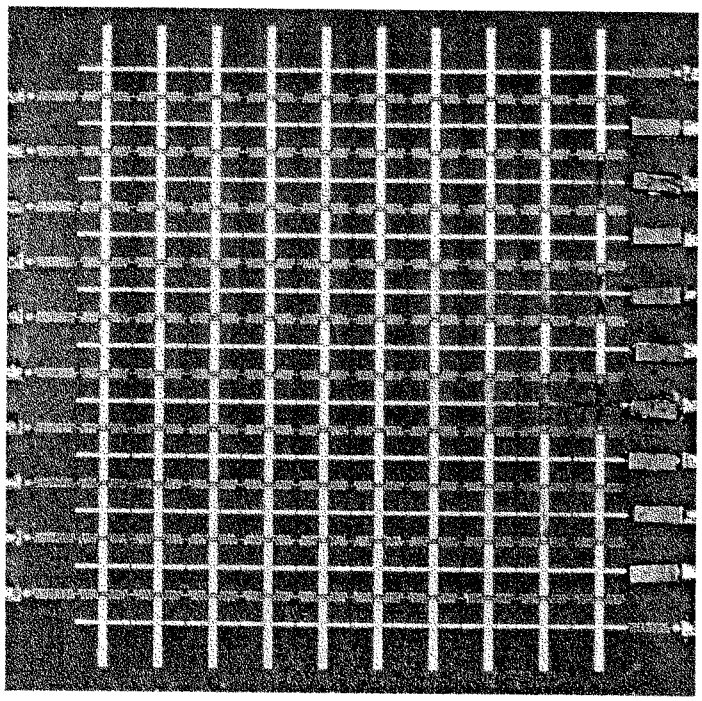

Fig. 1.3. Photograph of the 100-MESFET 10 W X-band oscillator grid developed by J.B. Hacker at Caltech [19].

the individual elements and directs the output beam forward. The oscillation frequency is primarily determined by the spacing between devices, while the power scales with the total number of devices incorporated.

The first successful grid was a 25-MESFET oscillator, tested by Popović, Kim, and Rutledge [16]. This grid radiated 460 mW at 9.7 GHz. Several other grids soon followed [17,18], with the most recent being a high-power hybrid grid [19]. This grid, shown in Fig. 1.3, incorporated 100 MESFET's and produced 10.3 W at 9.8 GHz. A tremendous variety of grids as well as other types of quasi-optical oscillators have been successful, employing a number of different active devices. Professor R.A. York at the University of California at Santa Barbara has written an excellent review describing many of these active arrays [20].

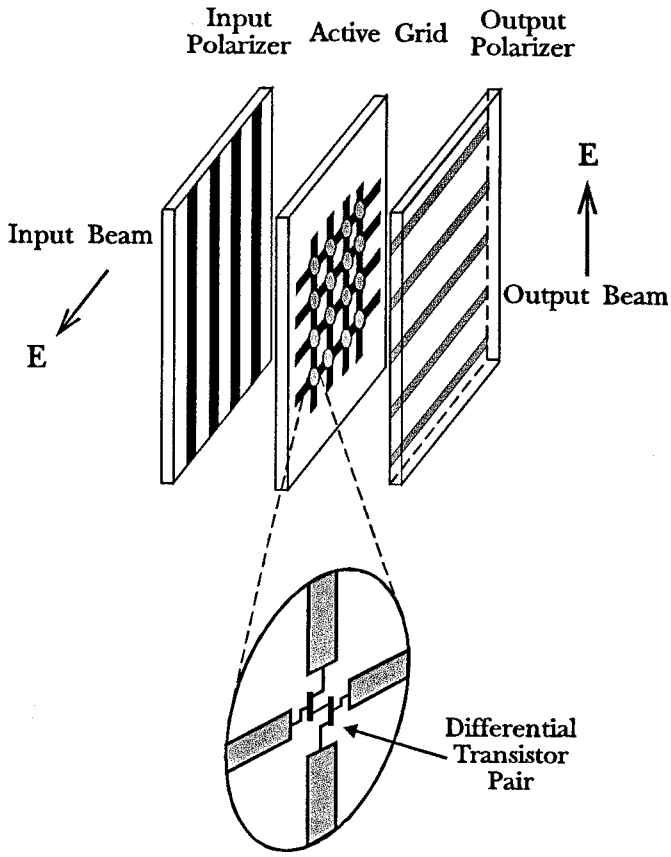

Fig. 1.4. A grid amplifier. Metal strip polarizers independently tune the input and output.

1.3. Grid Amplifiers

Much of today's quasi-optical research has shifted to the study of amplifiers. The first quasi-optical amplifier was a grid developed by M. Kim *et al.* at Caltech [21]. This grid used 25 MESFET pairs, demonstrating a gain of 11 dB at 3.3 GHz. A grid amplifier, as shown in Fig. 1.4, is an array of closely-spaced differential pairs of transistors. A horizontally polarized input beam, incident from the left, excites rf currents on the horizontal leads of the grid. These currents drive the inputs of the transistor pair in the differential mode. The output currents are redirected along the grid's vertical leads, producing a vertically polarized output beam to the right. The cross-polarized input and output has two important advantages. First, it provides good input-output isolation, reducing the potential for spurious feedback oscillations. Second, the amplifier's input and output circuits can be independently tuned using metal-strip polarizers, which also confine the beam to the forward direction. A 100-element HBT grid soon followed [22].

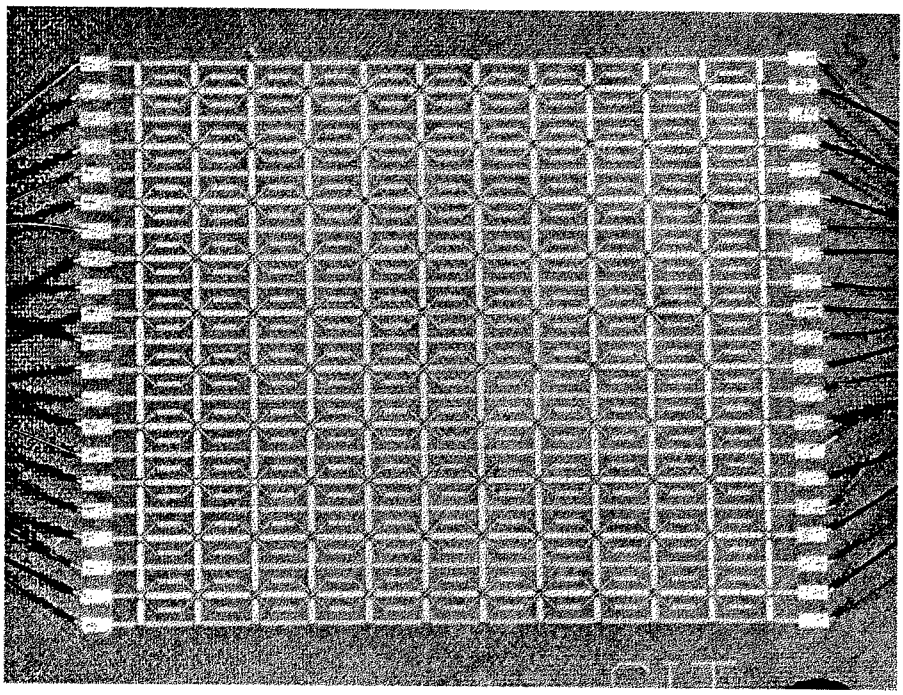

Fig. 1.5. Photograph of the 100-element HBT grid built and tested by M. Kim [22].

Reference	# of Cells	Devices	Type	Freq. (GHz)	Gain (dB)	B.W. (%)	N.F. (dB)	Power (W)
[21]	25	MESFET Diff. Pair	Hybrid Grid	3.3	11	2.7	—	—
[22]	100	HBT Diff. Pair	Hybrid Grid	10	10	10	7	0.45
[25]	1	MESFET Pair	Probe-Probe	4	12	3.5	—	—
[34]	16	MESFET	Folded slot-Folded slot	4.2	5	8	—	—
[24]	1	pHEMT MMIC	Back-to-Back Etched Horn	102	15.5	~ 4	7.4	—
[28]	9	HEMT	Patch-Patch	10.9	5.5	9.2	—	—
[35]	16	HBT MMIC	Folded Slot-Folded Slot	11	8	4	—	—
[30]	9	2-stage HEMT	Patch-Patch	10	18	~ 3	—	—
[32]	24	MESFET	Patch-Patch	10	10.4	—	—	0.7
[32]	6	2-stage pHEMT	Folded Slot-Slot	9.5	9.8	~ 4	2.2	—
[36]	9	MESFET MMIC	Slot-Slot	29	6	1.5	—	1
[37] [Chapter 3]	100	pHEMT Diff. Pair	Hybrid Grid	9	12	15	3	3.7
[33]	2×9	HEMT	2 Cascaded Patch-Patch	10	13	~ 4	—	—
[39]	28	HBT MMIC	Monolithic Slot-Patch	50	~ 1	—	—	—
[41]	36	HBT Diff. Pair	Monolithic Grid	40	5	4.5	—	0.67
[42] [Chapter 4]	36	pHEMT Diff. Pair	Monolithic Grid	44–60	2.5–6.5	6	—	—

Table 1.1. Examples of quasi-optical amplifiers. Tabulated performance characteristics are: operating frequency, peak gain, percent bandwidth, noise figure, and output power.

This grid is shown in Fig. 1.5. The gain was 10 dB at 10 GHz, with a 10% 3-dB bandwidth. The noise figure was 7 dB, and the output power was 450 mW. Both gain and noise figure are similar to that of a single device, while the output power increases with the total number of devices.

Based on the success of these original grids, a number of other types of quasi-optical amplifiers have been developed. The approaches vary. Amplifiers using back-to-back integrated horn antennas [23,24], probe antennas [25], patch antennas [26–33], and slot antennas [34–36] have been successfully demonstrated. Progress in grid amplifiers has also continued [37,38]. The first monolithic quasi-optical amplifier has been demonstrated by Rockwell International [39], but the gain was limited. Very recently, monolithic grid amplifiers have demonstrated appreciable gain and power at millimeter-wave frequencies [40–42]. The performance of some notable quasi-optical amplifiers is summarized in Table 1.1.

1.4. Organization of the Thesis

The bulk of this thesis details three distinct active grids. The first, described in Chapter 2, is a 16-element hybrid tunnel diode oscillator grid. Design, experimental results, and motivation will be discussed. A locked frequency spectrum was achieved, with a peak Effective Radiated Power (ERP) of 1.3 mW at 1.9 GHz. This is the first grid oscillator using broadband negative differential resistance devices. This grid is a prototype for future monolithic grids using Resonant Tunneling Diodes (RTD's). Designs of several RTD grids from 200 to 500 GHz will be presented.

Chapter 3 discusses a 100-element hybrid amplifier grid. The grid uses pseudomorphic High Electron Mobility Transistors (pHEMT's) as the active devices. The pHEMT differential pair chips were custom fabricated by Lockheed Martin Laboratories, Baltimore. A simple transmission-line model useful for predicting

gain will be introduced. This grid achieved a 12-dB gain at 9 GHz with a 15% bandwidth. The measured noise figure was 3 dB and the saturated output power was 3.7 W. Gain, input and output tuning, and angular dependence will be shown to be consistent with theoretical predictions.

In Chapter 4, a 36-element monolithic pHEMT grid amplifier will be detailed. These grids were also fabricated by Lockheed Martin Laboratories. First iteration grids produced limited gain. A second iteration grid was designed, with greatly reduced parasitic source inductance. These grids demonstrated 6.5 dB of gain at 44 GHz. Simply by changing the positions of external polarizers and tuning elements, the grid could operate up to 60 GHz with 2.5 dB gain.

The subject of Chapter 5 is directions for future research in active quasi-optical power combining.

Appendix A outlines the technique used throughout the thesis to model the electromagnetic properties of gratings and periodic structures. This approach combines the method of moments with the induced emf method.

Appendix B investigates some thermal properties of active arrays, which will become important for future applications.

References

[1] G.C. DiPiazza, "Dual-Use and Defense Conversion: A View from the Second Tier," *1995 IEEE MTT-S Int. Microwave Symp. Dig.*, pp. 1059–1062, 1995.

[2] H.H. Meinel, "Commercial Applications of Millimeterwaves History, Present Status, and Future Trends," *IEEE Trans. Microwave Theory Tech.*, vol. 43, pp. 1639–1653, July 1995.

[3] P.F. Goldsmith, C.-T. Hsieh, G.R. Huguenin, J. Kapitzky, E.L. Moore, "Focal Plane Imaging Systems for Millimeter Wavelengths," *IEEE Trans. Microwave Theory Tech.*, vol. 41, pp. 1664–1675, Oct. 1993.

[4] F. Ali, J.B. Horton, "Introduction to Special Issue on Emerging Commercial and Consumer Circuits, Systems, and Their Applications," guest editor's introduction, *IEEE Trans. Microwave Theory Tech.*, vol. 43, pp. 1633–1638, July 1995.

[5] K.J. Sleger, R.H. Abrams, Jr., R.K. Parker, "Trends in Solid-State Microwave and Millimeter-Wave Technology," *IEEE MTT-S Newsletter*, no. 127, pp. 11–14, Fall 1990.

[6] D.M. Pozar, *Microwave Engineering*, Adison-Wesley Publishing Co., Inc., Reading, MA, 1990, pp. 651–660.

[7] S.M. Sze, *Physics of Semiconductor Devices*, second ed., John Wiley & Sons, Inc., New York, 1981, pp. 513–678.

[8] K. Chang, C. Sun, "Millimeter-Wave Power Combining Techniques," *IEEE Trans. Microwave Theory Tech.*, vol. 31, pp. 91–107, Feb. 1983.

[9] J.W. Mink, "Quasi-Optical Power Combining of Solid-State Millimeter-Wave Sources," *IEEE Trans. Microwave Theory Tech.*, vol. 34, pp. 273–279, Feb. 1986.

[10] D.B. Rutledge, S.E. Schwarz, "Planar Multimode Detector Arrays for Infrared and Millimeter-Wave Applications," *IEEE J. Quantum Electronics*, vol. 17, pp. 407–414, March 1981.

[11] H-.X.L. Liu, L.B. Sjogren, C.W. Domier, N.C. Luhmann, Jr., D.L. Sivco, A.Y. Cho, "Monolithic Quasi-Optical Frequency Tripler Array with 5-W Output Power at 99 GHz," *IEEE Electron Device Lett.*, vol. 14, pp. 329–331, July 1993.

[12] J.-C. Chiao, A. Markelz, Y. Li, J. Hacker, T. Crowe, J. Allen, D.B. Rutledge, "Terahertz Grid Frequency Doublers," presented at *The 6th Int. Symp. Space Terahertz Tech.*, March 1995.

[13] J.B. Hacker, R.M. Weikle, M. Kim, M.P. De Lisio, D.B. Rutledge, "A 100-Element Planar Schottky Diode Grid Mixer," *IEEE Trans. Microwave Theory Tech.*, vol. 40, pp. 557–562, March 1992.

[14] W.W. Lam, H.Z. Chen, K.S. Stolt, C.F. Jou, N.C. Luhmann, Jr., D.B. Rutledge, "Millimeter-Wave Diode Grid Phase Shifters," *IEEE Trans. Microwave Theory Tech.*, vol. 36, pp. 902–907, May 1988.

[15] L.B. Sjogren, H.-X.L. Liu, X.-H. Qin, C.W. Domier, N.C. Luhmann, Jr., "Phased Array Operation of a Diode Grid Impedance Surface," *IEEE Trans. Microwave Theory Tech.*, vol. 42, pp. 565–572, April 1994.

[16] Z.B. Popović, M. Kim, D.B. Rutledge, "Grid Oscillators," *Int. J. Infrared Millimeter Waves*, vol. 9, pp. 647–654, July 1988.

[17] Z.B. Popović, R.M. Weikle, M. Kim, D.B. Rutledge, "A 100-MESFET Planar Grid Oscillator," *IEEE Trans. Microwave Theory Tech.*, vol. 39, pp. 193–200, March 1990.

[18] R.M. Weikle, M. Kim, J.B. Hacker, M.P. De Lisio, D.B. Rutledge, "Planar MESFET Grid Oscillators Using Gate Feedback," *IEEE Trans. Microwave Theory Tech.*, vol. 40, pp. 1997–2003, Nov. 1992.

[19] J.B. Hacker, M.P. De Lisio, M. Kim, C.-M. Liu, S.-J. Li, S.W. Wedge, D.B. Rutledge, "A 10-Watt X-Band Grid Oscillator," *1994 IEEE MTT-S Int. Microwave Symp. Dig.*, pp. 823–826, 1994.

[20] R.A. York, "Quasi-Optical Power Combining Techniques," in *Millimeter and Microwave Engineering for Communications and Radar*, J.C. Wiltse, ed., Critical Reviews of Optical Science and Technology, vol. CR54, pp. 63–97.

[21] M. Kim, J.J. Rosenberg, R.P. Smith, R.M. Weikle, J.B. Hacker, M.P. De Lisio, D.B. Rutledge, "A Grid Amplifier," *IEEE Microwave Guided Wave Lett.*, vol. 1, pp. 322–324, Nov. 1991.

[22] M. Kim, E.A. Sovero, J.B. Hacker, M.P. De Lisio, J.-C. Chiao, S.-J. Li, D.R. Gagnon, J.J. Rosenberg, D.B. Rutledge, "A 100-Element HBT Grid Amplifier," *IEEE Trans. Microwave Theory Tech.*, vol. 41, pp. 1762–1771, Oct. 1993.

[23] C.-Y. Chi, G.M. Rebeiz, "A Quasi-Optical Amplifier," *IEEE Microwave Guided Wave Lett.*, vol. 3, pp. 164–166, June 1993.

[24] T.P. Budka, M.W. Trippe, S. Weinreb, G.M. Rebeiz, "A 75 GHz to 110 GHz Quasi-Optical Amplifier," *IEEE Trans. Microwave Theory Tech.*, vol. 42, pp. 899–901, May 1994.

[25] N. Kolias, R.C. Compton, "A Microstrip-Based Unit Cell for Quasi-Optical Amplifier Arrays," *IEEE Microwave Guided Wave Lett.*, vol. 3, pp. 330–332, Sept. 1993.

[26] T. Mader, J. Schoenberg, L. Harmon, Z.B. Popović, "Planar MESFET Transmission Wave Amplifier," *Electronics Lett.*, vol. 29, pp. 1699–1701, Sept. 1993.

[27] H.S. Tsai, R.A. York, "Polarisation-Rotating Quasioptical Reflection Amplifier Cell," *Electronics Lett.*, vol 29, pp. 2125–2127, Nov. 1993.

[28] N. Sheth, T. Ivanov, A. Balasubramaniyan, A. Mortazawi, "A Nine HEMT Spatial Amplifier," *1994 IEEE MTT-S Int. Microwave Symp. Dig.*, pp. 1239–1242, 1994.

[29] J.S.H. Schoenberg, S.C. Bundy, Z.B. Popović, "Two-Level Power Combining Using a Lens Amplifier," *IEEE Trans. Microwave Theory Tech.*, vol. 42, pp. 2480–2485, Dec. 1994.

[30] T. Ivanov, A. Mortazawi, "Two Stage Double Layer Microstrip Spatial Amplifiers," *1995 IEEE MTT-S Int. Microwave Symp. Dig.*, pp. 589–592, 1995.

[31] J. Schoenberg, T. Mader, B. Shaw, Z.B. Popović, "Quasi-Optical Antenna Array Amplifiers," *1995 IEEE MTT-S Int. Microwave Symp. Dig.*, pp. 605–608, 1995.

[32] J.S.H. Schoenberg, T.B. Mader, J.W. Dixon, B.L. Shaw, Z.B. Popović, "Quasi-Optical Antenna Array Amplifiers," submitted to *IEEE Trans. Microwave Theory Tech.*, March 1995.

[33] T. Ivanov, A. Balasubramaniyan, A. Mortazawi, "One- and Two-Stage Spatial Amplifiers," *IEEE Trans. Microwave Theory Tech.*, vol. 43, pp. 2138–2143, Sept. 1995.

[34] H.S. Tsai, M.J.W. Rodwell, R.A. York, "Planar Amplifier Array With Improved Bandwidth Using Folded-Slots," *IEEE Microwave Guided Wave Lett.*, vol. 4, pp. 112–114, April 1994.

[35] H.S. Tsai, R.A. York, "Quasi-Optical Amplifier Array using Direct Integration of MMICs and 50 Ω Multi-Slot Antennas," *1995 IEEE MTT-S Int. Microwave Symp. Dig.*, pp. 593–596, 1995.

[36] J. Hubert, J. Schoenberg, Z.B. Popović, "High-Power Hybrid Quasi-Optical Ka-Band Amplifier Design," *1995 IEEE MTT-S Int. Microwave Symp. Dig.*, pp. 585–588, 1995.

[37] M.P. DeLisio, S.W. Duncan, D.-W. Tu, C.-M. Liu, A. Moussessian, J.J. Rosenberg, D.B. Rutledge, "Modelling and Performance of a 100-Element pHEMT Grid Amplifier," submitted to *IEEE Trans. Microwave Theory Tech.*, April 1995.

[38] C.-M. Liu, E.A. Sovero, M.P. DeLisio, A. Moussessian, J.J. Rosenberg, D.B. Rutledge, "Gain and Stability Models for HBT Grid Amplifiers," *1995 IEEE AP-S Int. Symp. Dig.*, pp. 1292–1295, 1995.

[39] J.A. Higgins, E.A. Sovero, W.J. Ho, "44-GHz Monolithic Plane Wave Amplifiers," *IEEE Microwave Guided Wave Lett.*, vol. 5, pp. 347–348, Oct. 1995.

[40] C.-M. Liu, E.A. Sovero, W.J. Ho, J.A. Higgins, D.B. Rutledge, "A Millimeter-Wave Monolithic Grid Amplifier," to appear in *Int. J. Infrared Millimeter Waves*, vol. 16, Nov. 1995.

[41] C.-M. Liu, E.A. Sovero, W.J. Ho, J.A. Higgins, M.P. De Lisio, D.B. Rutledge, "Monolithic 40-GHz 670-mW HBT Grid Amplifier," submitted to *1996 IEEE MTT-S Int. Microwave Symp.*, Oct. 1995.

[42] M.P. De Lisio, S.W. Duncan, D.-W. Tu, S. Weinreb, C.-M. Liu, D.B. Rutledge, "A 44-60 GHz Monolithic pHEMT Grid Amplifier," submitted to *1996 IEEE MTT-S Int. Microwave Symp.*, Oct. 1995.

Chapter 2

Tunnel Diode Oscillator Grid

This chapter details the design, construction, and performance of a tunnel diode oscillator grid. Intended to serve as a prototype for future monolithic grids using Resonant Tunneling Diodes (RTD's), this grid is a hybrid construction of sixteen germanium tunnel diodes. The grid was designed to operate at 2.3 GHz. A locked output frequency spectrum was achieved, with a peak Effective Radiated Power (ERP) of 1.3 mW at 1.9 GHz. Spurious bias line oscillations were suppressed using ferrite material. The average Single-Sideband (SSB) noise level was −76 dBc/Hz at an offset of 100 kHz. The radiation patterns were measured and will be presented. In addition, frequency components were observed at multiples of one-third of the main frequency, but at power levels at least 16 dB lower. This is the first oscillator grid using broadband negative differential resistance devices.

2.1. Motivation and Design Goals

For several years, NASA and other space agencies have been developing sensitive submillimeter and Terahertz receivers, operating from 300 GHz to 3 THz. These instruments are necessary for the study of astrophysical phenomena, such as star and galaxy formation, as well as for the study of our Earth's atmosphere and the depletion of the ozone layer [1–6]. An integral component of these receivers is the local oscillator. This oscillator pumps the mixer in a heterodyne system, and it must provide a clean, stable signal if the system is to perform

optimally. Furthermore, for many of the proposed missions, the local oscillator must be capable of providing milliwatt-level power as high as 3 THz.

Generation of power at these frequencies is difficult. A conventional approach is to use a series of Schottky diode multipliers to upconvert the output of a Gunn diode oscillator [7]. If a single multiplier diode is unable to provide enough power, a quasi-optical multiplier array can combine the powers of many devices—a 36-element doubler grid has demonstrated 330 μW at 1 THz [8]. This is the highest reported output power for a solid-state multiplier at 1 THz. Unfortunately, the multiplier chains necessary in this approach can become quite complicated. Vacuum tubes and free-electron lasers can directly generate power at these frequencies, but suffer from serious drawbacks. Vacuum devices are capable of providing substantial power, but their size, weight, and need for high-voltage power supplies limit their utility, especially for spaceborne applications. Similarly, the cost and complexity of free-electron lasers are severely prohibitive, limiting their use to large research institutions. An alternative approach is to use a photo-mixer to heterodyne the optical or infrared outputs of two lasers, generating a THz-level beat frequency. This technique has been demonstrated up to 3.8 THz [9]. The approach shows great promise, but so far the output powers have been low—on the order of 0.1 μW at 1 THz—and it is unclear if the available lasers are suitable for spacecraft operation.

The lack of a solid-state device capable of directly generating useful power at these frequencies has been problematic. The development of the Resonant Tunneling Diode (RTD) may offer a solution. The RTD is a quantum-well heterostructure that exhibits negative differential resistance, which enables it to generate rf power. E.R. Brown and co-workers have observed oscillations up to 420 GHz in GaAs/AlAs RTD's [10], and up to 712 GHz in InAs/AlSb devices [11], making the RTD the world's fastest room temperature solid-state electronic device. Fig. 2.1 illustrates the performance of these RTD's. Even higher oscil-

lation frequencies have been projected [12,13] by replacing the ohmic contact at the collector of a conventional RTD with a Schottky contact. Preliminary dc and microwave measurements of a Schottky-collector AlAs/InGaAs/InP RTD indicate a maximum frequency of oscillation, f_{max}, of 2.2 THz [14].

Unfortunately, the output powers of RTD's are quite low, as seen in Fig. 2.1. In order to make a submillimeter or Terahertz source with RTD's, the outputs of many devices must be combined. A two-element RTD resonant waveguide combiner has been demonstrated at 75 GHz [15]. For reasons discussed in the first chapter, however, this approach has a number of limitations, especially at higher frequencies. Another approach involves connecting several devices in series [16,17]. This approach has potential, but requires an rf drive signal to initiate the oscillation. Quasi-optical power combining is an attractive alternative.

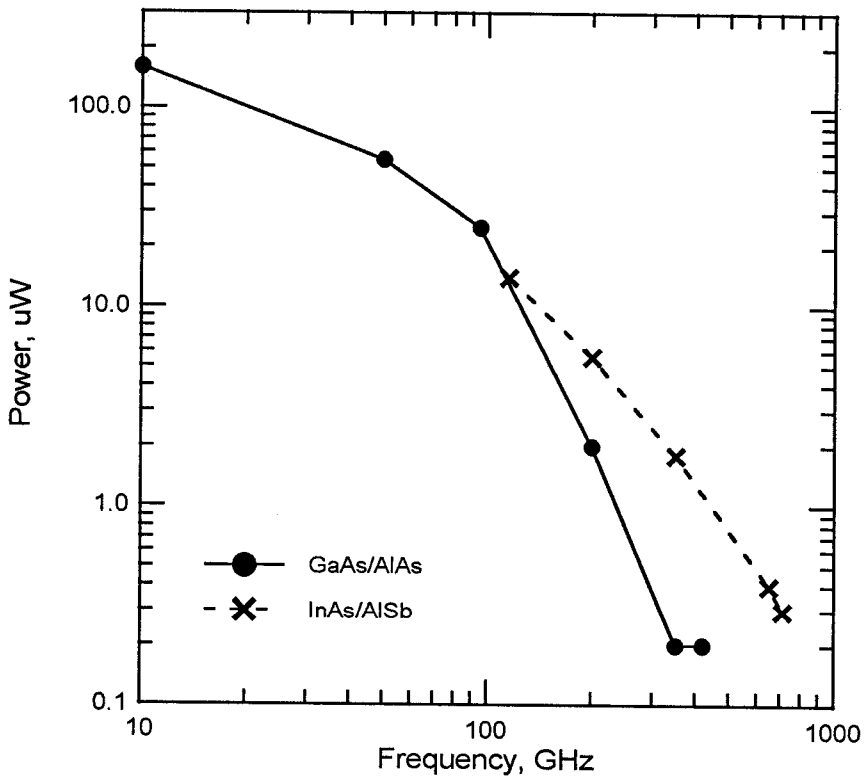

Fig. 2.1. State of the art RTD performance. The GaAs/AlAs diode has a 4-μm diameter [8]. The InAs/AlSb device has a diameter of 1.8 μm [9].

Low output power is one of the limitations of the the RTD. Another, possibly more serious one, is the broadband nature of the device's Negative Differential Resistance (NDR). An RTD circuit is capable of oscillating anywhere from dc up to the maximum oscillation frequency, f_{max}. The designer of an RTD oscillator has to be extremely vigilant that the circuit is only unstable where intended. Often, the design will be plagued by low-frequency oscillations in the bias circuitry. These spurious bias-circuit instabilities are notorious and well-documented [18,19].

The goal of this project was to design and build a grid oscillator of broadband NDR devices. Testing of this grid would determine whether submillimeter or Terahertz RTD grids are feasible. Due to the lack of readily-available RTD's, germanium tunnel diodes were used as the active devices. Tunnel diodes, like RTD's, are broadband NDR devices, but their operating frequencies are much lower—their f_{max} is typically less than 100 GHz. These devices were invented in 1957 by Leo Esaki [20,21], for which he shared the 1973 Nobel Prize for Physics. Tunnel diodes have been widely used for a number of applications, although today, the development of Gunn and IMPATT diodes and, more recently, GaAs transistors has made them almost obsolete. Quasi-optical power combiners have been successful using other NDR devices such as Gunn diodes [22,23] and IMPATT diodes [24]. These devices, however, are primarily transit-time devices, where a lower bound for the oscillation frequency can be given by [25,26]:

$$f_{osc} \geq \frac{v_{sat}}{2W_{eff}}. \tag{2.1}$$

In this expression, v_{sat} is the saturation velocity of an electron in the semiconductor (around 6×10^6 cm/s in GaAs) and W_{eff} is the effective length of the drift region (typically on the order of a micron). Unlike these transit-time devices, tunnel diodes are extremely susceptible to low-frequency bias-line oscillations, and therefore share many of the difficulties associated with creating a monolithic RTD grid oscillator.

2.2. Modelling and Design

Fig. 2.2 shows the measured dc current-voltage relation for a germanium tunnel diode. The tunnel diodes used in this experiment were Germanium Power Devices TD272A diodes. A tunnel diode consists of a degenerately-doped p-n junction [25,26]. With small applied forward bias voltage, the current increases rapidly as electrons tunnel from the n-side to the p-side. As the voltage increases, the current increases to a maximum, and then begins to decrease due to fewer states available for the tunneling electrons on the p-side. In this part of the curve, the current decreases with increasing voltage, corresponding to a region of negative differential resistance. The device is unstable in the NDR region, and the parameter analyzer is unable to measure a meaningful trace. Finally,

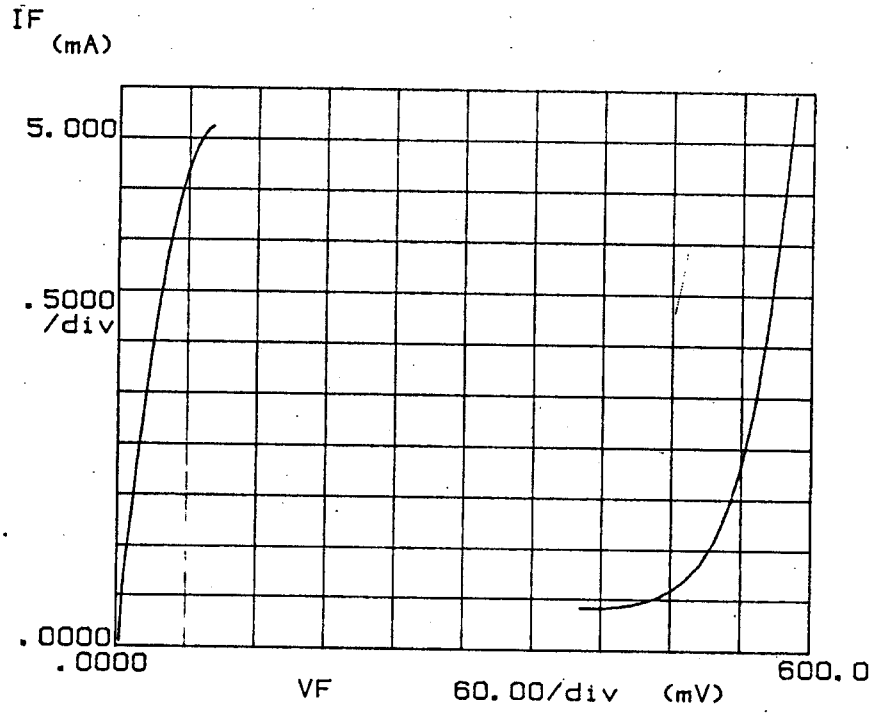

Fig. 2.2. Measured dc I-V curve for a Germanium Power Devices TD272A tunnel diode. The vertical scale is 0.5 mA/division and the horizontal scale is 60 mV/division.

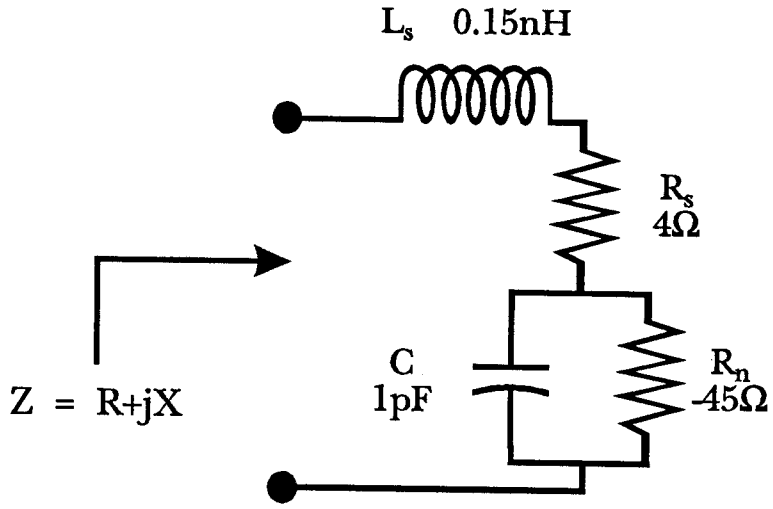

Fig. 2.3. Small-signal equivalent circuit for the GPD TD272A tunnel diode when biased in the NDR region. Component values obtained from the manufacturer's's data sheet [27].

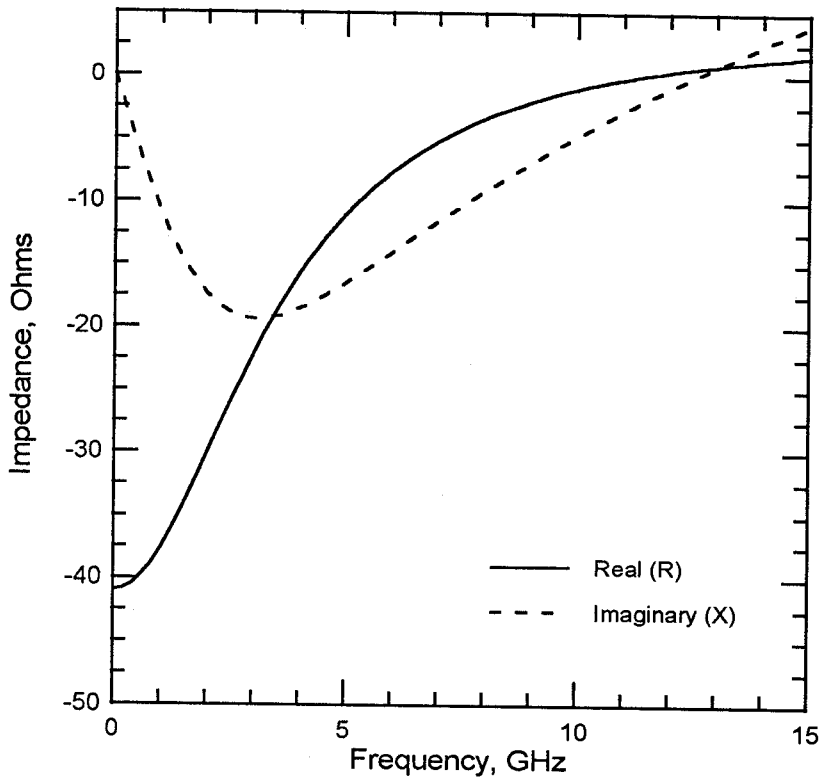

Fig. 2.4. Input impedance of the circuit in Fig. 2.3. The diode is potentially unstable from dc to 11.3 GHz.

as the bias voltage continues to increase, the current will eventually begin to exponentially grow, as in a familiar p-n junction.

Fig. 2.3 shows the small-signal equivalent circuit for the tunnel diode when biased in the NDR region. This circuit is very similar to the circuit for a normal diode, with parasitic series resistance R_s, series inductance L_s, and junction capacitance C. The unusual property of the tunnel diode is that the junction resistance, R_n, is negative. The diode will be potentially unstable when the real part of its input impedance is negative. Examination of the circuit in Fig. 2.3 gives an analytical expression for the maximum oscillation frequency f_{max}:

$$f_{max} = \frac{1}{2\pi |R_n| C} \sqrt{\frac{|R_n| - R_s}{R_s}}. \tag{2.2}$$

It has been assumed that $R_n < 0$ and $|R_n| \geq R_s$. For the component values given in Fig. 2.3, $f_{max} = 11.32\,\text{GHz}$. Fig. 2.4 shows the input impedance of this circuit as a function of frequency. As predicted by (2.2), the real part of the input impedance R is negative from dc up to 11.3 GHz. This implies that the device can oscillate anywhere from dc to f_{max}.

The grid oscillator is analyzed by considering an infinite periodic array of identical devices, all locked to the same frequency and phase. These assumptions allow one to exploit the symmetry of the structure, and simplify the analysis by examining a single device in an equivalent waveguide unit cell [28]. The unit cell, shown in Fig. 2.5, consists of electric walls on the top and bottom, and magnetic walls on the sides. The size of the unit cell is chosen so that the TEM mode of the equivalent waveguide is the only propagating mode.

Next, the driving-point impedance seen from the device terminals is calculated. First, the surface current density on the vertical strip is determined using the method of moments. Once an estimate for the surface current has been obtained, the impedance can be computed using the induced emf technique. This

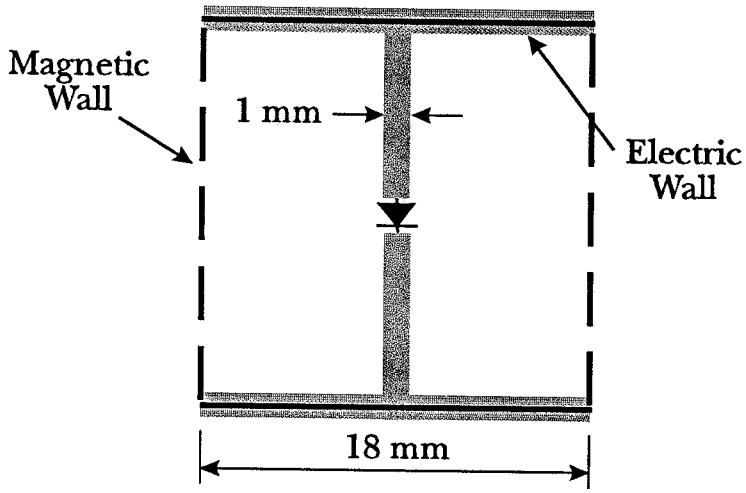

Fig. 2.5. The equivalent waveguide unit cell. The dimension of the cell is the same as the spacing between devices.

approach is a refinement of the elegant method developed by R.M. Weikle at Caltech [29]. Further details can be found in Appendix A.

Finally, we can construct a rather intuitive transmission-line equivalent circuit for the tunnel diode oscillator grid. The oscillator's physical configuration is shown in Fig. 2.6(a). The grid is constructed on a Duroid substrate with a relative dielectric constant of 10.8. The equivalent circuit is shown in Fig. 2.6(b). Free space is represented by the 377-Ω resistor, and the mirror behind the grid is represented by the short-circuited transmission line. The Duroid substrate also appears as a transmission line of appropriate electrical length and characteristic impedance. The inductance of the vertical strip represents coupling to the evanescent TE modes of the equivalent waveguide.

There are several ways to analyze the circuit of Fig. 2.6(b). We have found the approach suggested by Martinez and Compton [30] to be useful. A circulator is inserted at a node, as shown in Fig. 2.7. The reflection coefficient from the circulator is defined as the circular function, C. The circular function can be

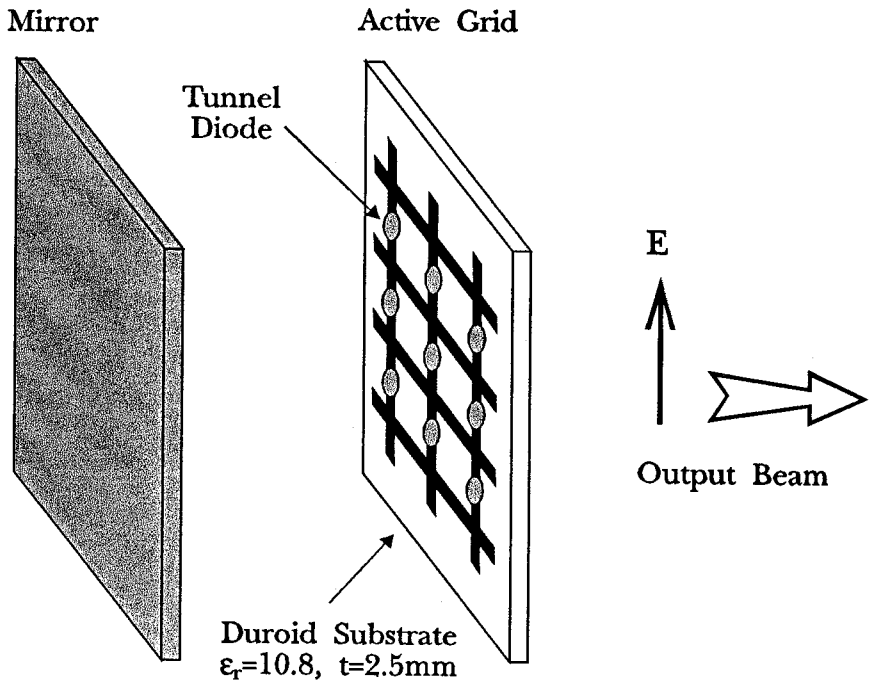

(a)

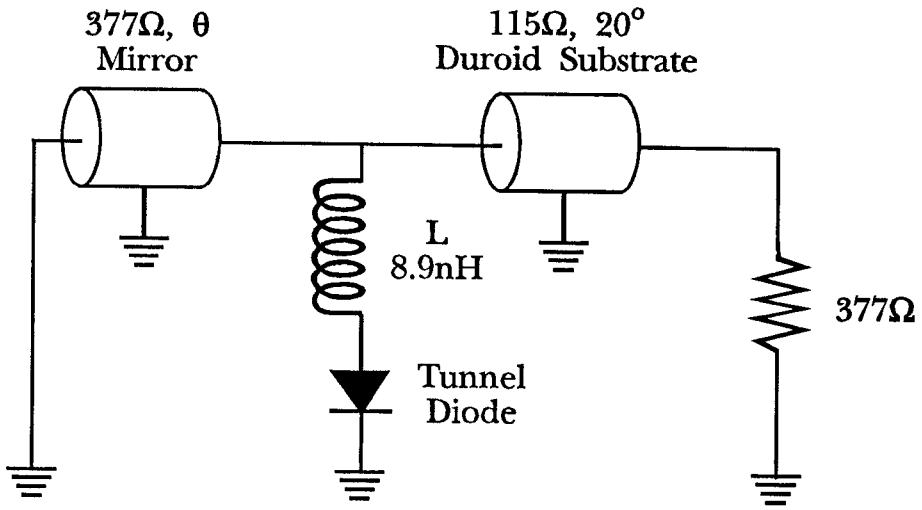

(b)

Fig. 2.6. Physical configuration (a) and transmission-line equivalent circuit (b) of the grid oscillator at 2 GHz.

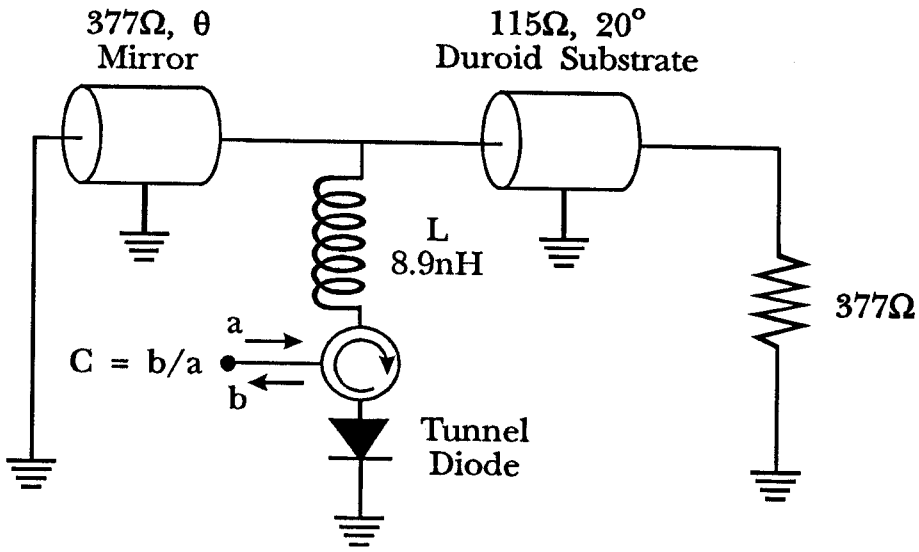

Fig. 2.7. Insertion of the circulator to measure the circular function.

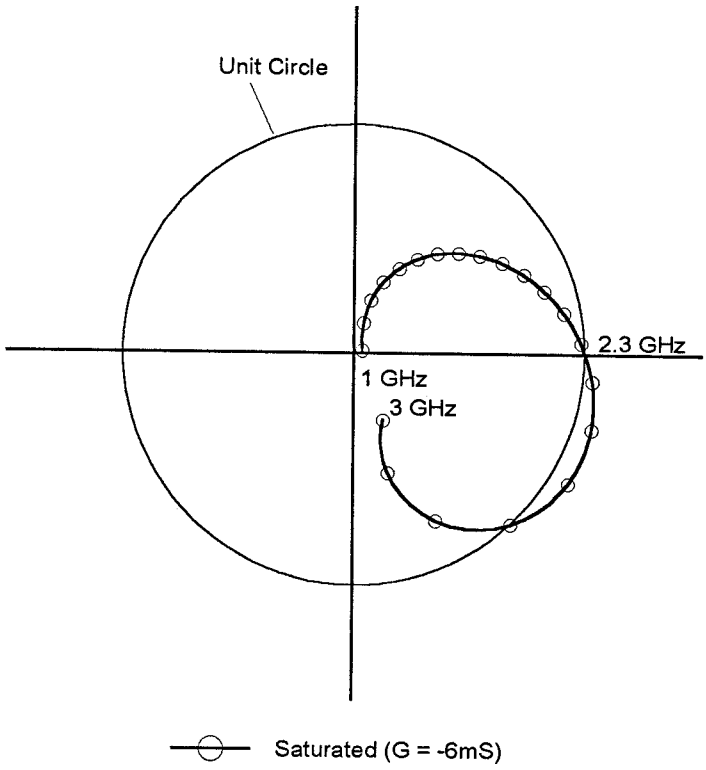

Fig. 2.8. Saturated circular function. The circuit should oscillate at 2.3 GHz.

thought of as a measure of the open loop gain of the circuit. Stability theory indicates that the circuit will be unstable when the loop gain equals unity. Fig. 2.8 shows the saturated circular function of the grid. Saturation in the diode was modelled by reducing the magnitude of the negative conductance ($G_n = 1/R_n$) from −22 mS to −6 mS. At this point, C is unity at 2.3 GHz, implying that the grid should oscillate at this frequency.

To validate this design procedure, a microstrip oscillator was built using a single GPD TD272A tunnel diode. The oscillator was designed to operate at 2.3 GHz using the above technique. A spectrum analyzer plot of the output spectrum is shown in Fig. 2.9. The circuit oscillates at 2.29 GHz, in excellent agreement with the model. The oscillator power was 180 μW with an overall dc-to-rf conversion efficiency of 40%.

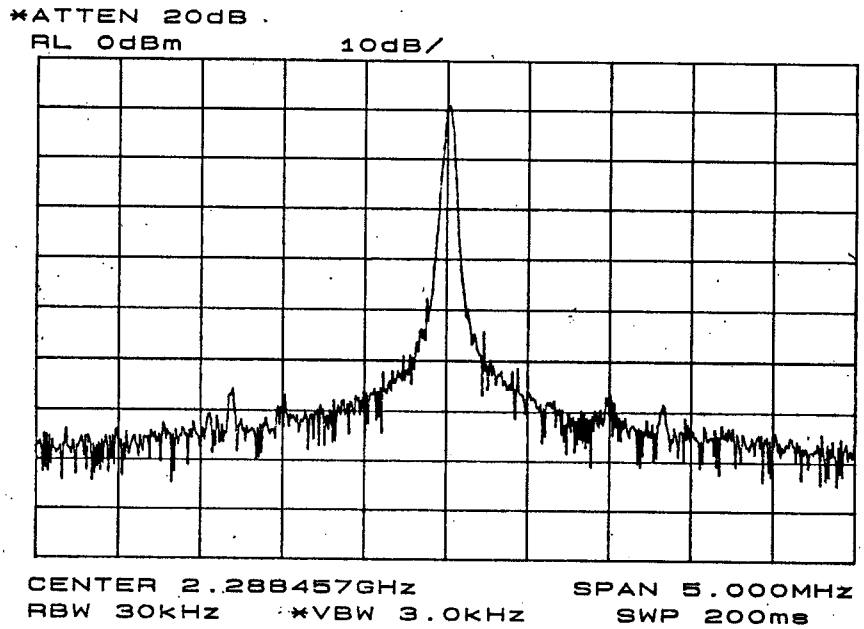

Fig. 2.9. Measured output spectrum of a microstrip tunnel diode oscillator. The center frequency is 2.29 GHz. The vertical scale is 10 dB/division and the horizontal scale is 500 kHz/division.

2.3. Grid Construction

The completed grid is shown in Fig. 2.10. The grid is a 4×4 array of GPD TD272A tunnel diodes, spaced 18 mm apart. A monolithic RTD grid would be fabricated on a GaAs wafer, which has a relative dielectric constant of 13. In an attempt to better simulate this situation with the tunnel diode grid, the devices were soldered onto an etched 2.5-mm thick Duroid substrate with $\varepsilon_r = 10.8$. The diodes are arranged such that adjacent rows share bias lines. In order to preserve the symmetry of the grid, we would like to present a low rf impedance to the topmost and bottommost rows, as dictated by the electric wall boundary condition. To help achieve this, the stubs along the upper and lower rows are

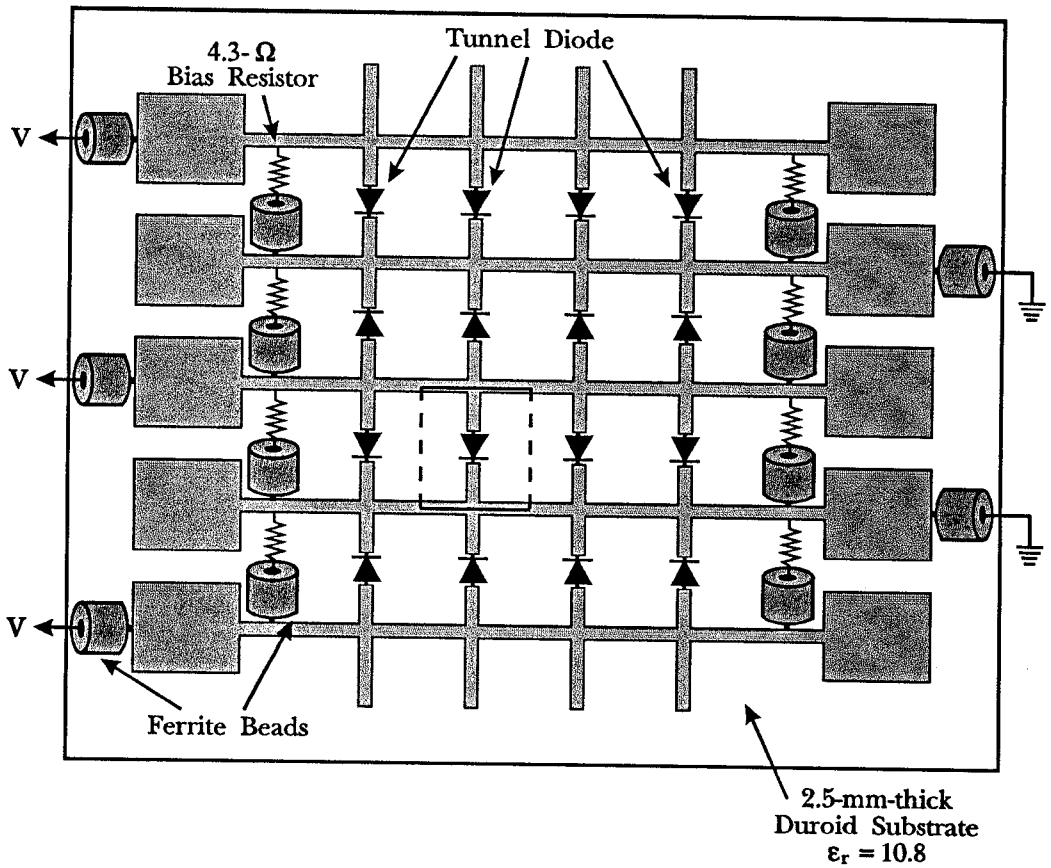

Fig. 2.10. The assembled oscillator grid. The devices are spaced 18 mm apart.

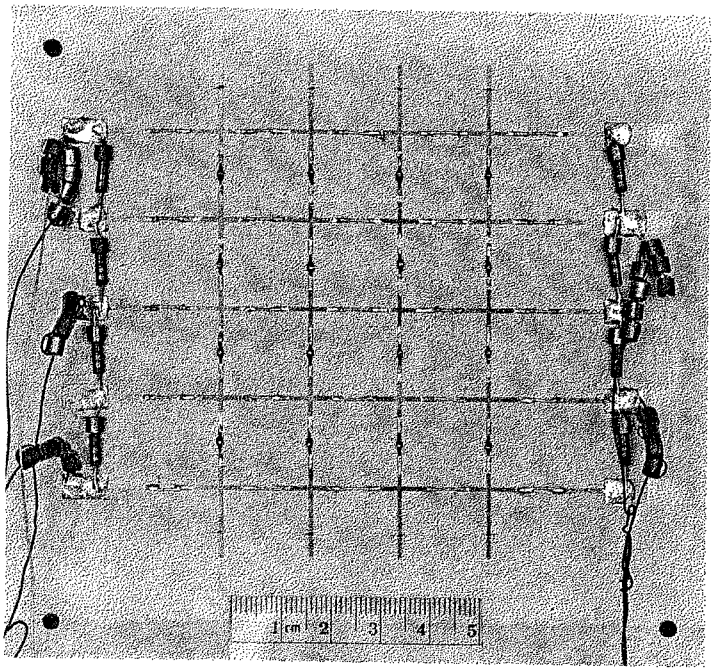

Fig. 2.11. Photograph of the 16-element tunnel diode grid oscillator. The entire array is 7.2 cm on a side.

an effective quarter-wavelength. Ferrite beads were used extensively to suppress bias-line oscillations. A photograph of the oscillator is shown in Fig. 2.11.

The entire grid can be biased with a single dc supply. This dc supply must have a low source resistance in order to bias the devices into the NDR region. When biasing a single device, the source resistance must be lower than the magnitude of the diode's negative junction resistance. Biasing an entire row in parallel compounds this requirement. If a single supply is used to bias the whole grid, this requirement is even more stringent—the entire array is essentially in parallel. The dc source's resistance must be less than one-sixteenth of a tunnel diode's negative resistance, which corresponds to less than $3\,\Omega$. To insure that we do present a low source resistance, 4.3-Ω carbon resistors were placed at the ends of each row. These resistors will severely reduce the overall dc-to-rf efficiency of the grid, but were found to be necessary.

2.4. MEASUREMENTS

A necessary component for measuring the oscillator grid is a well-characterized antenna near 2 GHz. A number of simple coaxial probe antennas were built and tested, none of which gave satisfactory results over a sufficient bandwidth. The discone antenna is noted for its wide bandwidth [31]. Two identical discones were designed and built by John Davis at Caltech. Fig. 2.12 shows the antenna characterization setup. The two antennas are separated by a distance R. Because this is a far-field measurement, R must satisfy [32]:

$$R > \frac{2D^2}{\lambda}, \tag{2.3}$$

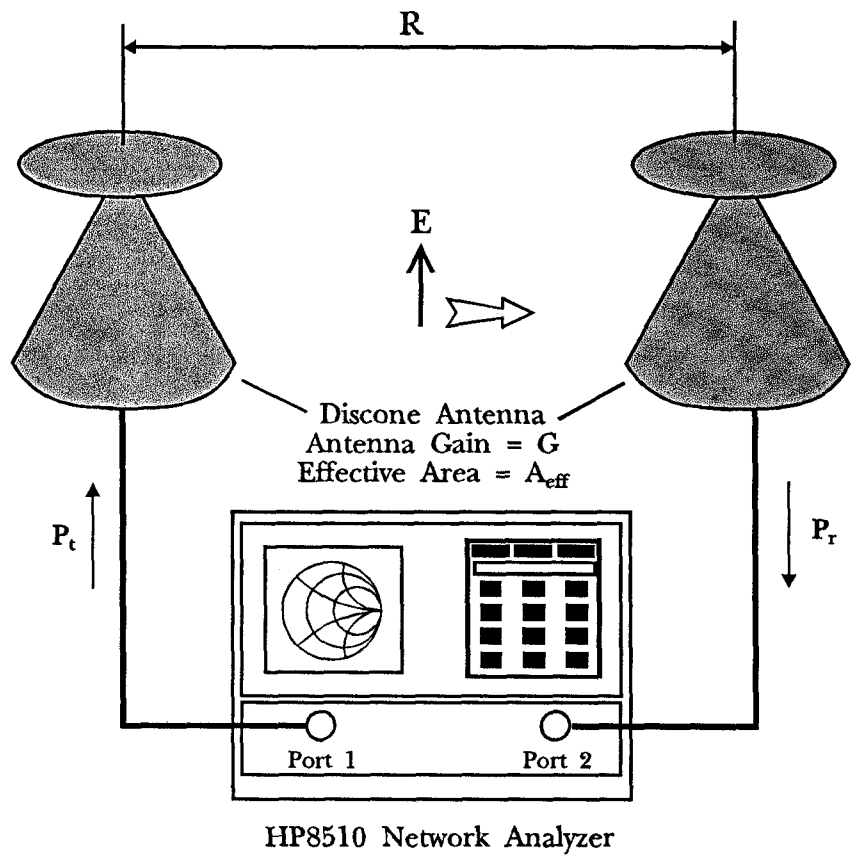

Fig. 2.12. The discone antenna far-field measurement setup.

where λ is the shortest free-space wavelength and D is the longest antenna dimension. Assuming each discone has an effective area A_{eff}, the ratio of received power to transmitted power is given by Friis transmission formula [32]:

$$\frac{P_r}{P_t} = |S_{21}|^2 = \frac{A_{eff}^2}{(\lambda R)^2}. \tag{2.4}$$

The network analyzer directly measures $|S_{21}|$, and we compute the effective area:

$$A_{eff} = |S_{21}|\lambda R. \tag{2.5}$$

Fig. 2.13 shows the effective area of the antenna as a function of frequency. The discone is reasonably well behaved from 500 MHz to 3.8 GHz. There seems to be a resonance near 2.2 GHz; oscillator measurements taken near this frequency may be suspect.

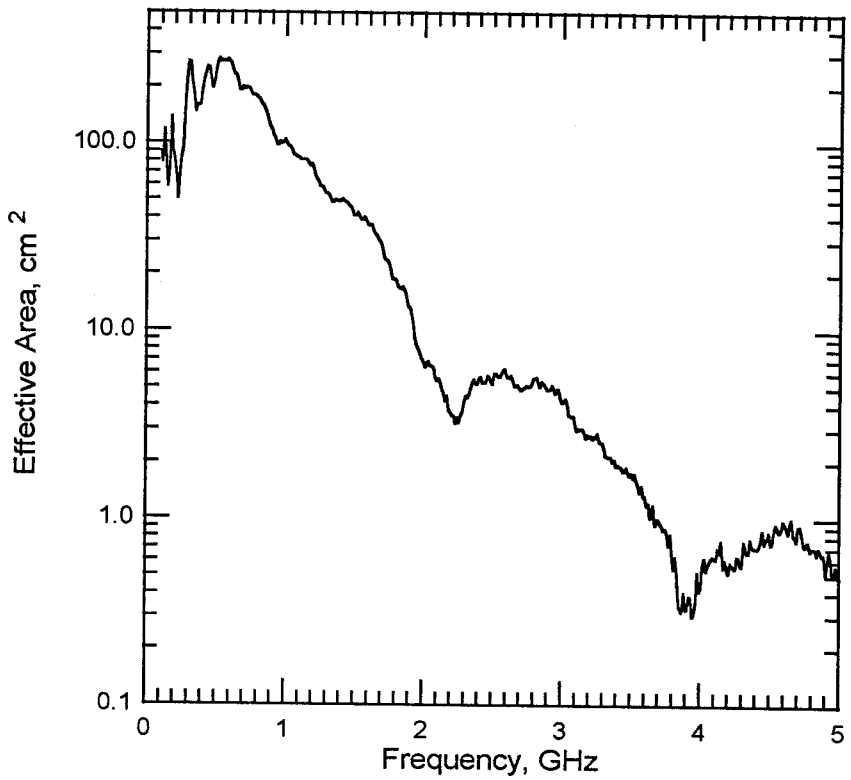

Fig. 2.13. The effective area of the discone as a function of frequency. The discone is well-behaved from 500 MHz to 3.8 GHz.

The setup used to measure the oscillator grid is illustrated in Fig. 2.14. The entire array was biased with a single dc supply. A discone antenna and spectrum analyzer were used to receive the power radiated from the grid. The grid was placed in the far-field of the receiving antenna. A double-slab tuner was used to maximize the grid's output power. This tuner consists of two 6.4-mm-thick Stycast slabs with $\varepsilon_r = 12$ placed in front of the grid. This is the quasi-optical analog of the double-slug tuner used in coaxial systems. By varying the spacing between slabs and the distance between the grid and tuner, the impedance seen at the output surface of the oscillator grid can be changed dramatically.

Initially, the grid suffered from low-frequency bias-line oscillations. These oscillations were suppressed by placing ferrite beads on the bias wires and on the

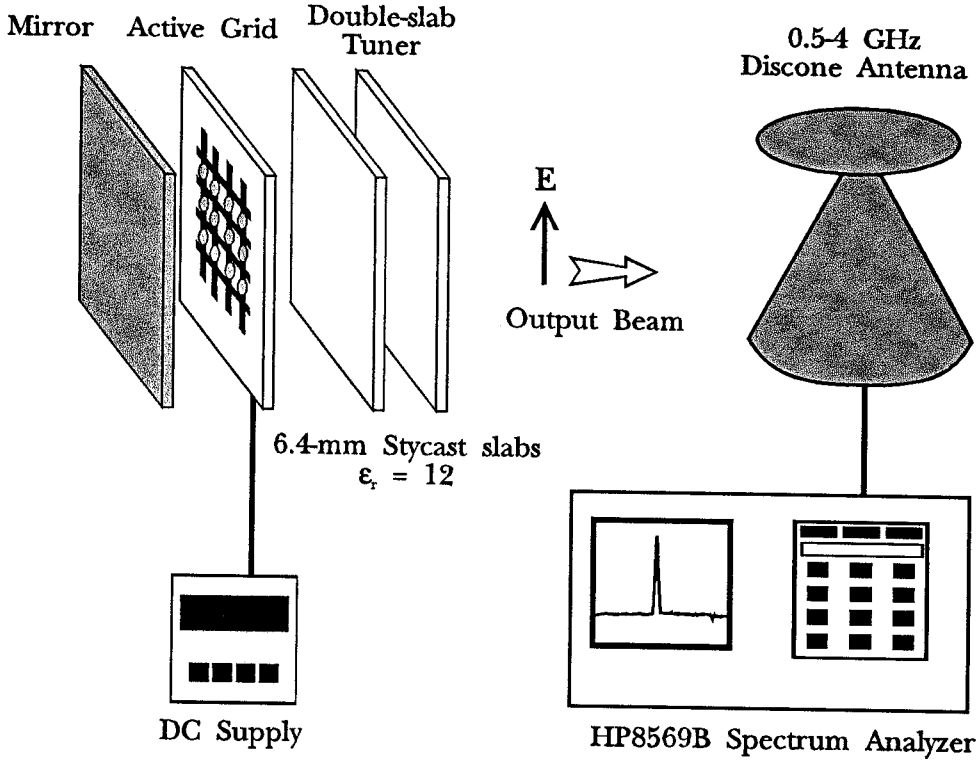

Fig. 2.14. The grid oscillator measurement setup.

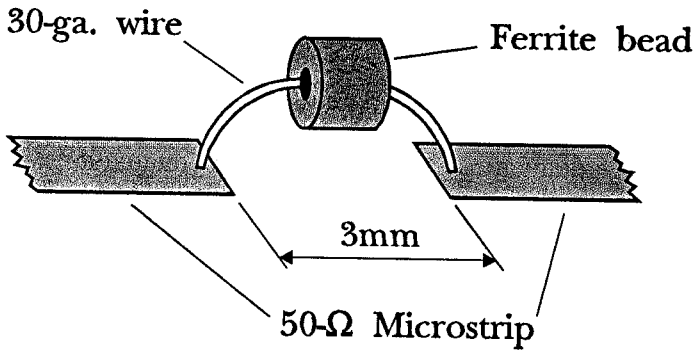

(a)

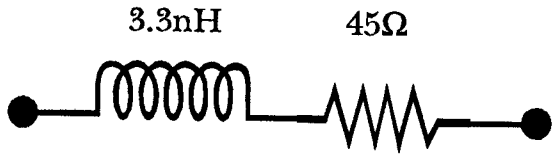

(b)

Fig. 2.15. Microwave measurement of a ferrite bead (a) and equivalent circuit model (b) valid between 200 MHz and 10 GHz.

leads of the 4.3-Ω bias resistors. In previous oscillator grids, ferrite beads have been used to eliminate spurious bias-line oscillations. Although it is not well understood why ferrites are so successful in killing these oscillations, measurements indicate that the ferrite material is quite lossy. A microstrip measurement of a piece of 30-gauge wire-wrap wire through a Lodestone Pacific #2643000101 ferrite bead is illustrated in Fig. 2.15(a). This measurement reveals the equivalent circuit model for the ferrite shown in Fig. 2.15(b). This simple circuit models the behavior of the ferrite reasonably well between 200 MHz and 10 GHz. The considerable series resistance may account for the suppression of spurious bias-line oscillations.

Fig. 2.16 shows the output frequency spectrum of the tunnel diode grid oscillator. Peak power was measured at 1.86 GHz. The relatively clean, narrowband peak in the spectrum indicates that the devices are properly locked. The measured frequency is about 20% lower than the design frequency, 2.3 GHz. This may be attributed to the fact that the grid is so small. The unit cell approach used in the design assumes an infinite, unterminated array. Elements on the periphery of the grid clearly violate this assumption. In a 4×4 array, 75% of the elements are on an edge. In this light, the frequency shift is not surprising.

An often-quoted and conveniently-measured figure of merit for quasi-optical sources is the Effective Radiated Power (ERP) [28]. The ERP is the power an isotropic source would have to radiate to give the same power density. This figure is related to the power measured in a quasi-optical test system, P_{meas}, by:

$$\mathrm{ERP} = P_{meas}\frac{4\pi R^2}{A_{ant}}, \tag{2.6}$$

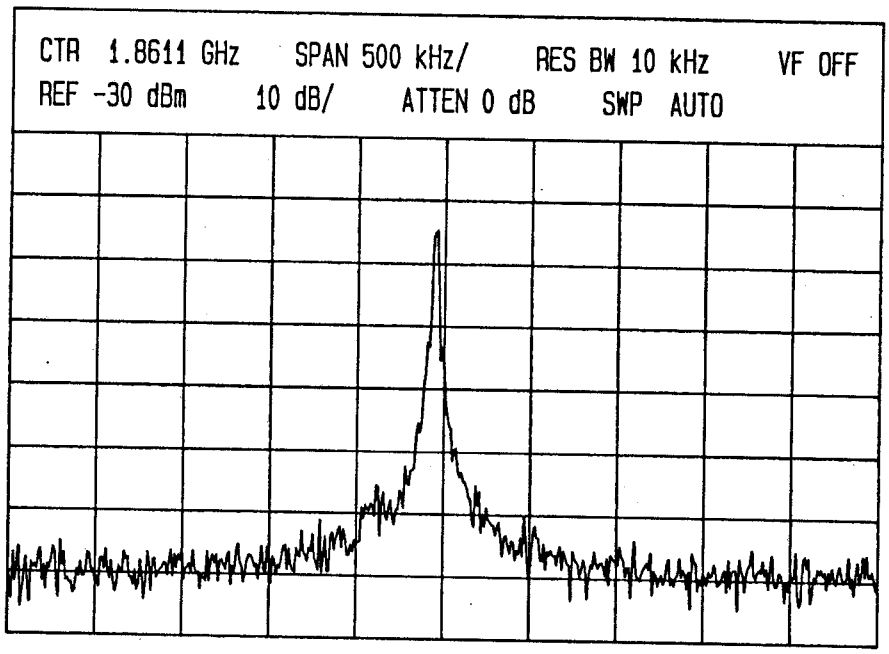

Fig. 2.16. Measured output spectrum the tunnel diode grid oscillator. The center frequency is 1.86 GHz. The vertical scale is 10 dB/division and the horizontal scale is 500 kHz/division.

where A_{ant} is the effective area of the receiving antenna and R is the distance separating the antenna and the grid. The tunnel diode grid had a peak ERP of 1.3 mW at 1.86 GHz using the double-slab tuner. Without the tuner, the peak ERP was 5 dB lower. The total dc bias was 480 mA at 280 mV. It is estimated that only about 50 mA of the bias current flows through the diodes, while the remainder is lost in the bias resistors.

Unless a full two-dimensional radiation pattern is measured, determining the total power radiated by the grid is difficult. M. Gouker has suggested the Effective Transmitter Power (ETP) to estimate this quantity [33]. The ETP assumes the array acts like a uniformly-illuminated aperture, and is related to ERP by:

$$\mathrm{ETP} = \frac{\mathrm{ERP}\lambda^2}{4\pi A_{array}}, \tag{2.7}$$

where A_{array} is the physical area of the grid and λ is the free-space wavelength. For our case, $A_{array} = 16A_{cell} = 51.8\,\mathrm{cm}^2$. This grid has an ETP of 500 μW, or 31 μW per device. Compared to the results from the single-diode microstrip oscillator, this power seems rather low, suggesting a poor power-combining efficiency. Furthermore, radiation pattern measurements indicate that the ETP may actually overestimate the total radiated power.

The Single-Sideband (SSB) noise performance was measured using a computer-controlled technique developed by Shi-Jie Li at Caltech. With the output tuner, the average SSB noise level was –76dBc/Hz at a 100 kHz offset from the carrier. The double-slab tuner increases the quality factor, or Q, of the oscillator circuit. As a result, the noise level is 3 dB worse with the tuner removed. An advantage of quasi-optical oscillators is that the noise performance improves as the array size increases because the noise from each individual element adds incoherently. This has been experimentally demonstrated in a MESFET grid oscillator built by Jon Hacker [34]. It is also possible to improve the noise performance of grid oscillators via injection locking [28].

Fig. 2.17 shows the grid's measured far-field H-plane radiation pattern without the double-slab output tuner. Also plotted is a theoretical pattern, generated assuming a uniform array of 16 elementary dipoles in front of a mirror. For simplicity, the Duroid substrate is neglected. This provides a theoretical pattern given by:

$$P(\theta) \propto \frac{\sin^2\left(\frac{4\pi a}{\lambda}\sin\theta\right)}{\sin^2\left(\frac{\pi a}{\lambda}\sin\theta\right)} \sin^2\left(\frac{2\pi m}{\lambda}\cos\theta\right). \tag{2.8}$$

The first term represents the H-plane array factor, where a is the element spacing. The second term accounts for the mirror, with m being the distance from the grid to the mirror. In this case, $a = 18\,\text{mm}$ and $m = 33\,\text{mm}$. Aside from a slight offset, the measured pattern agrees well with the theoretical one. The on-axis cross-polarization ratio was –23 dB.

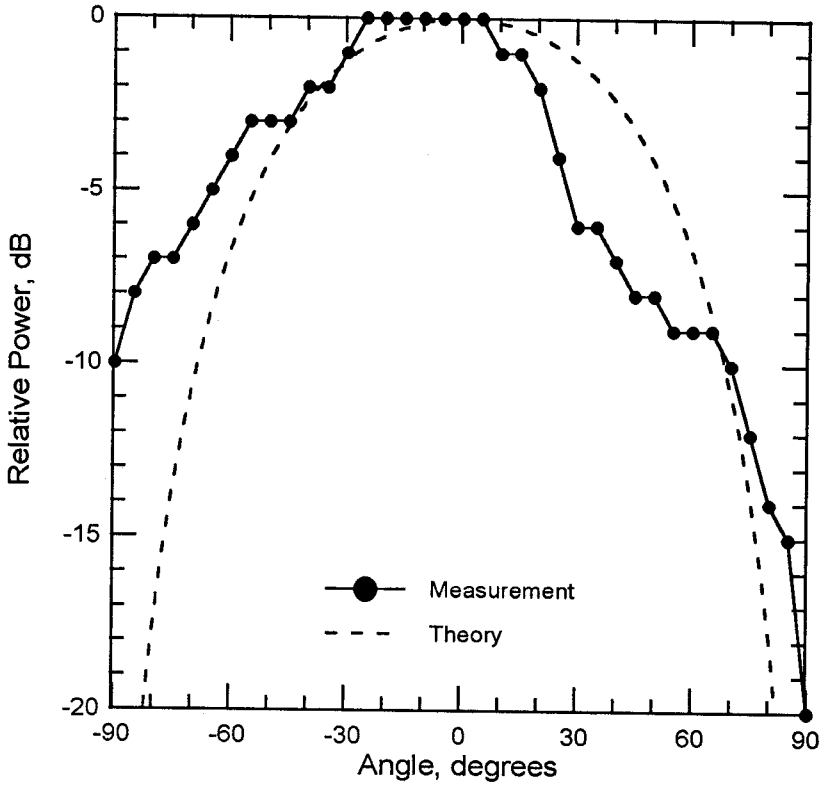

Fig. 2.17. Measured and theoretical H-plane radiation pattern at 1.86 GHz with the tuner removed.

Fig. 2.18 shows the measured far-field E-plane radiation pattern without the output tuner. The theoretical pattern was generated using (2.8), multiplied by an additional $\cos^2\theta$ term to account for the element pattern of the dipole. This results in a slightly narrower E-plane pattern. Again, the theory and measurement agree well.

Fig. 2.19 shows the E- and H-plane radiation patterns with the double-slab output tuner in place. The patterns of the tuned grid are considerably narrower than those of the untuned grid. This may be due to the impedance of the tuner varying rapidly with angle. The sharper radiation patterns give us cause to believe that the ETP, quoted above, may overpredict the total radiated power.

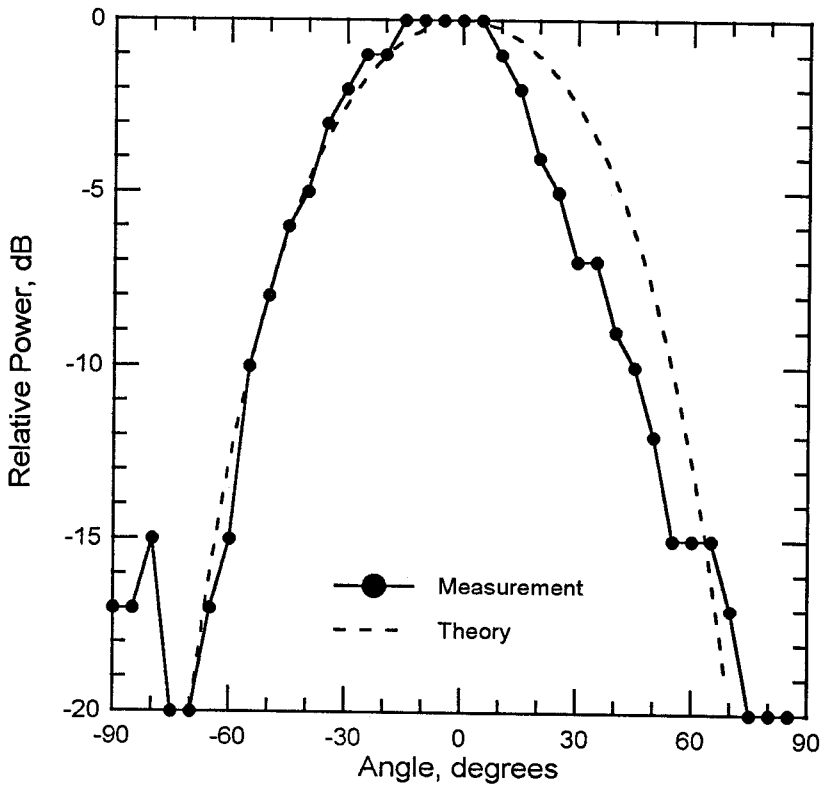

Fig. 2.18. Measured and theoretical E-plane radiation pattern at 1.86 GHz with the tuner removed.

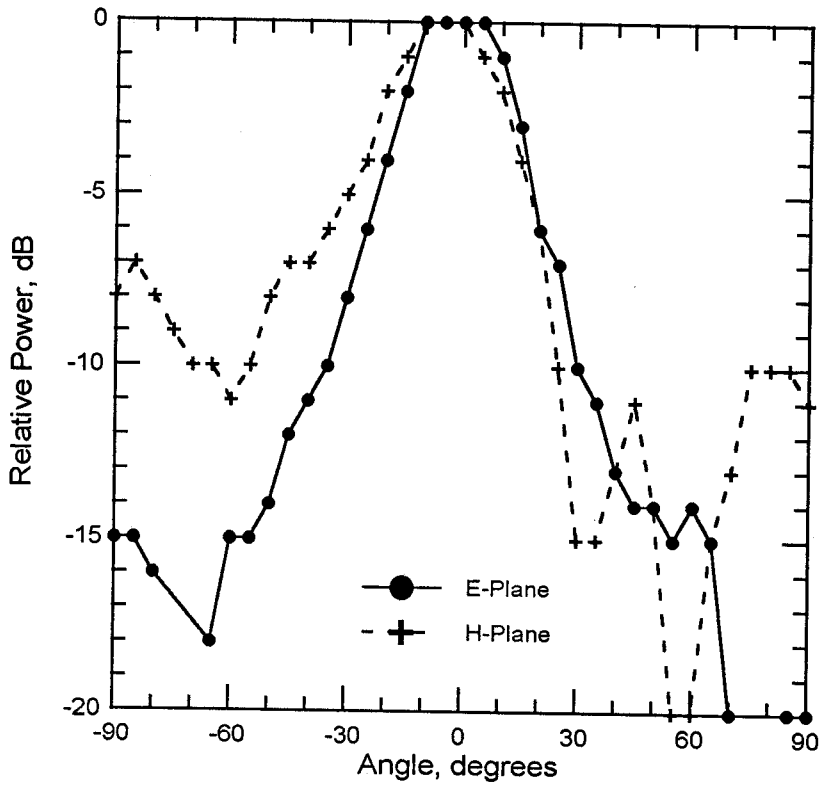

Fig. 2.19. Measured E and H-plane radiation patterns at 1.86 GHz with the double-slab tuner in place and adjusted for maximum ERP. The on-axis cross polarization ratio was –20 dB.

Subharmonic oscillations were observed in the frequency spectrum at multiples of one-third of the main frequency. The measured power in these components, however, was very small when compared to the main component at 1.86 GHz, as shown in Fig. 2.20. The highest level was 16 dB below the main component. The power level at 620 MHz, one-third of the main frequency, was 46 dB below the main signal.

When these subharmonics were first observed, it was suspected that the grid may be operating in the wrong mode. Many attempts were made at suppressing the subharmonic components, including the addition of various lumped elements into the grid oscillator structure, none of which were successful. The low power

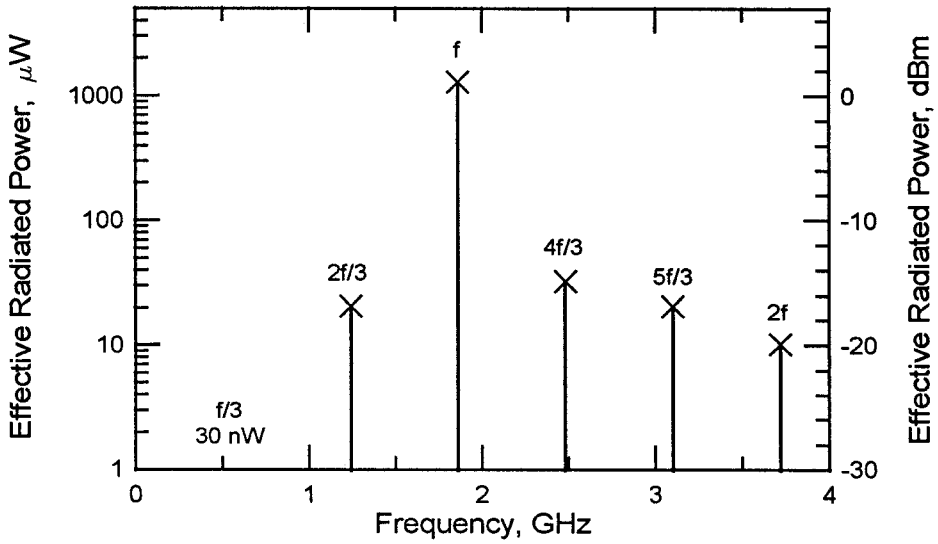

Fig. 2.20. The subharmonic components of the oscillator spectrum. The highest component is 16 dB below the main signal at 1.86 GHz.

associated with the subharmonics, the reasonable radiation patterns, and the low cross-polarization levels led to the conclusion that the grid was, in fact, operating in the correct mode. In addition, the bias lines were directly probed, and the measured power on the lines was less than –50 dBm, which further supports this conclusion.

We may be seeing evidence of period tripling, a type of bifurcation that can arise in nonlinear oscillators [35]. This behavior is not uncommon in NDR oscillator circuits—similar results have been observed in single-element oscillators using RTD's [36], as well as IMPATT and Gunn diode oscillators [37]. A system of two coupled tunnel diode oscillators has produced subharmonic components at multiples of one-eleventh of the main frequency [38]. In this grid, more bifurcations could be observed, depending on the mirror position and bias level, as well as the broadly-distributed spectra indicative of chaotic behavior. Fig. 2.21 shows an example of a chaotic spectrum.

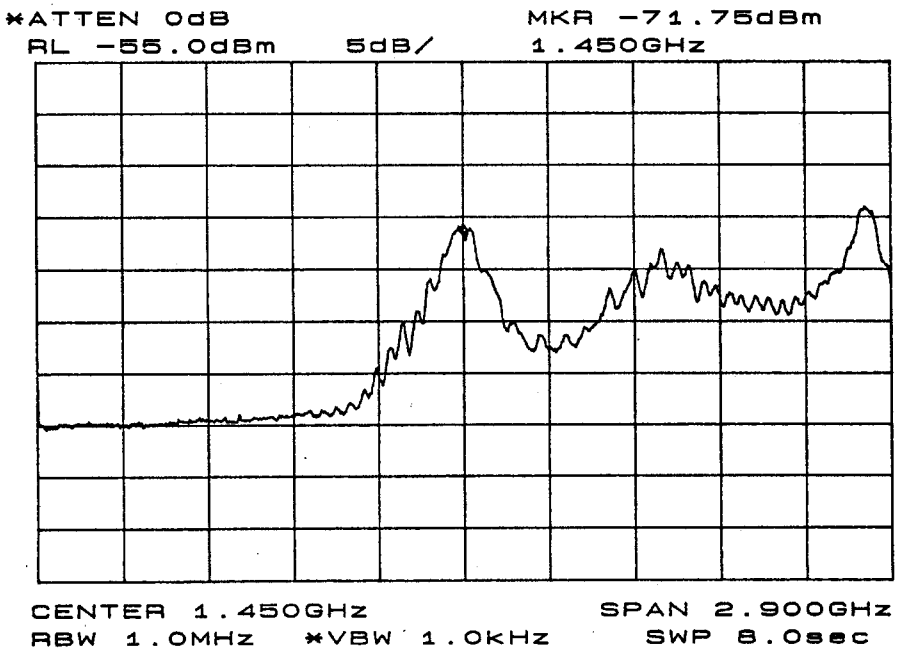

Fig. 2.21. Broadly-distributed output spectrum indicative of chaotic behavior in the grid oscillator. The vertical scale is 5 dB/division. The horizontal scale runs from 0 to 2.9 GHz, with 290 MHz/division.

Another possibility is that the some part of the grid structure is resonant at the one-third frequency, 620 MHz. It has been pointed out that grid oscillators may be particularly susceptible to substrate-mode oscillations [39]. One-half of an effective wavelength at 620 MHz is about 10 cm, where the effective dielectric constant was chosen to be 5.9, the mean between the substrate and air. This distance roughly corresponds to the spacing of the columns of bias resistors or the distance between the ends of the vertical stubs on the top and bottom rows of the grid. It is unlikely that this theory explains the subharmonic oscillations, however, because changing the position of the bias resistors or cutting gaps in the vertical stubs did not significantly change the oscillation frequency.

This oscillator is the first quasi-optical grid using broadband NDR devices. A locked output spectrum was achieved, with a peak ERP near the design frequency. The results were not as successful as hoped, namely the rather poor apparent combining efficiency and the subharmonic components in the spectrum. Nevertheless, the results were encouraging enough to warrant an attempt at a monolithic RTD oscillator grid.

2.5. RTD Grid Design

Based on the success of the hybrid tunnel diode oscillator grid, several designs for monolithic RTD grid oscillators have been completed. This is a collaborative project between Caltech, Dr. R.P. Smith's group at JPL, and Prof. M.J.W. Rodwell's group at the University of California at Santa Barbara. The active devices are Schottky-Collector Resonant Tunneling Diodes (SCRTD's), developed at UCSB and JPL [12–14]. Traditional high frequency diodes are rather large-area dots that are then contacted with whiskers [7,10,11].

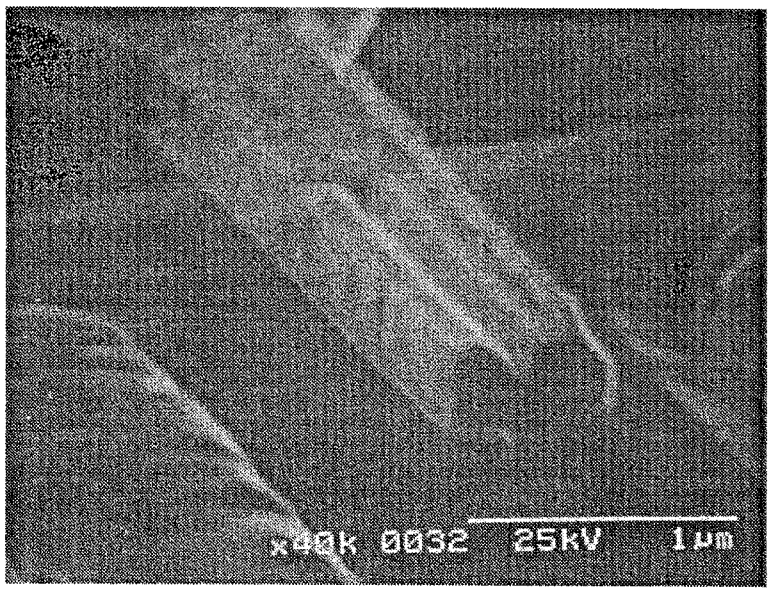

Fig. 2.22. SEM micrograph of a completed $0.1\times2\,\mu$m SCRTD. Figure courtesy of R.P. Smith at JPL.

These SCRTD's, however, are planar and therefore better suited to monolithic fabrication. They include a low-parasitic air-bridged connection to the collector. Fig. 2.22 shows a completed SCRTD.

Like tunnel diodes, SCRTD's have a negative-sloping section in their dc current-voltage curve where they are potentially unstable. Fig. 2.23 shows the small-signal equivalent circuit for the SCRTD when biased in the NDR region. As was the case for the tunnel diode, the circuit includes a parasitic series resistance R_s, a junction capacitance C, and a negative resistance R_n. Also included is a negative inductor L_{qw}, which represents the transit time through the quantum well. Fig. 2.24 shows the input impedance of this device as a function of frequency. The resistive part of this impedance is negative from dc up to 920 GHz. This implies that the device is capable of oscillating up to 920 GHz, the f_{max} of the diode.

The oscillators were designed using the same procedure used for the tunnel diode grid. The physical configuration of the grid is shown in Fig. 2.25(a). The grid is monolithically fabricated on a GaAs substrate. The oscillator chip is mounted onto a hyper-hemispherical antireflection-coated silicon lens. This lens will collimate the radiated beam as well as help prevent the excitation of substrate modes. The transmission-line equivalent circuit is shown in Fig. 2.25(b). Free space is represented by the 377-Ω resistor, and the mirror behind the grid is represented by the short-circuited transmission line. The dielectric lens is modelled by the transformer, and the inductor represents the coupling to the device via the short vertical lead. The $\times$ marks the node where the circulator is inserted to determine the oscillation frequency of the circuit. Fig. 2.26 is a plot of the saturated circular function, C. As before, saturation in the device is modelled by reducing the magnitude of the diode's negative conductance. This particular circuit should oscillate at 500 GHz.

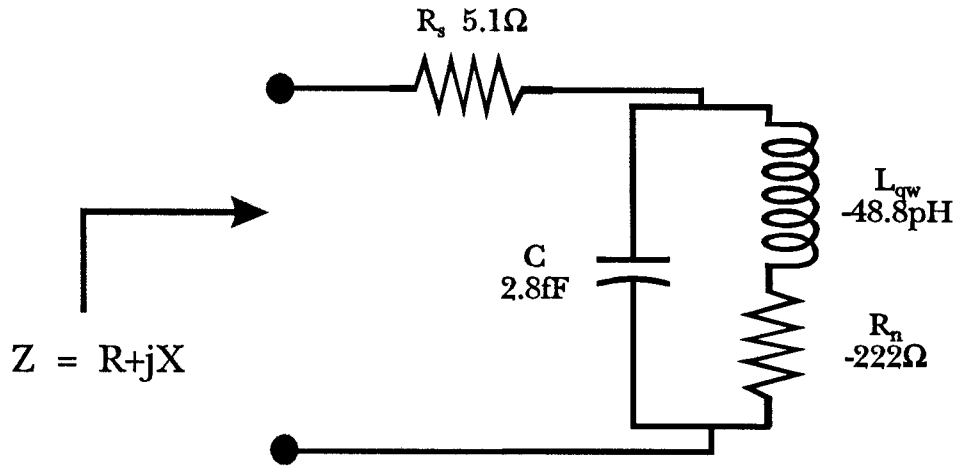

Fig. 2.23. Small-signal equivalent circuit for a 1-μm^2 SCRTD when biased in the NDR region.

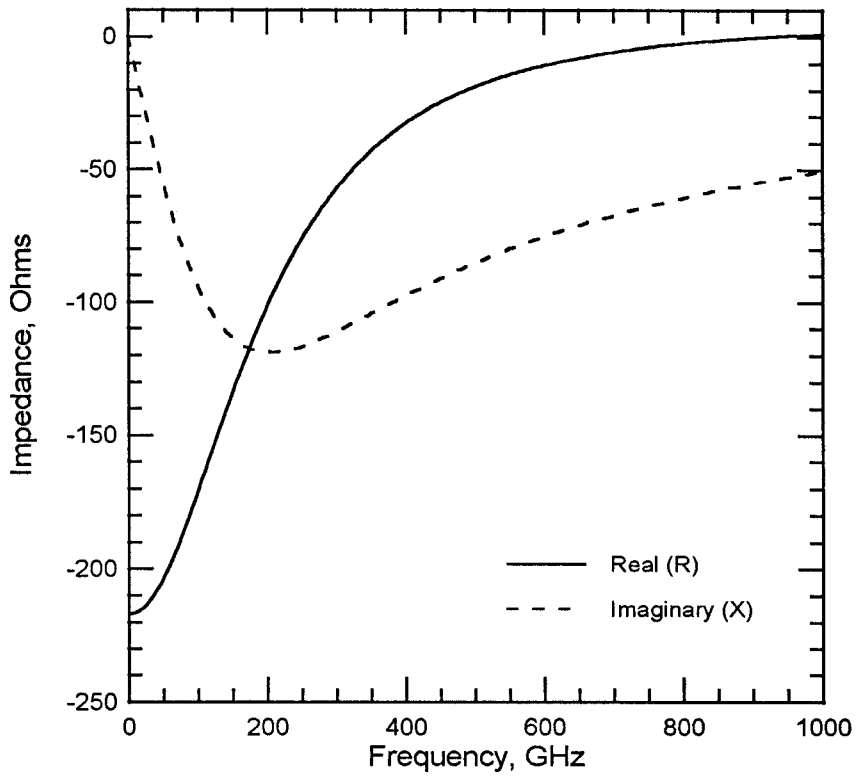

Fig. 2.24. Input impedance of the circuit in Fig. 2.23. The diode is potentially unstable from dc to 920 GHz.

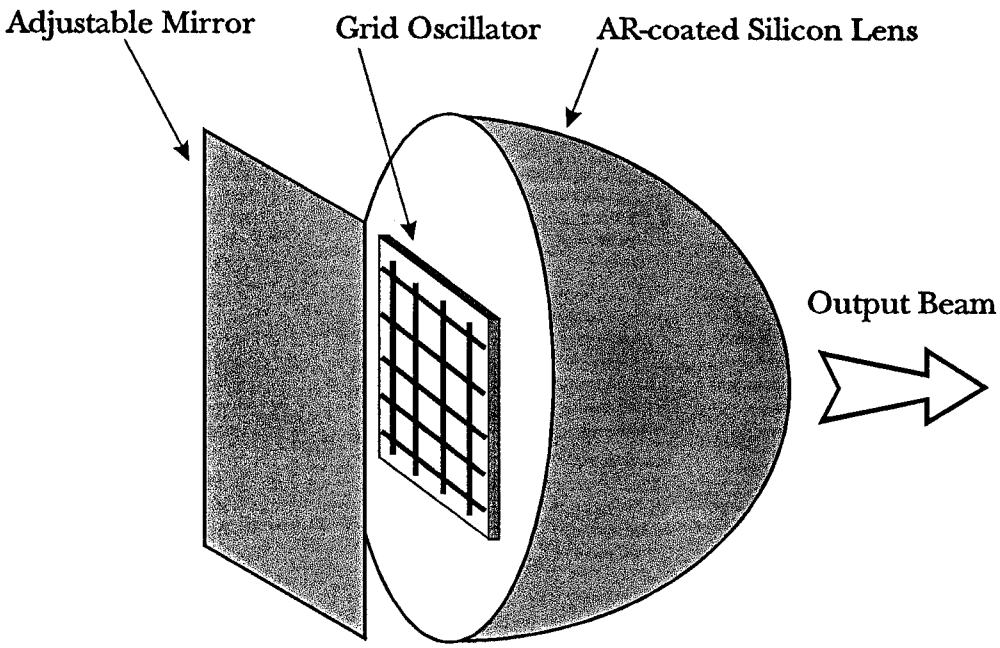

(a)

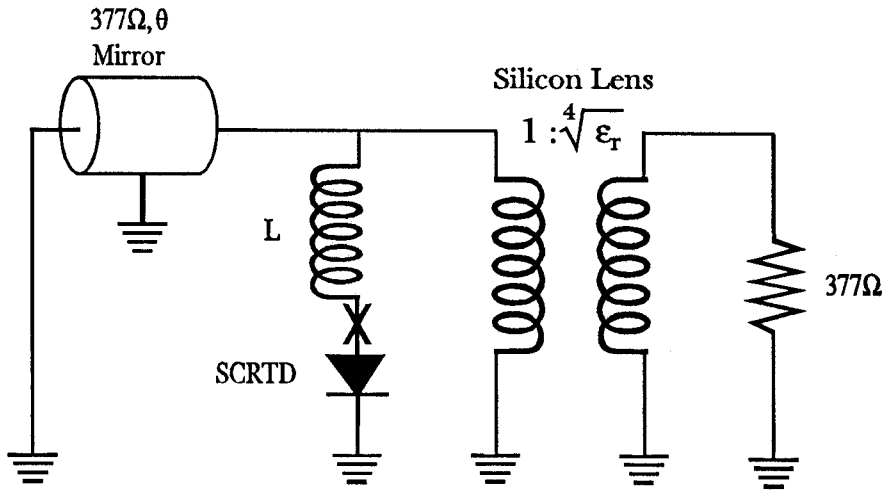

(b)

Fig. 2.25. Physical configuration (a) and transmission-line equivalent circuit (b) of the monolithic SCRTD grid oscillator. The × marks the spot where the circulator is inserted to measure the circular function.

A variety of designs from 200 GHz to 500 GHz have been completed and are summarized in Table 2.1. Arrays of two sizes are to be fabricated: 6×6 and 10×10. Fig. 2.27 shows a 100-element oscillator designed for 300 GHz. The unit cell size is 107 μm. Included at both ends of each row are monolithically integrated Schottky diodes to be used in the bias circuitry. These diodes perform a similar function as the bias resistors did in the tunnel diode grid. In addition, they have been found to be helpful in preventing low-frequency bias-line oscillations [40]. Fig. 2.28 shows a 36-element grid designed to oscillate at 500 GHz, with a 47 μm unit cell. The mask set for these grids has been completed, and the arrays are awaiting fabrication.

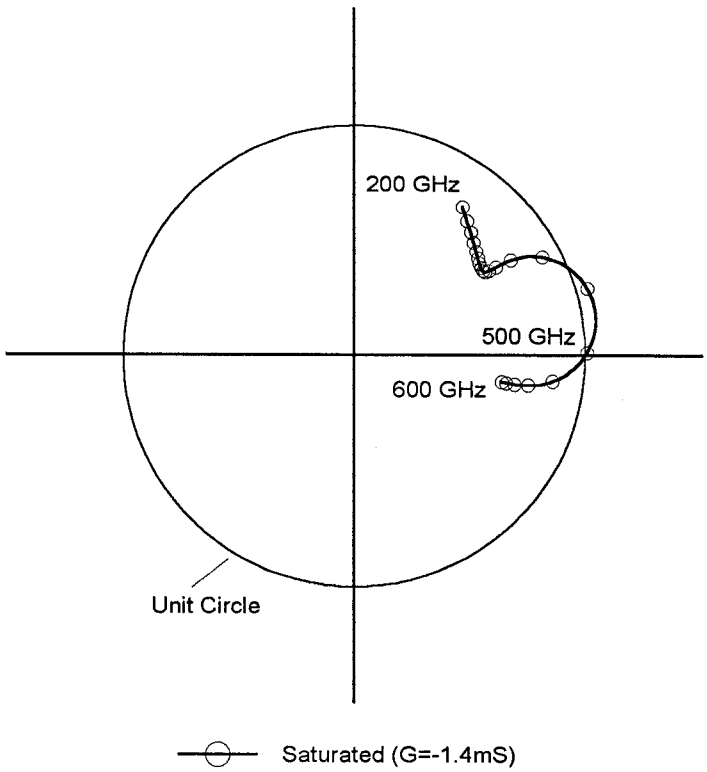

Fig. 2.26. Saturated circular function. The circuit should oscillate at 500 GHz

Design Frequency	Unit Cell Size
200 GHz	185 μm
300 GHz	130 μm
300 GHz	107 μm
400 GHz	85 μm
400/500 GHz	65 μm
500 GHz	47 μm

Table 2.1. Summary of monolithic SCRTD grid oscillator designs.

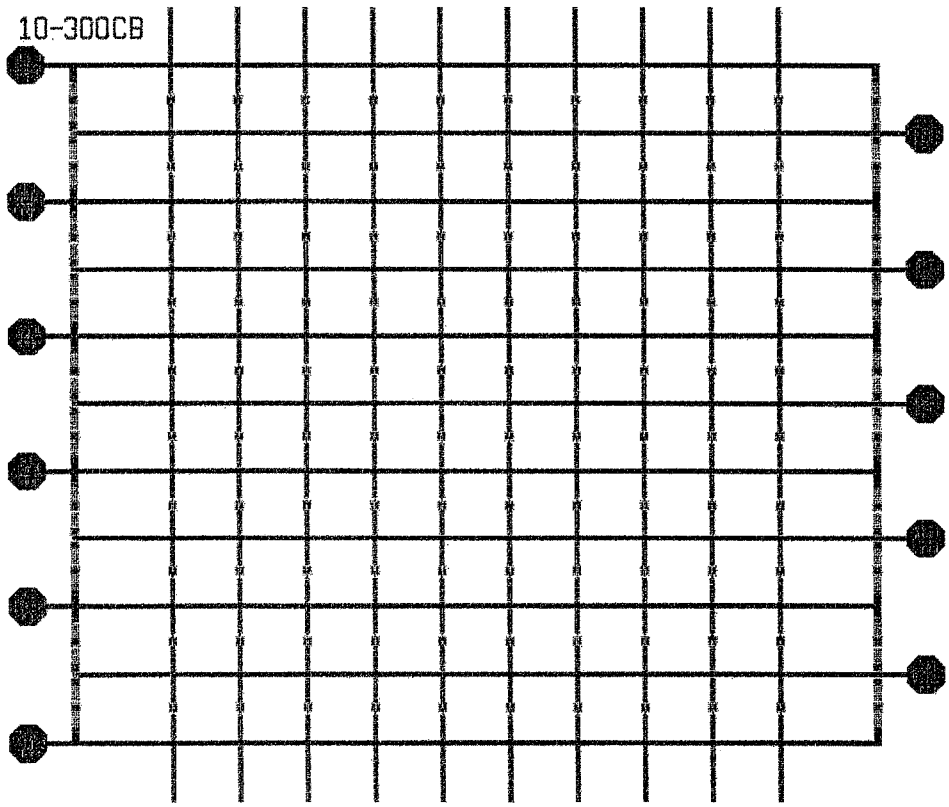

Fig. 2.27. A 100-element 300 GHz monolithic SCRTD grid oscillator. The unit cell size is 107 μm.

Measurements at frequencies this high are difficult to perform. Fig. 2.29 shows a setup that could be used to test the SCRTD grids. A Fabry-Perot interferometer is used to determine the oscillation frequency. The radiated power is detected by a thin-film bolometric detector, which consists of a film of bismuth evaporated onto a thin mylar membrane. Millimeter-wave power density measurements have been reported with this type of detector, with an estimated accuracy of 5% [41].

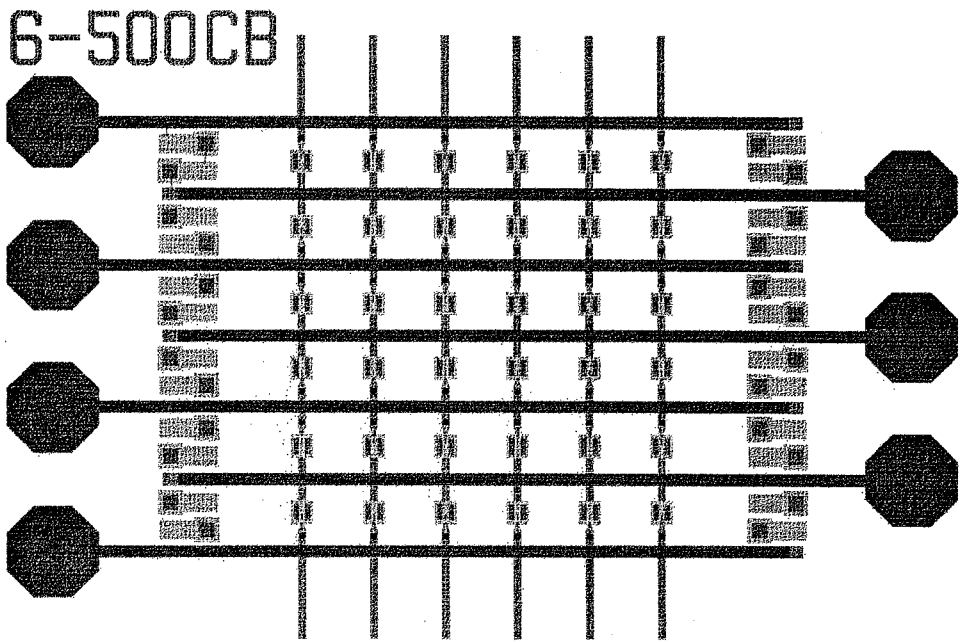

Fig. 2.28. A 36-element 500 GHz monolithic SCRTD grid oscillator. The unit cell size is 47 μm.

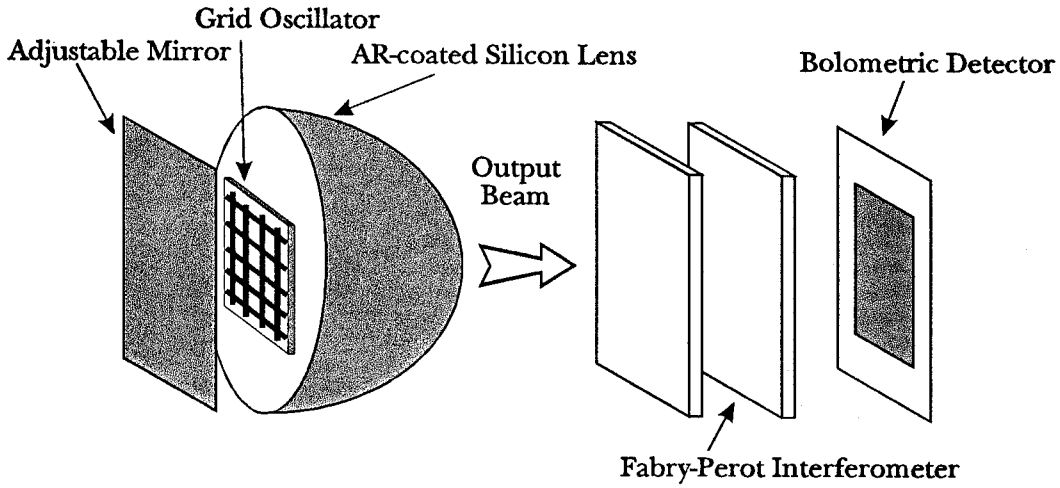

Fig. 2.29. Proposed measurement setup for testing the SCRTD grid oscillators.

2.6. Aside—A Brief Investigation of Transistor Oscillator Grids

Over the years, a number of successful transistor grid oscillators have been demonstrated. Commercially-available packaged devices are most easily inserted into the source-feedback configuration [28,42], as shown in Fig. 2.30(a). Another configuration, gate feedback, can be used with devices in chip form [34,43]. The equivalent circuits for these two configurations differ only in the way the device terminals are attached. Fig. 2.31 shows the equivalent circuits for both, using the numerical values derived in [28]. Notice that to the right of the transformer, these circuits are identical to the one used for the tunnel diode grid. Everything to the left of and including the center-tapped transformer can be thought of as a two-terminal active device.

Fig. 2.32 plots the resistance seen looking into the transformer as a function of frequency. The device S-parameters are those of a Fujitsu FSC11-series MESFET [44]. While it is true that the simple circuits in Fig. 2.31 are probably not

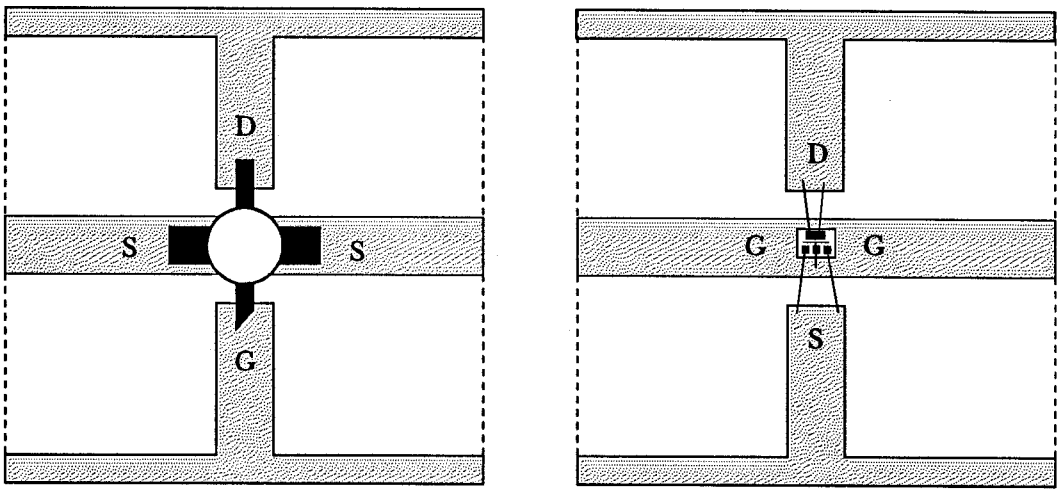

Fig. 2.30. Transistor oscillator grid unit cells: source feedback configuration (a) and gate feedback configuration (b).

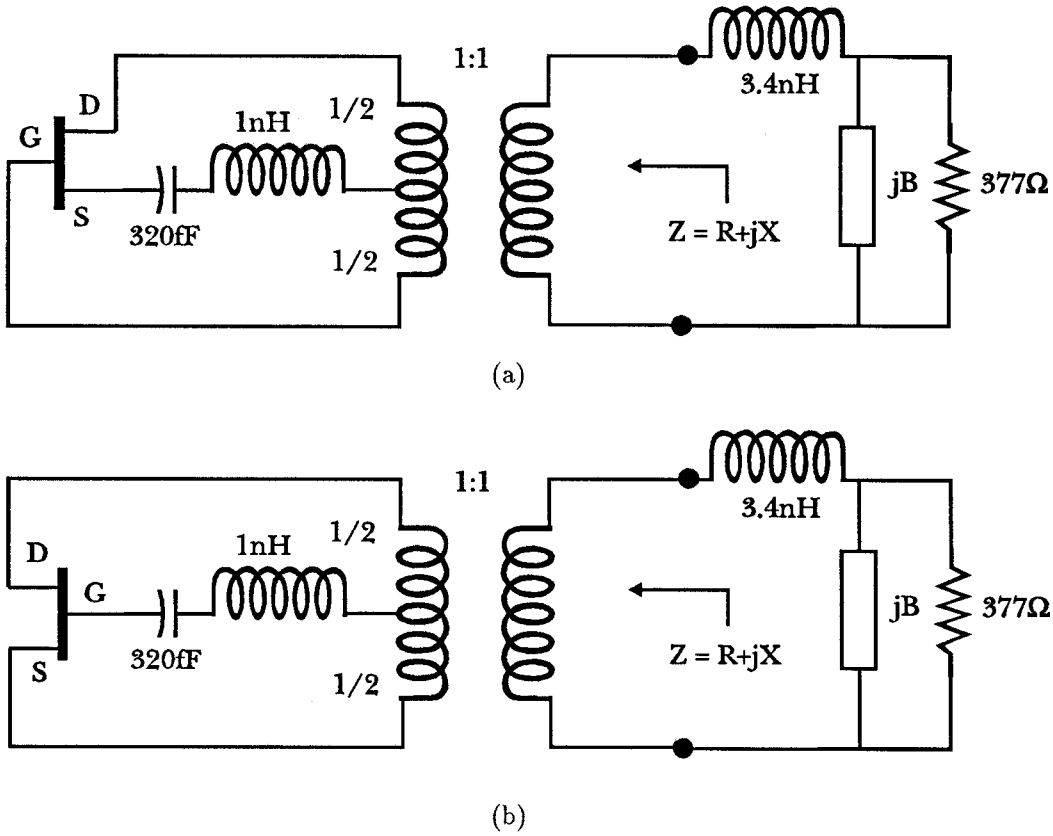

Fig. 2.31. Equivalent circuit for the oscillator grid using the numerical values in [28]. Source feedback configuration (a) and gate feedback configuration (b).

valid over the entire 12-GHz frequency range plotted, the result is nonetheless interesting. In the source-feedback configuration, the active device resistance is negative for almost the entire range. While negative resistance is not a necessary condition for instability, it is sufficient. This means that, as modelled, the source-feedback circuit is capable of oscillating from dc up to above 12 GHz, except possibly near 9.5 GHz. On the other hand, in the gate-feedback configuration the opposite is true. The device is most likely to oscillate when the resistance is negative, near 9.5 GHz. In both cases, the resistance changes sign near the resonant frequency of the L-C circuit in the center tap of the transformer, 8.9 GHz. This simple exercise shows that one can think of a source-feedback transistor grid as similar to a broadband NDR grid, while a gate-feedback grid is more like a narrowband, or tuned, NDR oscillator.

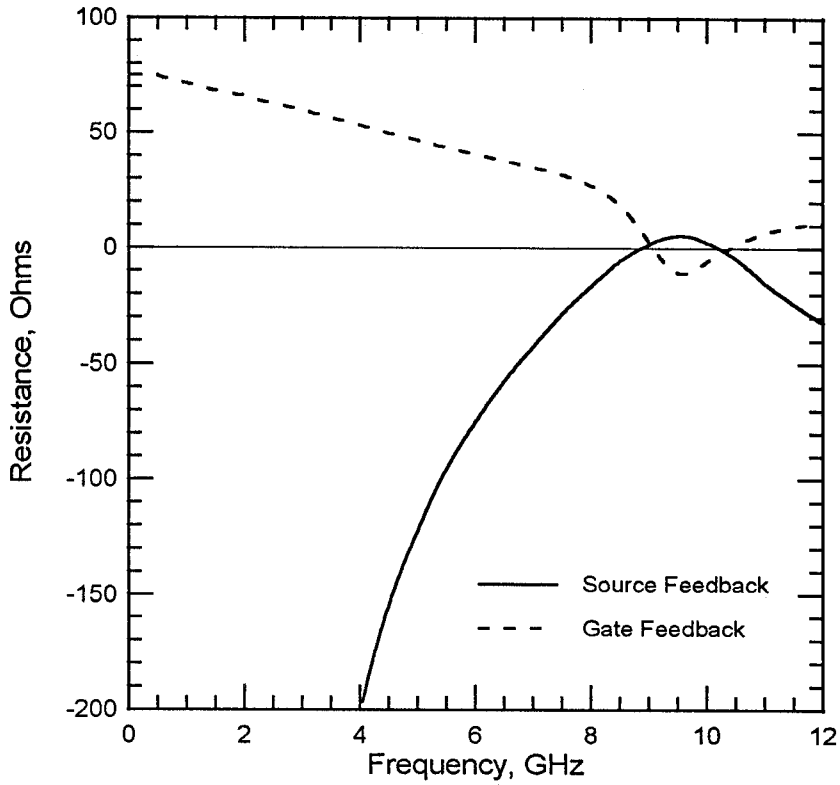

Fig. 2.32. Resistive part of the input impedance of the circuits of Fig. 2.31. The transistor is a Fujitsu FSC11-series MESFET.

References

[1] M. Sokolski, C.A. Kukkonen, "Overview of NASA's Terahertz Technology Program," *First Int. Symp. Space Terahertz Tech. Proc.*, pp. 33–68, 1990.

[2] M. Kaplan, "NASA Program Plans for Submillimeter-wave Astrophysics Program," *Second Int. Symp. Space Terahertz Tech. Proc.*, pp. 1–16, 1991.

[3] M.A. Frerking, "The Submillimeter Mission (SMMM) Heterodyne Instrument," *Second Int. Symp. Space Terahertz Tech. Proc.*, pp. 17–31, 1991.

[4] P. Siegel, "EOS MLS: A View from the Front," *Second Int. Symp. Space Terahertz Tech.*, pp. 32–56, 1991.

[5] T.G. Phillips, J. Keene, "Submillimeter Astronomy," *Proc. IEEE*, vol. 80, pp. 1662–1678, Nov. 1992.

[6] J.W. Waters, "Submillimeter-Wavelength Heterodyne Spectroscopy and Remote Sensing of the Upper Atmosphere," *Proc. IEEE*, vol. 80, pp. 1679–1701, Nov. 1992.

[7] A.V. Räisänen, "Frequency Multipliers for Millimeter and Submillimeter Wavelengths," *Proc. IEEE*, vol. 80, pp. 1842–1852, Nov. 1992.

[8] J.-C. Chiao, A. Markelz, Y. Li, J. Hacker, T. Crowe, J. Allen, D. Rutledge, "Terahertz Grid Frequency Doublers," presented at *The 6th Int. Symp. Space Terahertz Tech.*, March 1995.

[9] E.R. Brown, K.A. McIntosh, K.B. Nichols, C.L. Dennis, "Photomixing up to 3.8 THz in Low-Temperature-Grown GaAs," *Applied Physics Lett.*, vol. 66, pp. 285–287, Jan. 1995.

[10] E.R. Brown, T.C.L.G. Sollner, C.D. Parker, W.D. Goodhue, C.L. Chen, "Oscillations up to 420 GHz in GaAs/AlAs Resonant Tunneling Diodes," *Applied Physics Lett.*, vol. 55, pp. 1777–1779, Oct. 1989.

[11] E.R. Brown, J.R. Söderström, C.D. Parker, L.J. Mahoney, K.M. Molvar, T.C. McGill, "Oscillations up to 720 GHz in InAs/AlSb Resonant-Tunneling Diodes," *Applied Physics Lett.*, vol. 58, pp. 2291–2293, May 1991.

[12] Y. Konishi, S.T. Allen, M. Reddy, M.J.W. Rodwell, R.P. Smith, J. Liu, "AlAs/GaAs Schottky-Collector Resonant-Tunnel-Diodes," *Solid-State Electronics*, vol. 36, pp. 1673–1676, Dec. 1993.

[13] R.P. Smith, S.T. Allen, M. Reddy, S.C. Martin, J. Liu, R.E. Muller, M.J.W. Rodwell, "0.1 μm Schottky-Collector Alas/GaAs Resonant Tunneling Diodes," *IEEE Electron Device Lett.*, vol. 15, pp. 295–297, Aug. 1994.

[14] M. Reddy, M.J. Mondry, M.J.W. Rodwell, S.C. Martin, R.E. Muller, R.P. Smith, D.H. Chow, J.N. Schulman, "Fabrication and dc, Microwave Characteristics of Submicron Schottky-Collector AlAs/$In_{0.53}Ga_{0.47}As$/InP Resonant Tunneling Diodes," *J. Applied Physics*, vol. 77, pp. 4819–4821, May 1995.

[15] D.P. Steenson, R.E. Miles, R.D. Pollard, J.M. Chamberlain, M. Henini, "Demonstration of Power Combining at W-Band from GaAs/AlAs Resonant Tunneling Diodes," *Fifth Int. Symp. Space Terahertz Tech. Proc.*, pp. 756–767, 1995.

[16] O. Borić-Lubecke, D.-S. Pan, T. Itoh, "RF Excitation of an Oscillator with Several Tunneling Devices in Series," *IEEE Microwave and Guided Wave Lett.*, vol. 4, pp. 364–366, Nov. 1994.

[17] O. Borić-Lubecke, D.-S. Pan, T. Itoh, "Fundamental and Submarining Excitation for an Oscillator with Several Tunneling Diodes in Series," *IEEE Trans. Microwave Theory Tech.*, vol. 43, pp. 969–976, April 1995.

[18] C. Kinder, I. Mehdi, J.R. East, G.I. Haddad, "Power and Stability Limitations of Resonant Tunneling Diodes," *IEEE Trans. Microwave Theory Tech.*, vol. 38, pp. 864–872, July 1990.

[19] C. Kinder, I. Mehdi, J.R. East, G.I. Haddad, "Bias Circuit Instabilities and their Effect on the d.c. Current-Voltage Characteristics of Double-Barrier Resonant Tunneling Diodes," *Solid-State Electronics*, vol. 34, pp. 149–156, Feb. 1991.

[20] L. Esaki, "New Phenomenon in Narrow Germanium p-n Junctions," *Physical Rev.*, second series, vol. 109, pp. 603–604, Jan. 1958.

[21] L. Esaki, "Long Journey into Tunneling," Nobel lecture, in *Proc. IEEE*, vol. 62, pp. 825–831, June 1974.

[22] Z.B. Popović, D.B. Rutledge, "Diode Grid Oscillators," *1988 IEEE AP-S Int. Symp. Dig.*, pp. 442–445, 1988.

[23] R.A. York, R.C. Compton, "Quasi-Optical Power Combining Using Mutually Synchronized Oscillator Arrays," *IEEE Trans. Microwave Theory Tech.*, vol. 39, pp. 1000–1009, June 1991.

[24] A.C. Davidson, F.W. Wise, R.C. Compton, "A 60-GHz IMPATT Oscillator Array with Pulsed Operation," *IEEE Trans. Microwave Theory Tech.*, vol. 41, pp. 1845–1850, Oct. 1993.

[25] S. Yngvesson, *Microwave Semiconductor Devices*, Kluwer Academic Publishers, Boston, 1991, pp. 23–126.

[26] S.M. Sze, *Physics of Semiconductor Devices*, second ed., John Wiley & Sons, Inc., New York, 1981, pp. 513–678.

[27] Germanium Power Devices Corp., *Tunnel Diode Specifications*, Andover, MA.

[28] Z.B. Popović, R.M. Weikle, M. Kim, D.B. Rutledge, "A 100-MESFET Planar Grid Oscillator," *IEEE Trans. Microwave Theory Tech.*, vol. 39, pp. 193–200, Feb. 1991.

[29] R.M. Weikle, "Quasi-Optical Planar Grids for Microwave and Millimeter-wave Power Combining," Ph.D. Thesis, California Institute of Technology, Pasadena, CA, 1992.

[30] R.D. Martinez, R.C. Compton, "A General Approach for the S-Parameter Design of Oscillators with 1 and 2-Port Active Devices," *IEEE Trans. Microwave Theory Tech.*, vol. 40, pp. 596–574, March 1992.

[31] *The AARL Antenna Handbook*, G. Hall, ed., The American Radio Relay League, Newington, CT, 1988, pp. 9.1–9.12.

[32] J.D. Kraus, *Antennas*, second ed., McGraw-Hill Book Co., New York, 1988, pp. 48–61.

[33] M. Gouker, "Toward Standard Figures-of-Merit for Spatial and Quasi-Optical Power-Combined Arrays," *IEEE Trans. Microwave Theory Tech.*, vol. 43, pp. 1614–1617, July 1995.

[34] J.B. Hacker, M.P. De Lisio, M. Kim, C.-M. Liu, S.-J. Li, S.W. Wedge, D.B. Rutledge, "A 10-Watt X-Band Grid Oscillator," *1994 IEEE MTT-S Int. Microwave Symp. Dig.*, pp. 823–826, 1994.

[35] P.S. Linsay, "Period Doubling and Chaotic Behavior in a Driven Anharmonic Oscillator," *Physical Review Lett.*, vol. 47, pp. 1349–1352, Nov. 1981.

[36] E.S. Hellman, K.L. Lear, J.S. Harris, Jr., "Limit Cycle Oscillation in Negative Differential Resistance Devices," *J. Applied Physics*, vol. 64, pp. 2798–2800, Sept. 1988.

[37] E.A. Hosny, A.A.A. Nasser, M.I. Sobhy, "Analysis of Chaotic Behavior in Lumped-Distributed Circuits Applied to Practical Microwave Oscillators," *1995 IEEE MTT-S Int. Microwave Symp. Dig.*, pp. 1569–1572, 1995.

[38] J.P. Gollub, T.O. Brunner, B.G. Danly, "Periodicity and Chaos in Coupled Nonlinear Oscillators," *Science*, vol. 200, pp. 48–50, April 1978.

[39] D.W. Griffin, "Monolithic Active Array Limitations Due to Substrate Modes," *1995 IEEE AP-S Int. Symp. Dig.*, pp. 1300–1303, 1995.

[40] M. Reddy, R.Y. Yu, H. Kroemer, M.J.W. Rodwell, S.C. Martin, R.E. Muller, R.P. Smith, "Bias Stabilization for Resonant Tunnel Diode Oscillators," *IEEE Microwave Guided Wave Lett.*, vol. 7, pp. 219–221, July 1995.

[41] K.A. Lee, Y. Guo, P.A. Stimson, K.A. Potter, J.-C. Chiao, D.B. Rutledge, "Thin-Film Power-Density Meter for Millimeter Wavelengths," *IEEE Trans. Antennas and Propagation*, vol. 39, pp. 425–428, March 1991.

[42] T. Mader, S. Bundy, Z.B. Popović, "Quasi-Optical VCO's," *IEEE Trans. Microwave Theory Tech.*, vol. 41, pp. 1775–1781, Oct. 1993.

[43] R.M. Weikle, M. Kim, J.B. Hacker, M.P. De Lisio, D.B. Rutledge, "Planar MESFET Grid Oscillators Using Gate Feedback," *IEEE Trans. Microwave Theory Tech.*, vol. 40, pp. 1997–2003, Nov. 1992.

[44] Fujitsu Microelectronics, Inc., *1989/90 Microwave Semiconductors Data Book*, San Jose, CA.

Chapter 3

Hybrid X-Band pHEMT Amplifier Grid

In this chapter, a 100-element hybrid X-band amplifier grid is discussed. The active devices are custom-made pseudomorphic High Electron Mobility Transistor (pHEMT) differential-pair chips fabricated by Lockheed Martin Laboratories. A model useful for gain analysis and design will be presented. Chip resistors were used in the gate leads to suppress common-mode oscillations. The measured gain was 10 dB at 10 GHz. When tuned to operate at 9 GHz, the peak gain was 12 dB with a 15% 3-dB bandwidth. The grid can accept beams with incidence angles up to 25° with less than a 3-dB gain reduction. The minimum noise figure was 3 dB at 10 GHz. The saturated output power was 3.7 W at 9 GHz, with a peak power-added efficiency of 12%. These results are a significant improvement over previous amplifier grids using Heterojunction Bipolar Transistors (HBT's).

3.1. Introduction

Quasi-optical amplifiers combine the output powers of many solid-state devices in free space, eliminating the conductor losses associated with transmission-line or waveguide combiners. The first successful quasi-optical amplifier was a 25-element grid of MESFET pairs developed by Moonil Kim at Caltech [1]. A grid amplifier is an array of closely spaced differential pairs of transistors. Fig. 3.1 shows the approach. A horizontally polarized beam excites rf currents on the

input leads of the grid. This drives the transistor pair in the differential mode. Currents on the output leads produce a vertically polarized output beam. Metal-strip polarizers provide independent tuning of the amplifier's input and output circuits. Following this MESFET grid amplifier was a 100-element HBT grid amplifier, also developed by Moonil Kim [2]. Unlike the MESFET grid, this grid had a completely planar structure, making it more suitable for monolithic fabrication. This grid had a gain of 10 dB at 10 GHz, as shown in Fig. 3.2. The noise figure was 7 dB and the saturated output power was 450 mW. As discussed

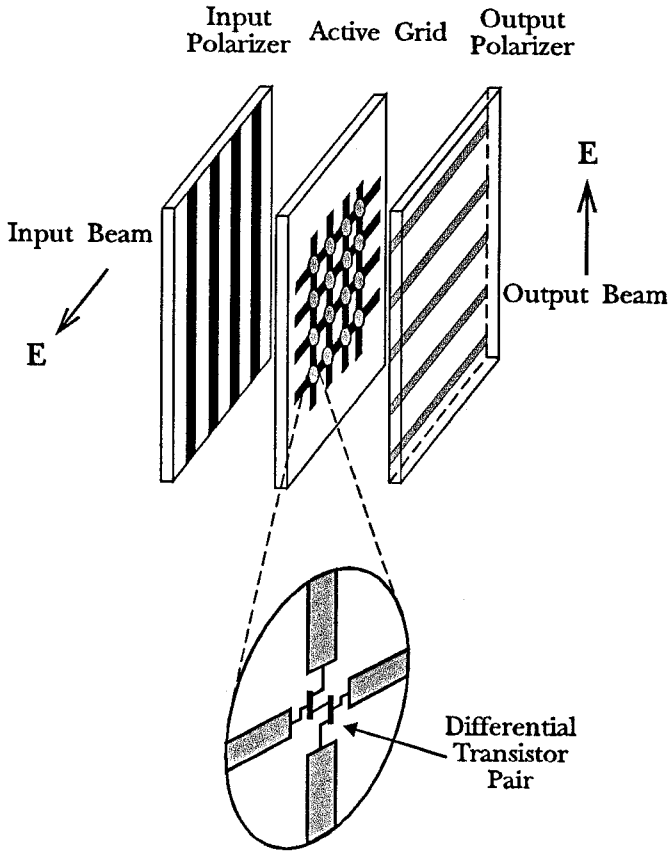

Fig. 3.1 A grid amplifier. A horizontally polarized input beam is incident from the left. The output beam is vertically polarized and is radiated to the right. The polarizers independently tune the input and output circuits.

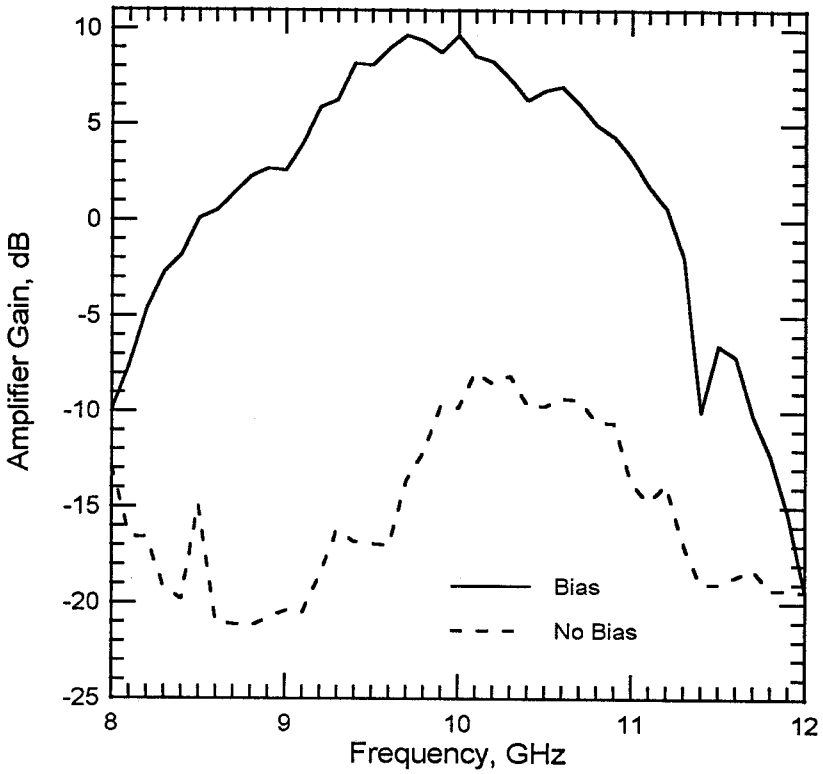

Fig. 3.2. Gain versus frequency for the 100-element HBT grid amplifier [2].

in the first chapter, many other types of quasi-optical amplifiers have been developed using back-to-back integrated horn antennas [3,4], probe antennas [5], patch antennas [6–13], and slot antennas [14–16], leading to a rapid development of quasi-optical technology.

pHEMT technology has also developed rapidly. Millimeter-wave pHEMT's are capable of high gain, high output power, high efficiency, and low noise figure, making them the device of choice for many high-frequency applications [17–20]. The first successful pHEMT grid amplifiers were 16-element arrays reported in [21]. This chapter will discuss the modelling and performance of a full-size 100-element pHEMT grid amplifier.

3.2. Amplifier Grid Modelling

An interesting property of grid amplifiers is that, to first order, the unit cell determines the driving-point impedances seen by the device, while the power scales with the grid area. This allows one to optimize for gain and noise figure by the choice of the unit cell, and to independently select the total grid size to meet the power requirement. The design of previous grid amplifiers has primarily been empirical [1,2]. For the 100-element HBT grid amplifier, a number of prototype 16-element grids were built and tested [22]. The unit cell used for the final full-size grid was the one that gave the best results. If grid amplifiers are ever to be confidently designed, a reliable model must be developed.

Consider the grid amplifier configuration shown in Fig. 3.3(a). The grid is constructed on a substrate with a relative dielectric constant ε and a thickness t_s. The input and output polarizers are located a distance t_i and t_o from the grid. To simplify this example, the polarizers are metallic gratings suspended in free space. A sample unit cell is shown in Fig. 3.3(b). This is a less complicated version of the cell presented in [2]. The transistors are assumed to be FET's. Horizontal leads are connected to the gates of the transistor pair and vertical leads are connected to the drains. Bias to the source and drain is provided along the thin lines.

A rather intuitive transmission-line equivalent circuit for this configuration is proposed in Fig. 3.4(a). Free space is represented by the resistors, with characteristic impedance η_o. For a square unit cell, $\eta_o = 377\,\Omega$. The air gaps between the polarizers and the grid are represented by transmission lines with characteristic impedance η_o and appropriate electrical length. The substrate is also represented by a transmission line. The effect of the dielectric is to reduce the characteristic impedance by a factor of $\sqrt{\varepsilon}$, the index of refraction of the material, and to increase the electrical length by this same factor. The polarizers are assumed to be perfect—they present a short circuit to a wave polarized along

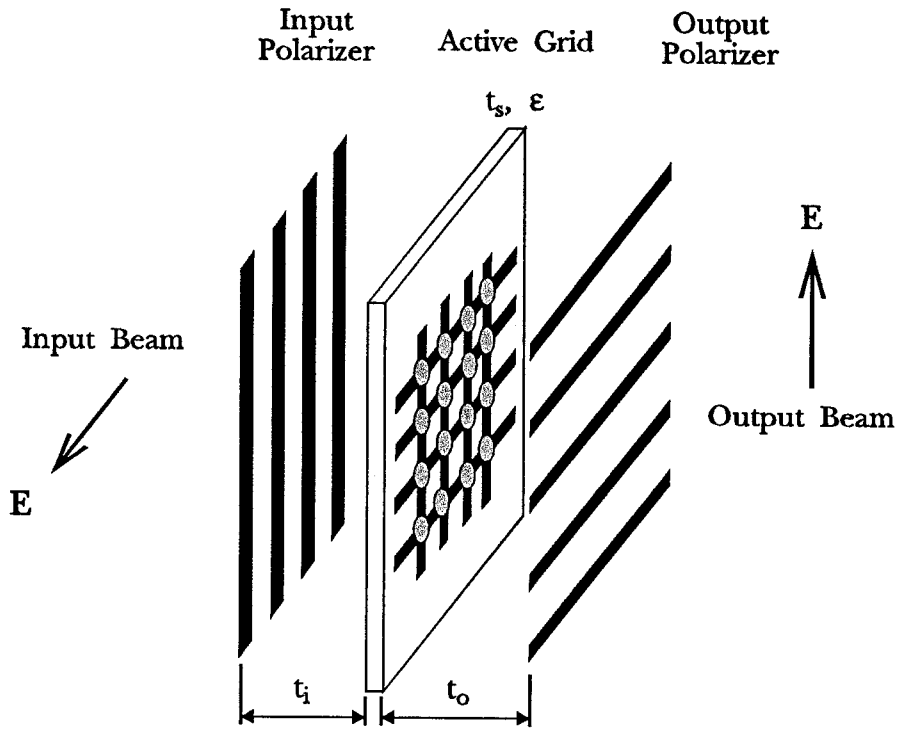

(a)

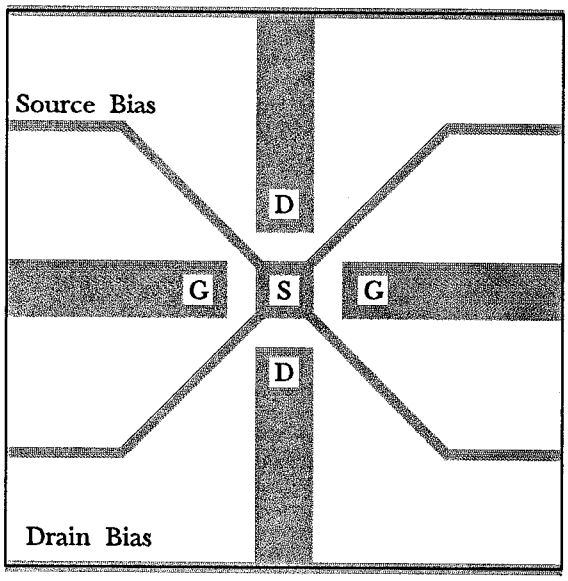

(b)

Fig. 3.3. Simplified assembled grid amplifier configuration (a) and unit cell (b).

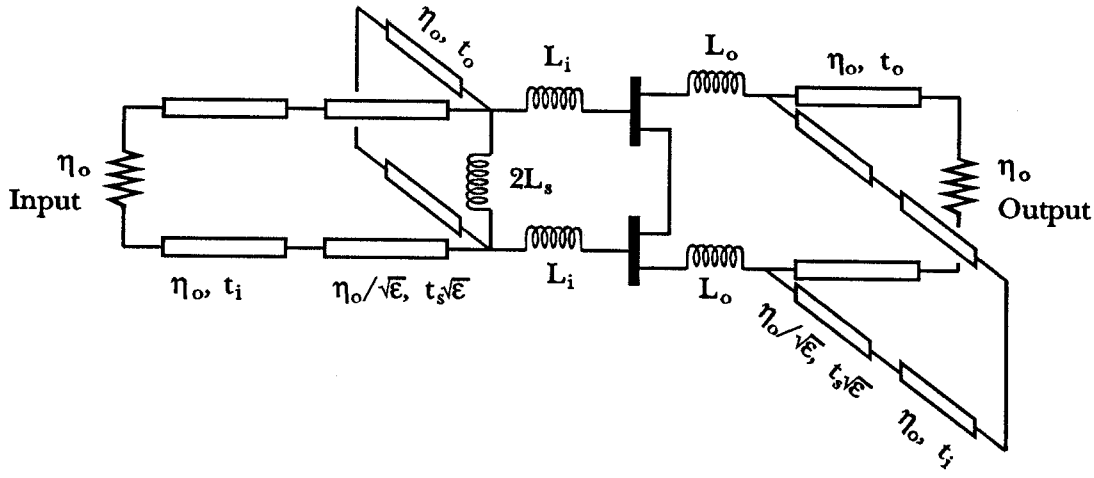

(a)

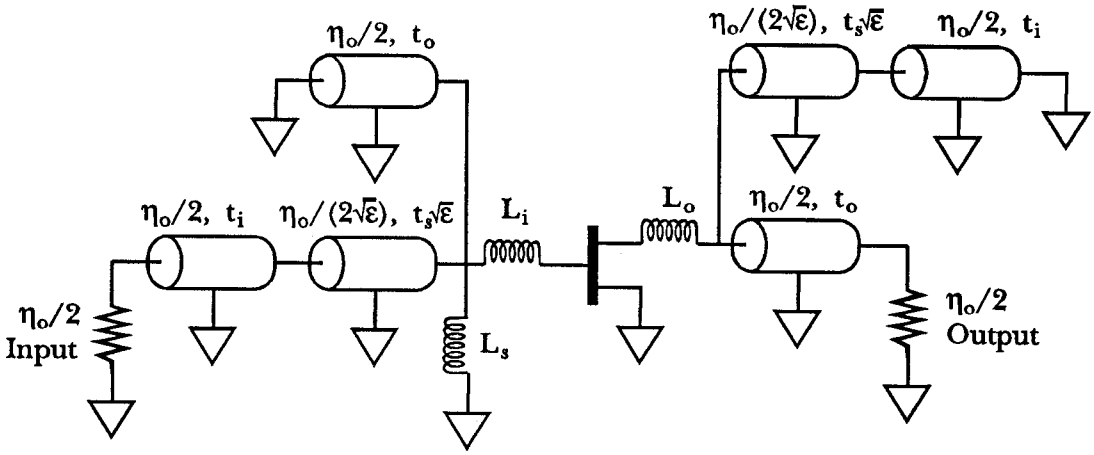

(b)

Fig. 3.4. Transmission-line equivalent circuit for the amplifier configuration shown in Fig. 3.3. The symmetry of the circuit allows one to simplify the full-cell model (a) to the half-cell model (b), where the transmission-line impedances are half their usual values.

the direction of the metal strips and they are invisible to a wave polarized orthogonal to the strips. The size and structure of the unit cell will determine the values of the remaining inductive elements. Coupling to the gates of the devices through the short horizontal leads is represented by the inductance L_i. The vertical output leads attached to the drains are modeled by the inductors labelled L_o. The thin bias lines are primarily horizontally directed. Therefore, they will appear at the input, and are represented by the shunt inductance L_s. It is clear that these lines should be made highly reactive to avoid shorting out the input of the grid. Numerical values for these reactive elements can be computed using any number of methods—from very simple quasi-static models to complicated moment method or finite-element techniques.

The circuit in Fig. 3.4(a) represents the full cell and therefore contains two transistors. The symmetry of this circuit allows one to bisect it along the horizontal symmetry plane with a virtual ground, resulting in the circuit shown in Fig. 3.4(b). This new circuit represents a half cell, containing only a single transistor. This simplifies the analysis because, often, it is the transistor model itself that is the most complicated part of the circuit. Bisecting the circuit results in the characteristic impedances of free space and all transmission lines becoming half of their usual values, while the effective lengths remain the same.

The model presented here is by no means intended to be complete. Rather, it is meant to provide a basis for understanding the more complicated equivalent circuit models which will be presented later. These circuits will include the effects of imperfect polarizers, dielectric tuning slabs, and other elements. In addition, the rather simple inductor network representing the coupling between the radiated waves and the device via the unit cell structure could be replaced with a more extensive one. Nevertheless, despite its apparent simplicity, this equivalent circuit has been used to design and model the behavior of a number of different amplifier grids with reasonable success [23–26].

3.3. Grid Design and Construction

The differential-pair chips used in this project were fabricated by Lockheed Martin Laboratories in Baltimore. The active devices are 0.1-μm AlGaAs/InGaAs/GaAs pHEMT's. The epitaxy employs a double-doped heterostructure optimized for high power. Fig. 3.5 shows a 0.1-μm T-gate. The gates were defined using an electron beam direct write system and a bi-level resist. The total gate width per transistor is 100 μm distributed among four fingers. The devices were passivated with SiN_x using Plasma-Enhanced Chemical Vapor Deposition (PECVD). Air-bridges and top-layer metallization were formed with several microns of electroplated gold. Further details regarding the device can be found in [17].

The differential-pair chip layout is shown in Fig. 3.6. The sources of two pHEMT's are tied together to form a differential pair. Unlike the HBT's in other

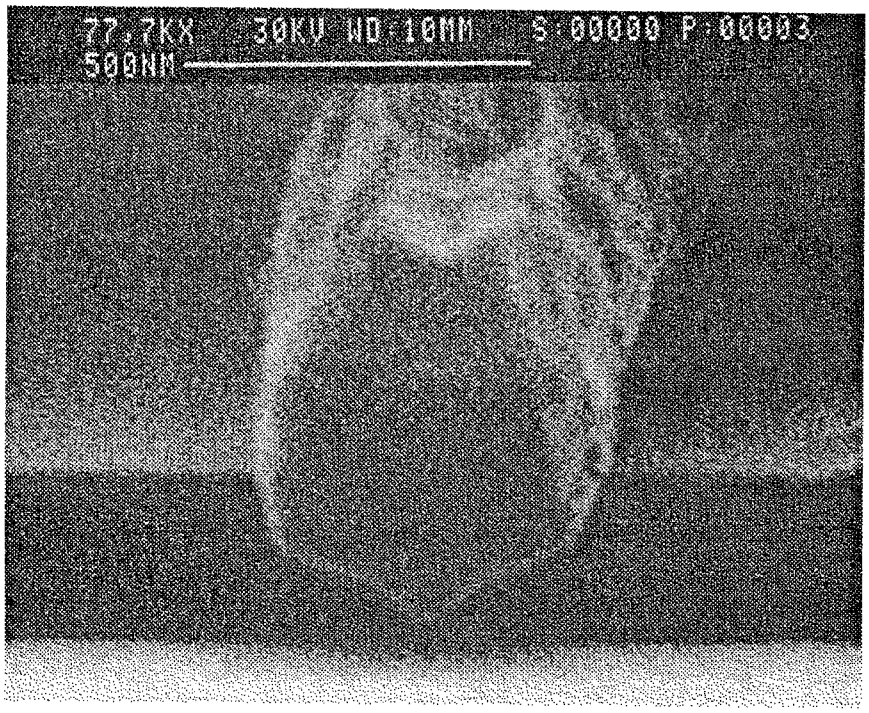

Fig. 3.5. SEM micrograph of a 0.1-μm mushroom gate [17].

grids, which were self-biased [2,24,25], the control terminal can be externally biased. The 1-kΩ resistor allows this gate control bias voltage to pass from cell to cell. This is possible because the gate draws very little bias current. The gate bias resistor passes under the air-bridged source connection. These devices are designed to be used as high as 100 GHz [17]. The 2-kΩ resistor and 0.5-pF capacitor are feedback elements to help stabilize the amplifier at X-band. The two 100-Ω source resistors are intended to reduce the common-mode gain. These resistors should not effect the differential-mode performance, but will reduce the overall efficiency of the amplifier. A photograph of the chip is shown in Fig. 3.7.

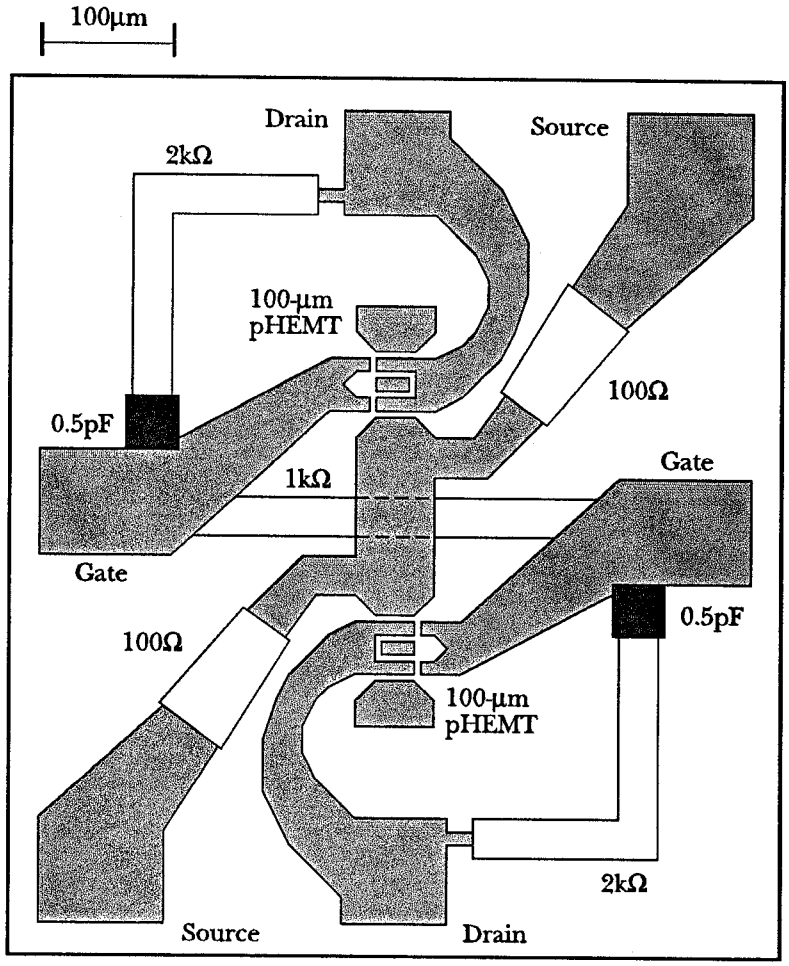

Fig. 3.6. The differential-pair chip layout.

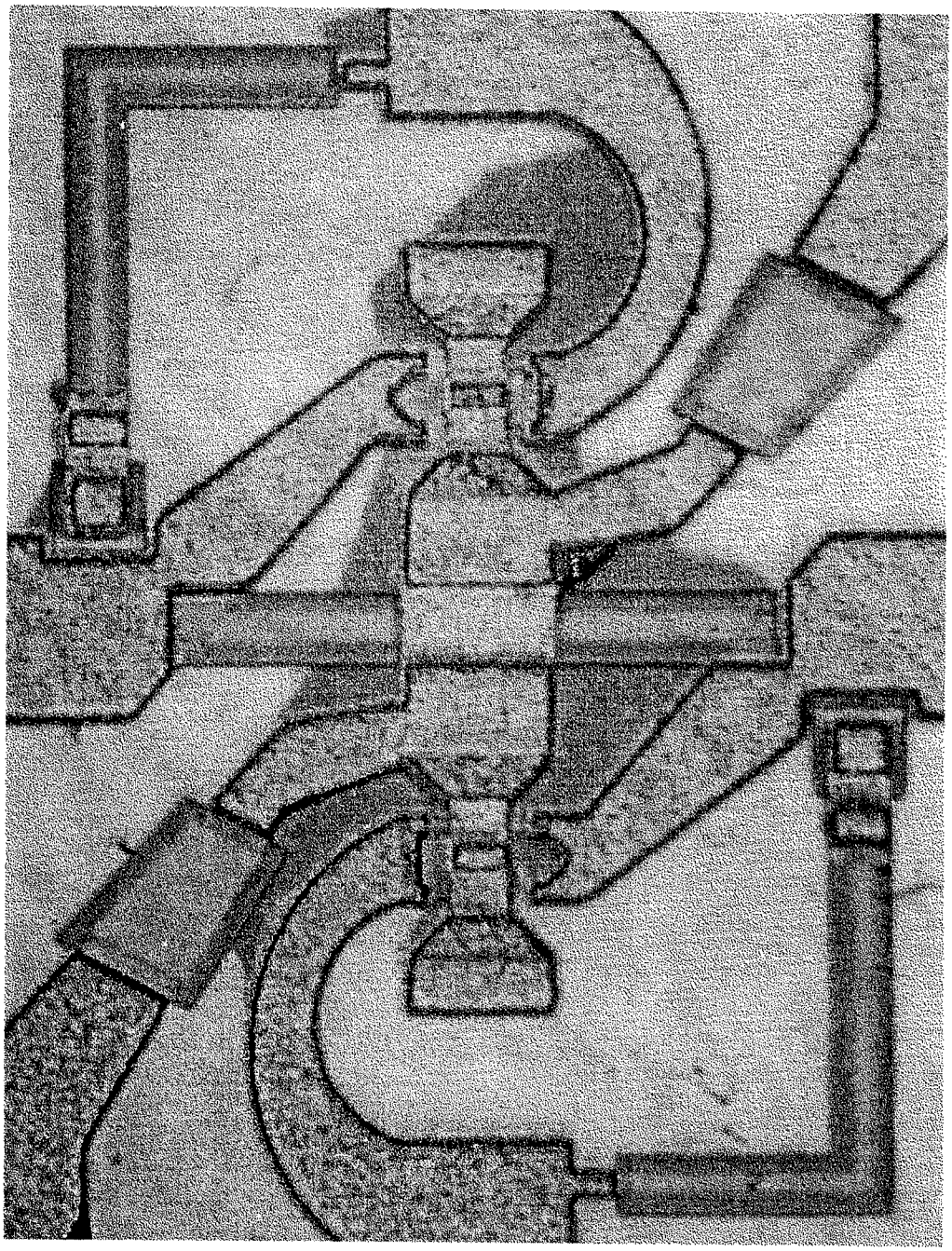

Fig. 3.7. Microscope photograph of the differential-pair chip. The chip is roughly 0.5 mm by 0.7 mm.

Fig. 3.8 shows the unit cell. The cell is 7.3 mm on a side. The input beam is coupled to the gates of the pHEMT's through the horizontal input leads, which also supply the gate bias. The output beam is radiated from the vertical drain leads. Both input and output leads are 0.4-mm wide. Bias to the drain and source is provided by the meandering lines, which are 0.2-mm wide. The bias lines are intended to present a rather high impedance to the input wave. The resistors in the gate leads suppress spurious common-mode oscillations and will be discussed later.

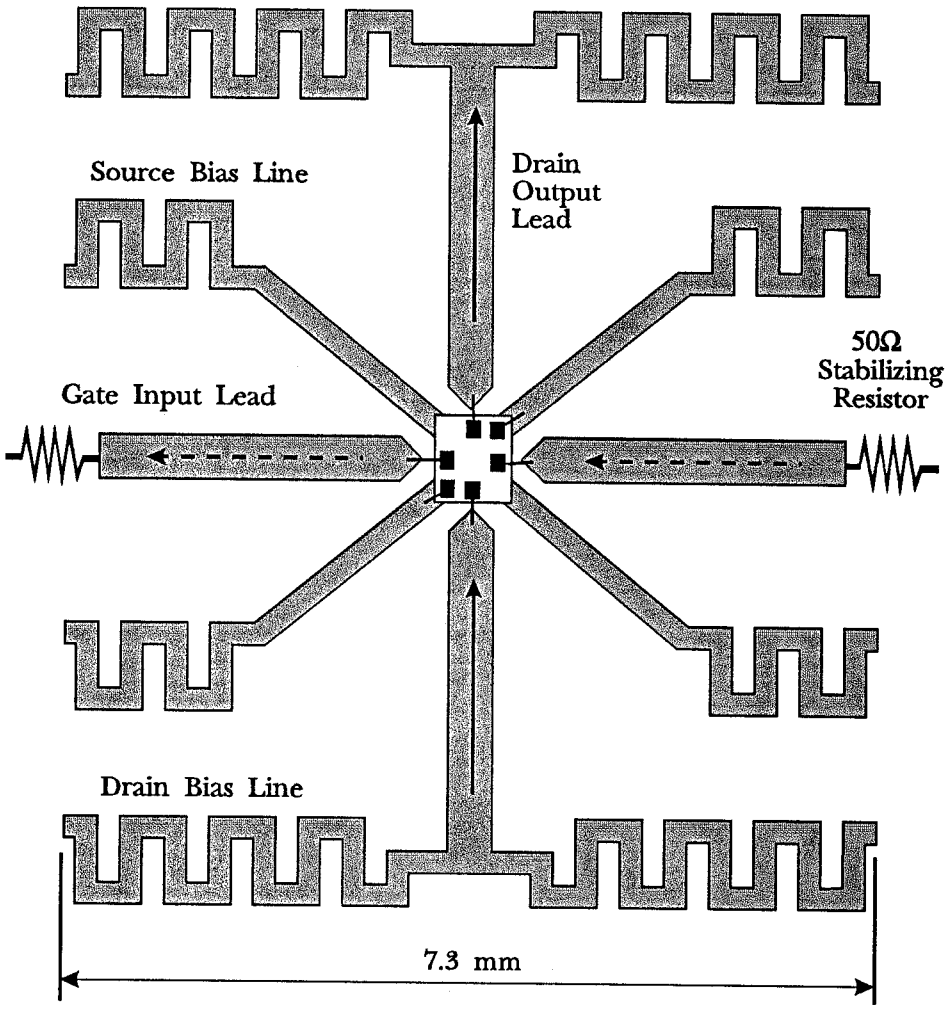

Fig. 3.8. The grid amplifier unit cell. Arrows indicate the direction of rf currents.

Based on the modelling discussions from the previous section, an equivalent circuit for this unit cell can be constructed. Fig. 3.9 shows the half-cell equivalent circuit. The circuit contains a single pHEMT, including the gate bias resistor R_{gb}, and the gate-drain feedback network R_f and C_f. Inductors L_i and L_o represent coupling through the input and output leads, and L_s models the effect of the bias lines. The oscillation-suppression resistor R_{st} in the gate lead appears in series with the input lead inductance L_i. Numerical values for L_i and L_o are computed by first using the method of moments to approximate the surface current distribution on the input and output leads. Once an estimate for the current distribution has been obtained, the driving-point impedance is calculated using the induced emf technique. More details regarding this method may be found in Appendix A. The numerical value for the shunt bias-line inductance L_s is empirically determined with the aid of Hewlett-Packard's High Frequency Structure Simulator (HFSS) [27].

An often-quoted figure of merit for potentially-unstable high-frequency transistors is the Maximum Stable Gain (MSG) [28,29]. The MSG is given by:

$$\mathrm{MSG} = \frac{|S_{21}|}{|S_{12}|}. \tag{3.1}$$

Fig. 3.10 plots the MSG for the pHEMT alone, using the equivalent circuit model for the device supplied by Lockheed Martin Laboratories. The MSG is over 18 dB at 10 GHz. The addition of resistors R_{st} and R_{gb}, and feedback elements R_f and C_f will tend to reduce the gain available from the transistor, but they do stabilize the device. For a stable transistor, one can quote the Maximum Available Gain (MAG):

$$\mathrm{MAG} = \frac{|S_{21}|}{|S_{12}|}(K - \sqrt{K^2 - 1}), \tag{3.2}$$

where K is the Rollett stability factor given by:

$$K = \frac{1 + |S_{11}S_{22} - S_{21}S_{12}|^2 - |S_{11}|^2 - |S_{22}|^2}{2|S_{21}||S_{12}|}. \tag{3.3}$$

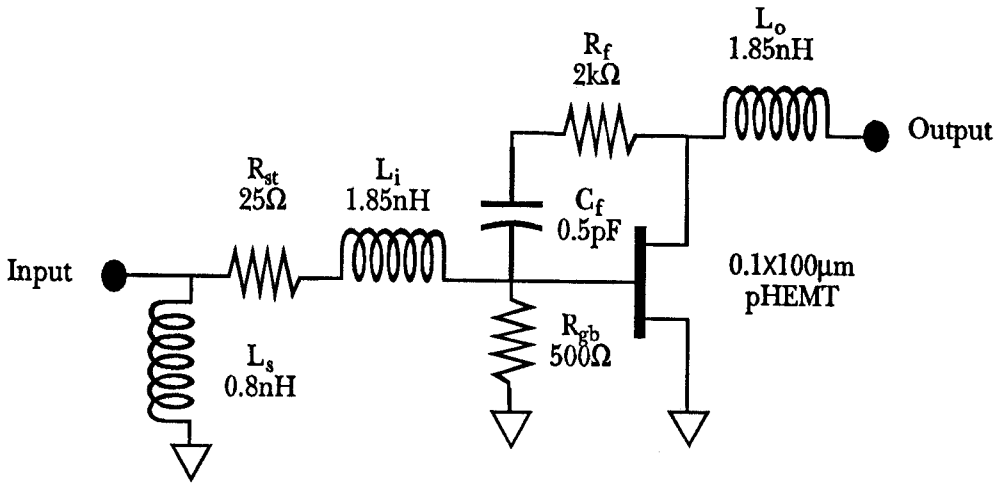

Fig. 3.9. Half-cell equivalent circuit model for the grid amplifier.

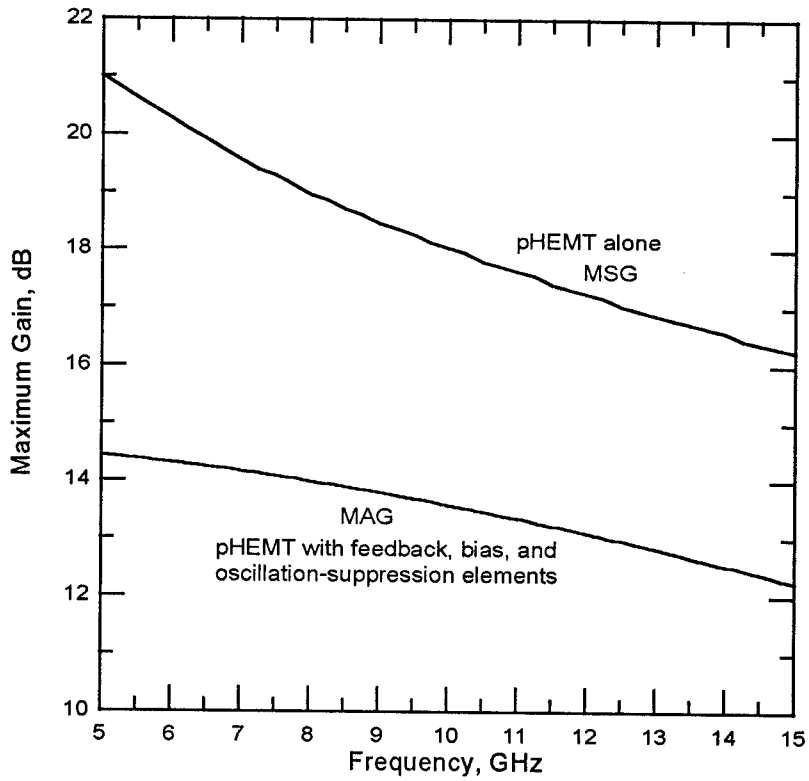

Fig. 3.10. Maximum stable gain of the pHEMT with and without the external bias, feedback, and stabilization elements.

For a stable device, $K > 1$. The MAG for the device including the bias, feedback, and stabilization elements is also plotted in Fig. 10. These elements reduce the gain available from the pHEMT by over 4.5 dB at 10 GHz.

A 10×10 array of these cells was etched onto a 15-mil Duroid substrate with a relative dielectric constant of 2.2. This thin board can then be attached to a second substrate, with a dielectric constant and thickness chosen to maximize the amplifier's electrical performance and mechanical integrity. The etched substrate was gold plated to facilitate wire bonding. The active chips were dc probed, and

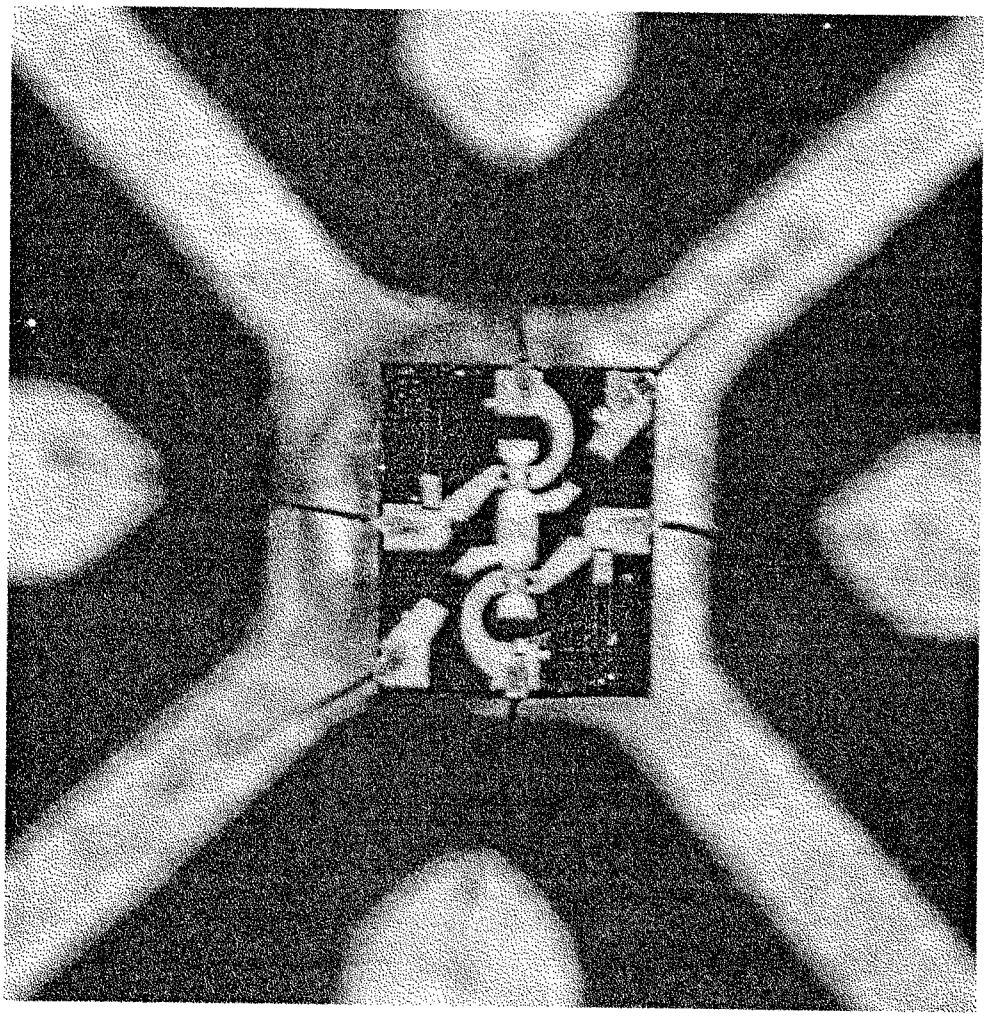

Fig. 3.11. Photograph of an active chip attached to the etched substrate.

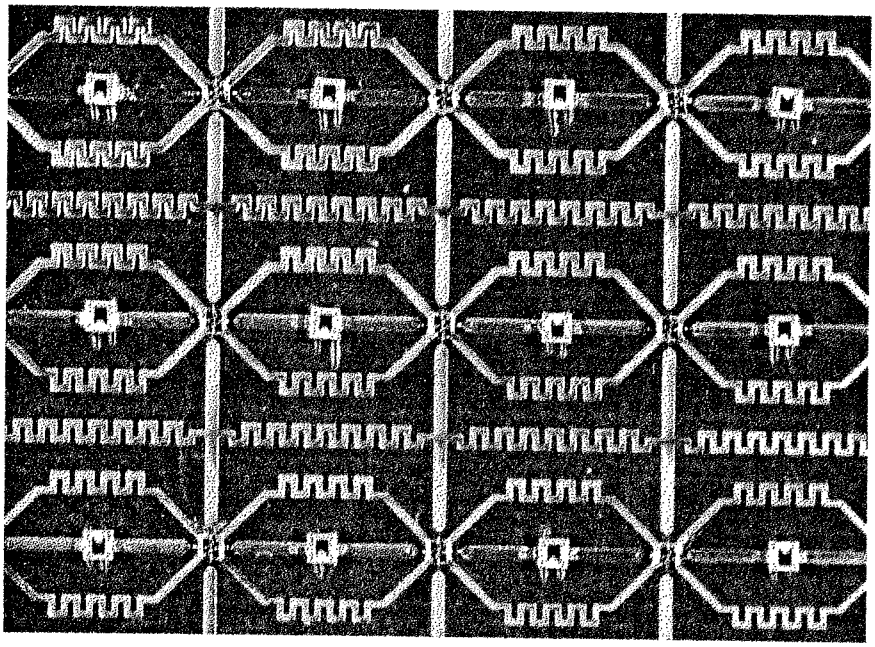

Fig. 3.12. Several unit cells. The cell size is 7.3 mm on a side.

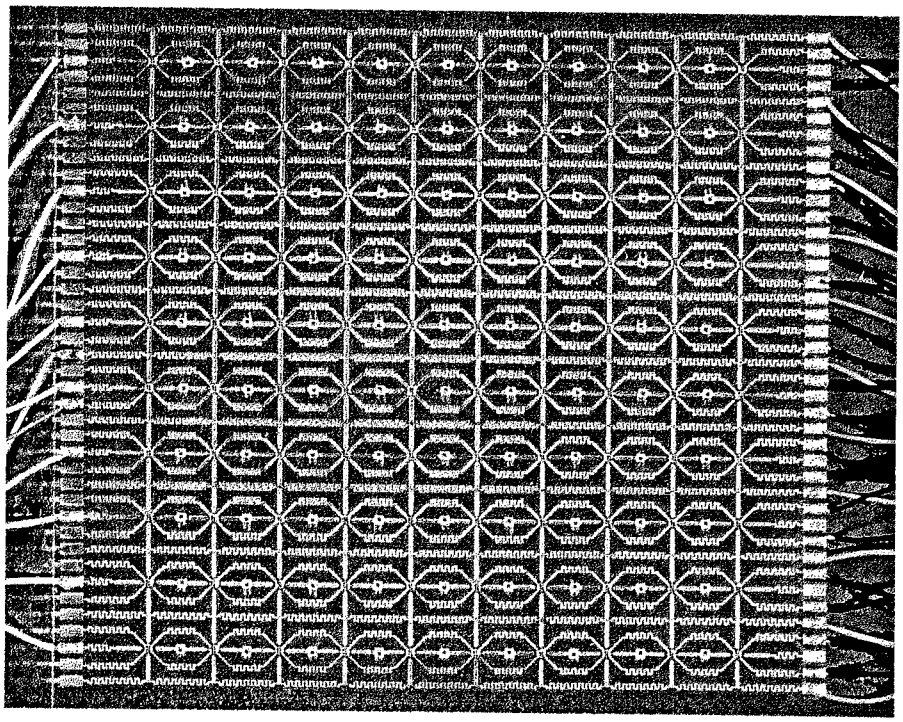

Fig. 3.13. The 100-element pHEMT grid amplifier. The active area is 7.3 cm on a side.

affixed to the grid with epoxy. The necessary electrical connections were made with wire bonds. Figs. 3.11 and 3.12 show the chips attached to the substrate in detail. Fig. 3.13 shows the entire 100-element pHEMT grid amplifier.

Initially, the grid suffered from 8–9 GHz oscillations, depending on the bias level. The onset of these oscillations was at a drain bias current of 9 mA per transistor—well below the device's usual operating point. The gain of the amplifier at the onset of oscillation was less than 4 dB. These oscillations were insensitive to the polarizer position and substrate thickness. This property, coupled with the measured radiation pattern, led to the conclusion that the instability was a common-mode oscillation like the one described in [24]. A model for these oscillations has been developed by Cheh-Ming Liu at Caltech. This model assumes that the transistor is operating in the common mode, which allows one to define a unit cell like the quarter cell in Fig. 3.14. A transmission-line equivalent circuit for the oscillation mode is shown in Fig. 3.15. Following the approach of

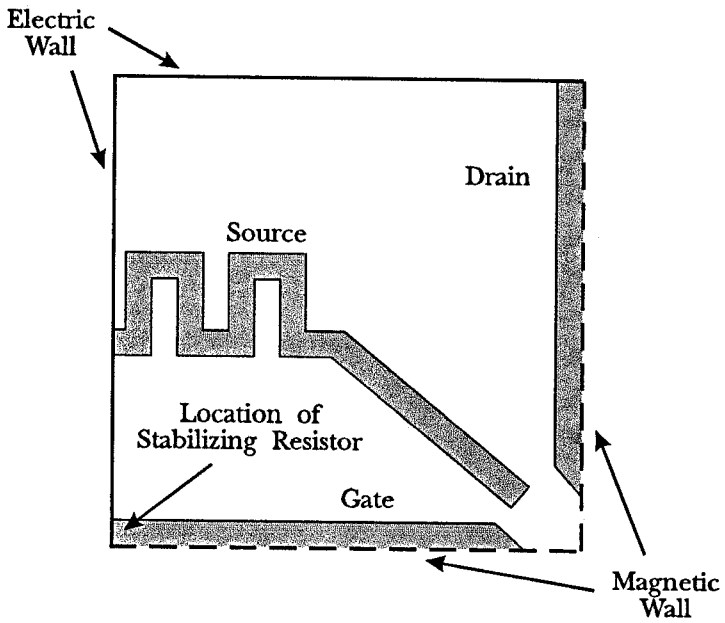

Fig. 3.14. Quarter cell. The boundary conditions are imposed by the grid symmetry.

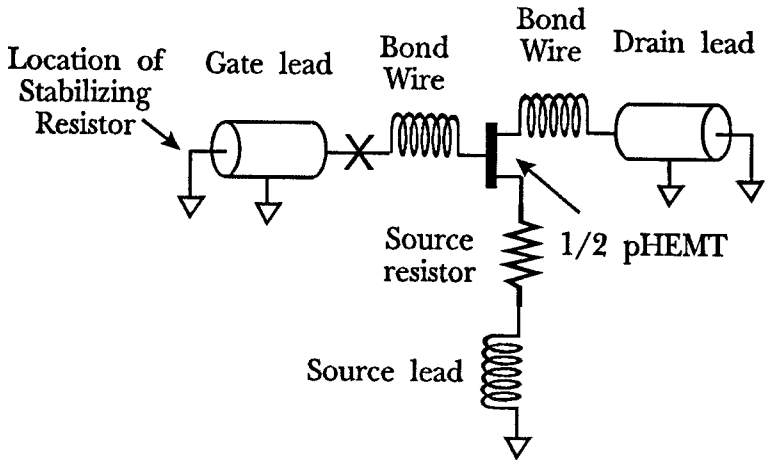

Fig. 3.15. Equivalent circuit model for the common-mode oscillation [24].

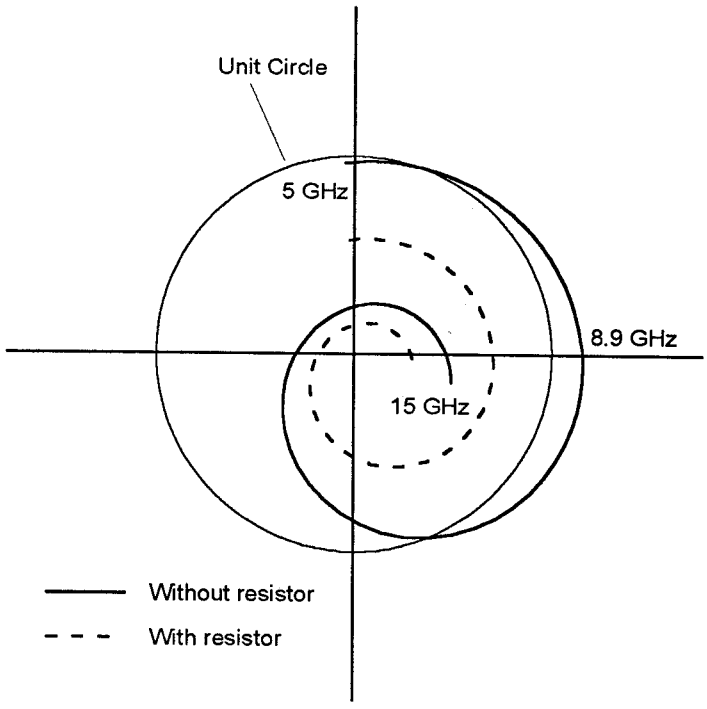

Fig. 3.16. Circular function of the amplifier grid. Without the gate resistors, the grid is unstable at 8.9 GHz. The stabilized amplifier has a gain margin of 3 dB.

Martinez and Compton [30], a circulator is inserted at the node marked with an $\times$ and the circular function is measured. The circular function, C, is plotted in Fig. 3.16. The circuit is theoretically unstable at 8.9 GHz because the magnitude of C is greater than unity and its phase is zero. This is close to where the actual oscillations occurred.

To suppress these oscillations, 50-Ω chip resistors were placed in the radiating gate lead, midway between transistor pairs. These resistors can be seen clearly in Fig. 3.12. With the resistors in place, the magnitude of C is less than unity, so the grid should be stable. After adding the resistors, the grid could be biased to a current of over 15 mA per transistor without oscillations. Unfortunately, these gate resistors will degrade the gain and noise figure of the amplifier. Theory indicates that the 100-Ω source resistors originally thought necessary to prevent common-mode oscillations may actually be contributing to the instability. Removal of the source resistors may result in a more stable amplifier, as well as a more efficient grid. Experiments investigating this are being performed by Alina Moussessian at Caltech.

3.4. Gain and Tuning

Two different techniques have been used to measure the gain of quasi-optical grid amplifiers. The first is a far-field approach shown in Fig. 3.17 [1,2]. The first step is to calibrate the system. This is done with the two horn antennas co-polarized, as shown in Fig. 3.17(a). Then, the amplifier gain is measured using the setup shown in Fig. 3.17(b). The amplifier gain G is related to the calibration power P_c and the power received with the grid in place P_r by:

$$G = \frac{P_r}{P_c}\left(\frac{\lambda R}{2A}\right), \tag{3.4}$$

where λ is the free-space wavelength, R is the spacing between the horn and the grid, and A is the physical area of the grid.

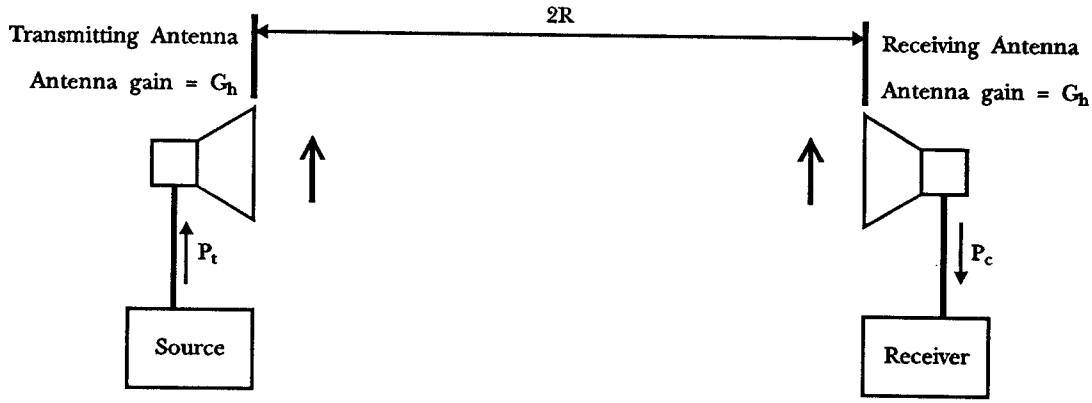

(a)

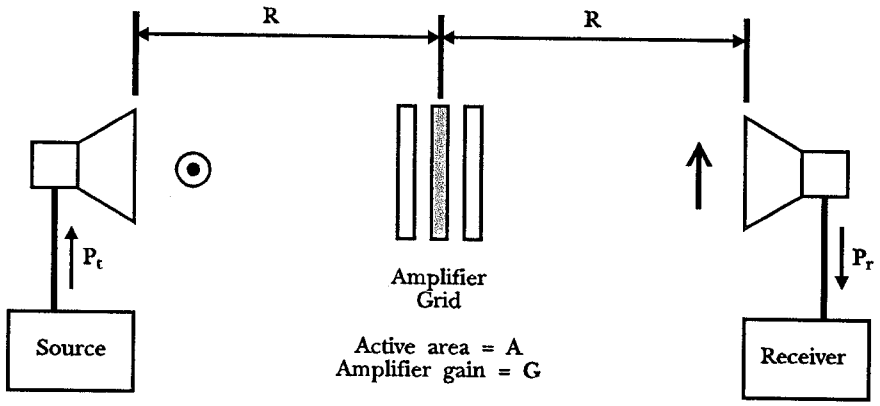

(b)

Fig. 3.17. Far-field setup used for gain measurement. The calibration step (a) is performed with the horns co-polarized. The measurement step (b) is performed with the horns cross-polarized.

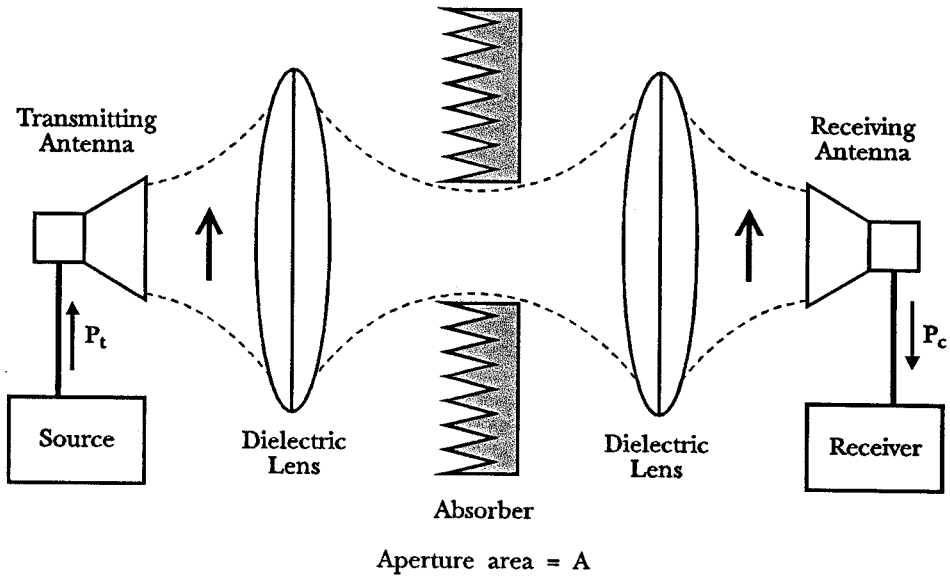

(a)

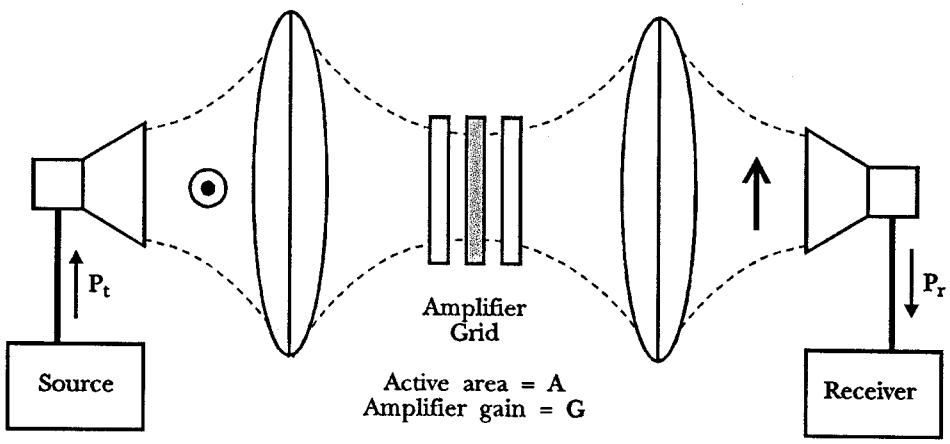

(b)

Fig. 3.18. Lens-focused setup used for gain measurement. The calibration step (a) is performed with co-polarized horns and an aperture in an absorbing screen. The measurement step (b) is performed with the horns cross-polarized.

The other method is the lens-focused approach shown in Fig. 3.18 [2]. This is a modified version of the quasi-optical reflectometer reported by D.R. Gagnon [31]. The system is calibrated by placing an absorbing screen at the focal plane, as shown in Fig. 3.18(a). The screen has an aperture cut in it, matching the physical area A of the amplifier grid. The gain is measured in the cross-polarized setup shown in Fig. 3.18(b). In this case, the amplifier gain is simply the ratio of the power received from the grid P_r to the calibration power P_c.

The lens-focused approach has the advantage of being more straightforward, eliminating much of the path loss associated with the far-field method. On the other hand, the far-field method is much simpler to set up, as there are no lenses to focus or align. The gain of the 100-element HBT grid amplifier was measured using both approaches, with nearly identical results [2]. For simplicity, the far-field method was used to measure the gain of the 100-element pHEMT grid.

Fig. 3.19 shows the setup used to measure the gain. The transmitting and receiving antennas were AEL H-1498 wideband horns. An HP8350B sweep oscillator was used as the microwave source, and an HP8592A spectrum analyzer was the receiver. The entire grid was biased with two dc supplies—a high-current supply for the drain and a low-current one for the gate. The setup was computer-controlled, using software written by Cheh-Ming Liu, to facilitate data collection.

The assembled grid amplifier tuned for 10 GHz is shown in Fig. 3.20(a). The grid and polarizers are fabricated on Duroid boards with a relative dielectric constant of 2.2. A Duroid slab with $\varepsilon_r = 10.5$ was used as an output tuner to increase the gain. The transmission-line equivalent circuit is shown in Fig. 3.20(b). This is a half-cell model, so free space is represented by the 189-Ω resistors. The air gaps and substrates appear as transmission lines. The model representing the unit cell is the same as the one presented earlier. The polarizers are not assumed to be perfect. For a wave polarized along the direction of the metal strips, the polarizer is modeled by a low-impedance inductor. For a wave polarized orthogo-

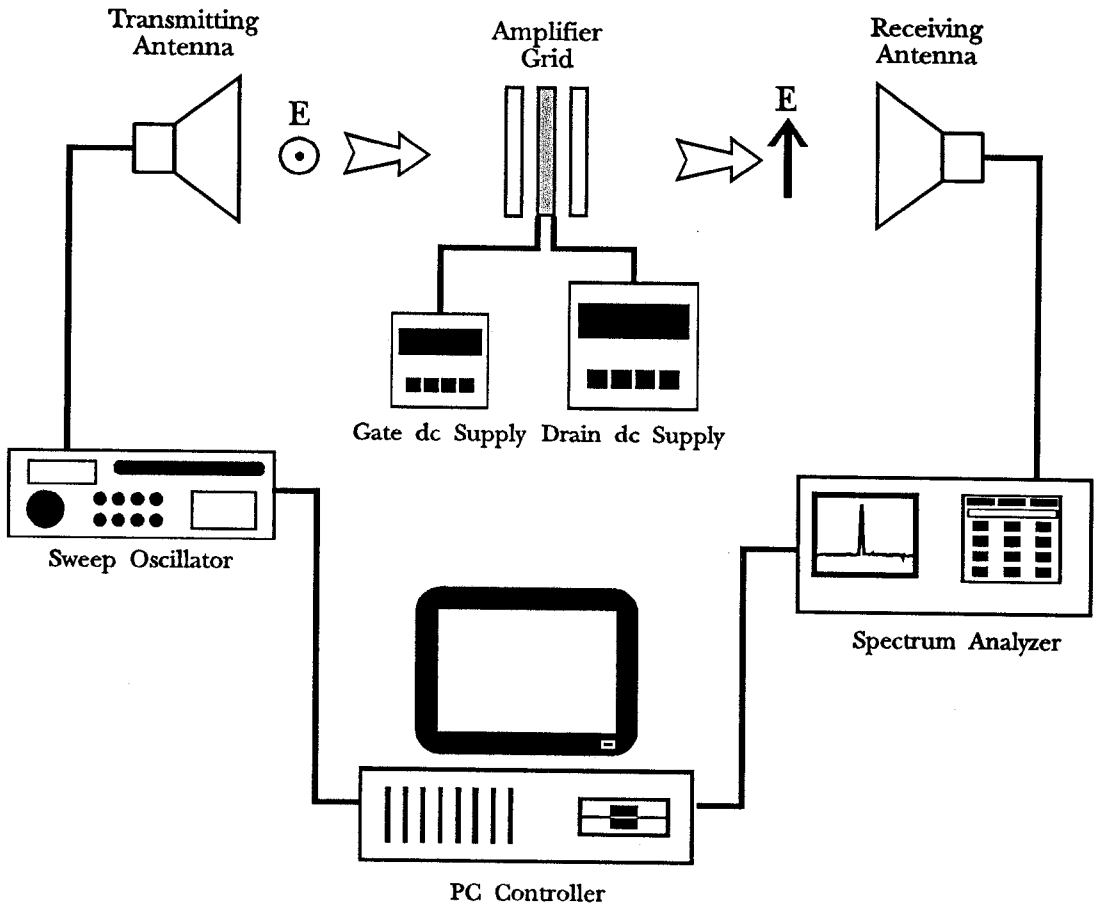

Fig. 3.19. Setup used to measure gain.

nal to the strips, the polarizer appears as a high-impedance capacitor. Numerical values for these elements were determined using the method of moment approach discussed in Appendix A.

Fig. 3.21 shows the measured small-signal gain of the amplifier. The peak gain is 10 dB at 10 GHz. The 3-dB gain bandwidth is 700 MHz, which corresponds to 7%. The modelled gain is also plotted, and it agrees well with the measured results. The grid was biased at a drain voltage of 3 V and a total drain current of 2.5 A. Without bias, the gain of the grid is below −12 dB over the entire frequency range. At peak gain, the difference between the biased and unbiased gain is over

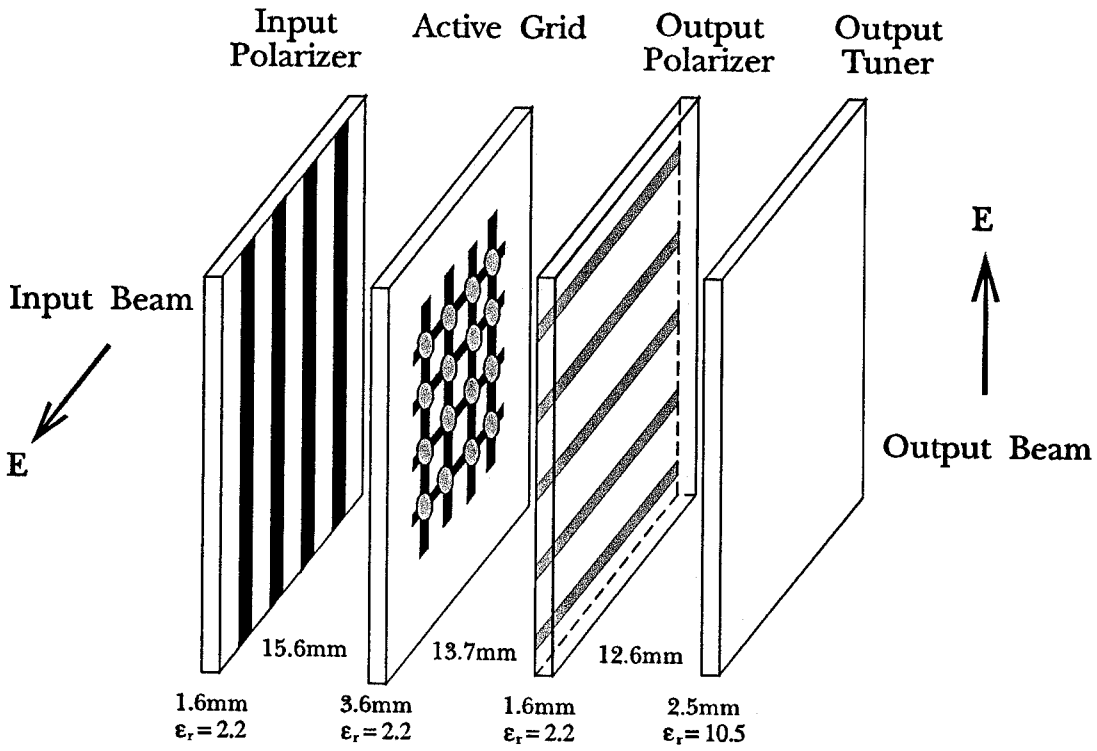

(a)

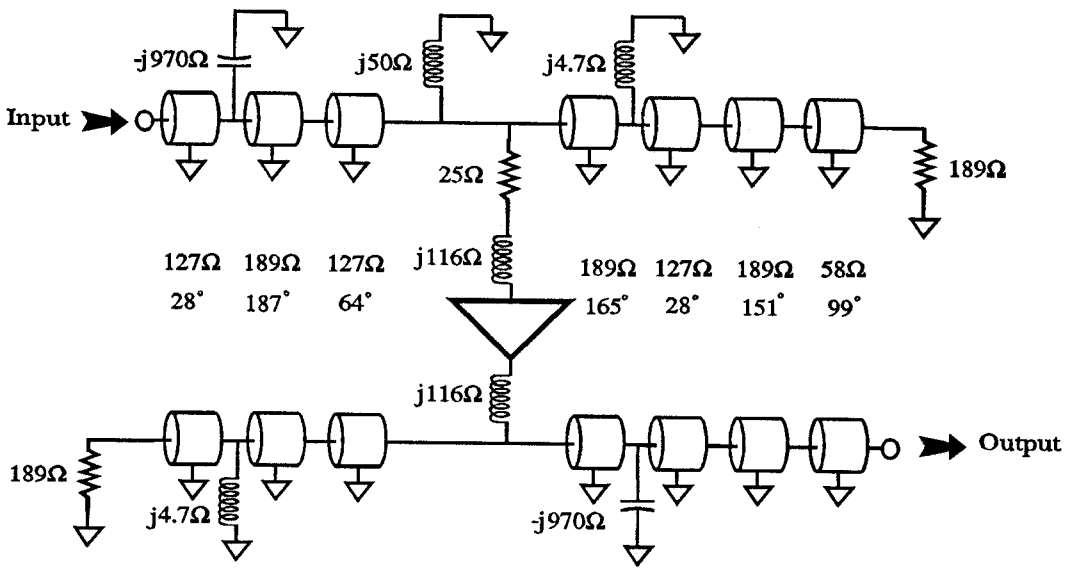

(b)

Fig. 3.20. The assembled amplifier grid (a), and the transmission-line equivalent circuit model (b) for the grid at 10 GHz.

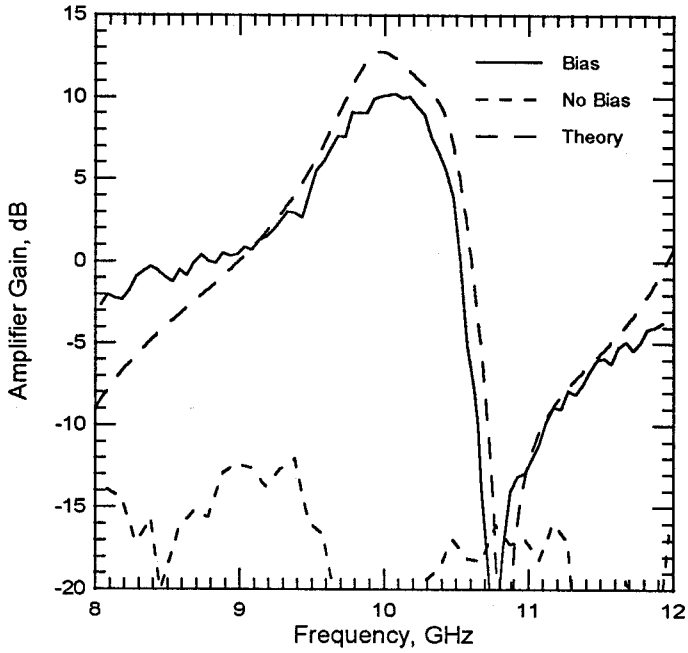

Fig. 3.21. Grid amplifier gain versus frequency. The polarizer and tuner positions are shown in Fig. 3.20(a).

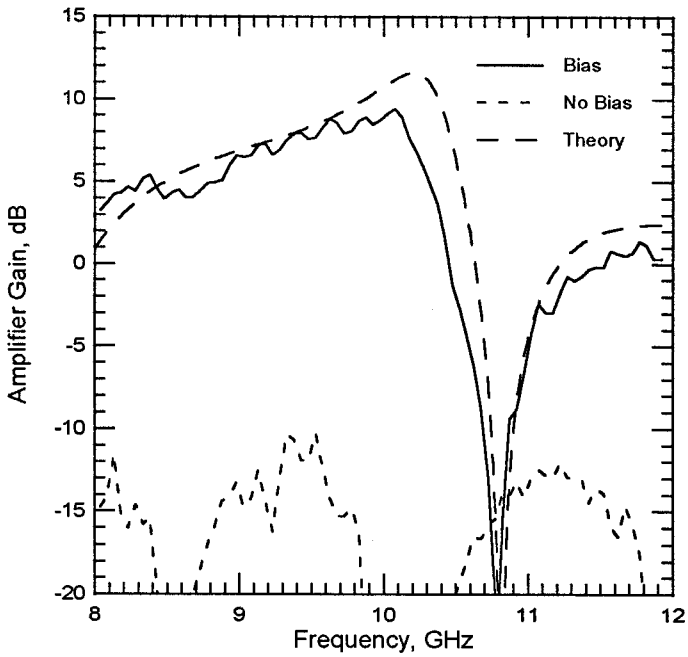

Fig. 3.22. Amplifier gain with the output tuner removed.

30 dB. An on-off ratio this high is a good indication that the grid is operating correctly. Fig. 3.22 shows the gain with the output tuner removed. The positions of the polarizers were unchanged. The peak gain is 1 dB less, but the bandwidth is increased to 1.3 GHz (13%). Again, theory and experiment compare well.

Fig. 3.23 shows the gain at 10 GHz with the output tuner removed as a function of drain bias current for three different drain bias voltages. The current was varied under constant drain voltage by changing the gate bias. The drain current was increased until the common-mode oscillations reappeared. The gain is a monotonically increasing function of drain current, levelling off at higher current levels. These results show that further increases in drain current are unlikely to significantly increase the amplifier gain.

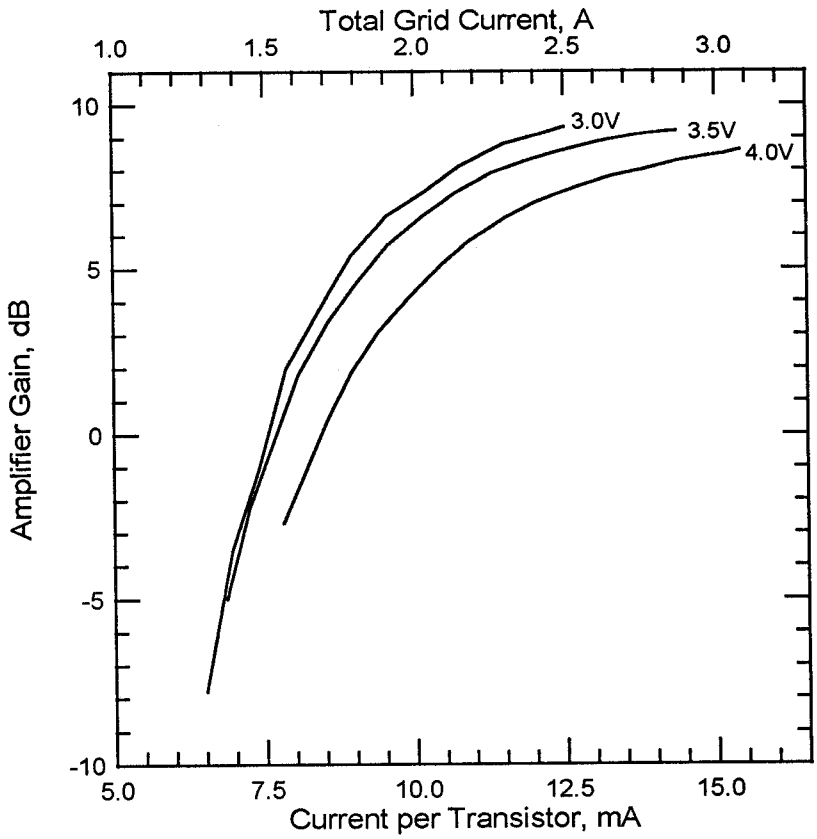

Fig. 3.23. Amplifier gain at 10 GHz as a function of drain bias current. The output tuner was not used.

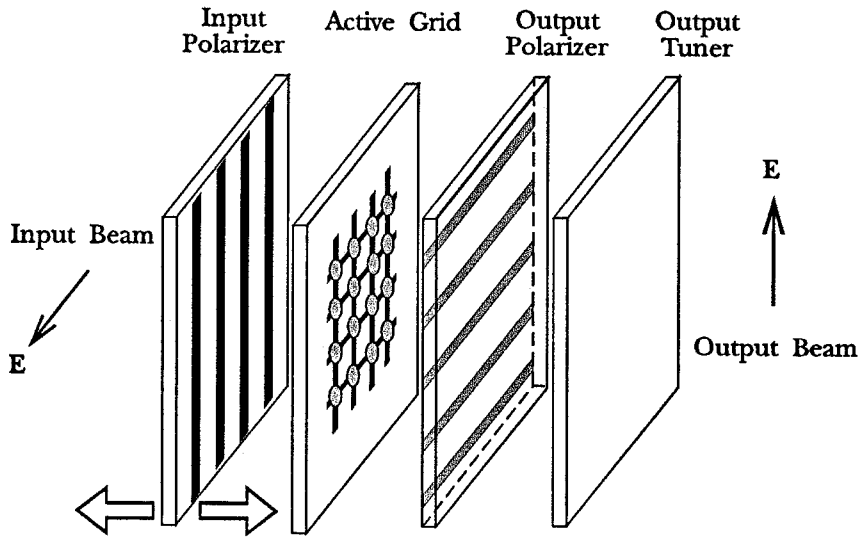

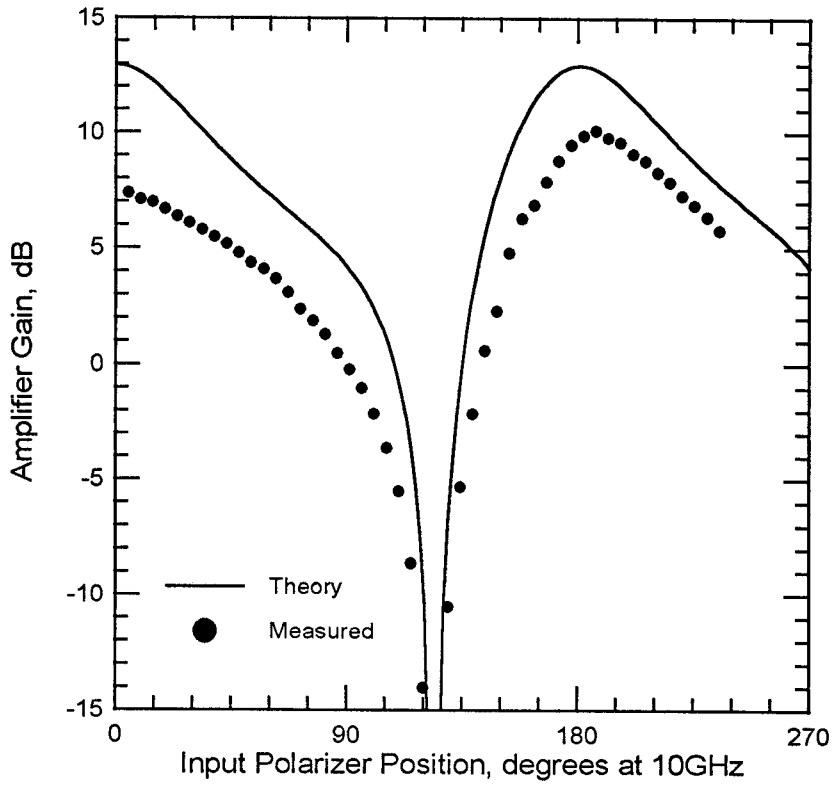

Fig. 3.24. Amplifier gain at 10 GHz as a function of input polarizer position.

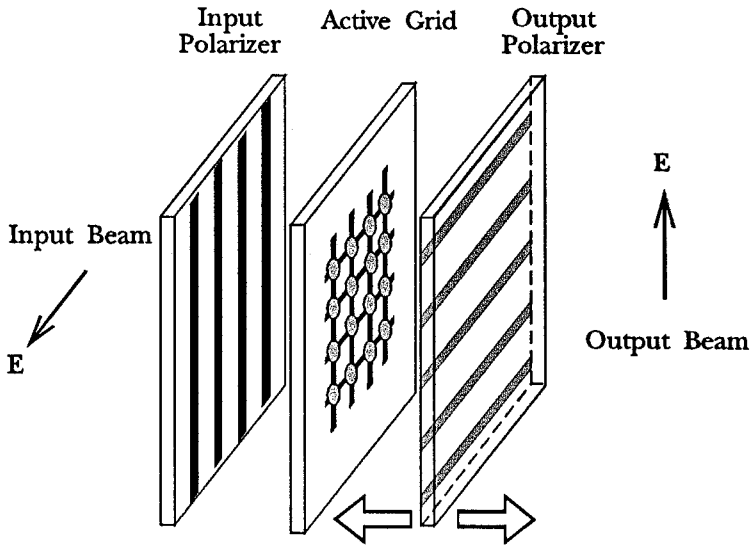

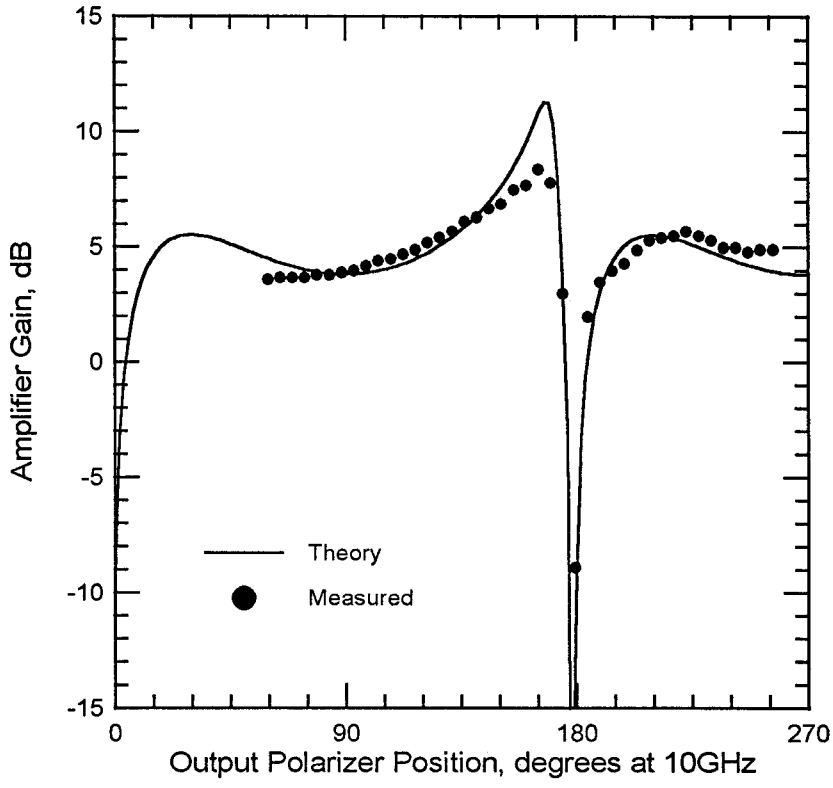

Fig. 3.25. Amplifier gain at 10 GHz as a function of output polarizer position.

To further validate the model, the gain was measured as a function of polarizer position. Fig. 3.24 shows the gain at 10 GHz as a function of input polarizer position. As seen in Fig. 2.20(b), the position of the input polarizer actually tunes the grid's output circuit. Fig. 3.25 shows the gain as a function of output polarizer position, with the output tuner removed for convenience. The tuning curves agree quite well with the theoretical predictions, which gives more credibility to the transmission-line model.

The grid can be tuned to operate at other frequencies simply by changing the positions of the external polarizers and tuners. Fig. 3.26 shows the gain with the grid tuned for 9 GHz. The peak gain is 12 dB with a 3-dB bandwidth of 1.3 GHz. This corresponds to a 15% bandwidth—the highest reported for a quasi-optical amplifier. Theory and experiment compare quite favorably, and

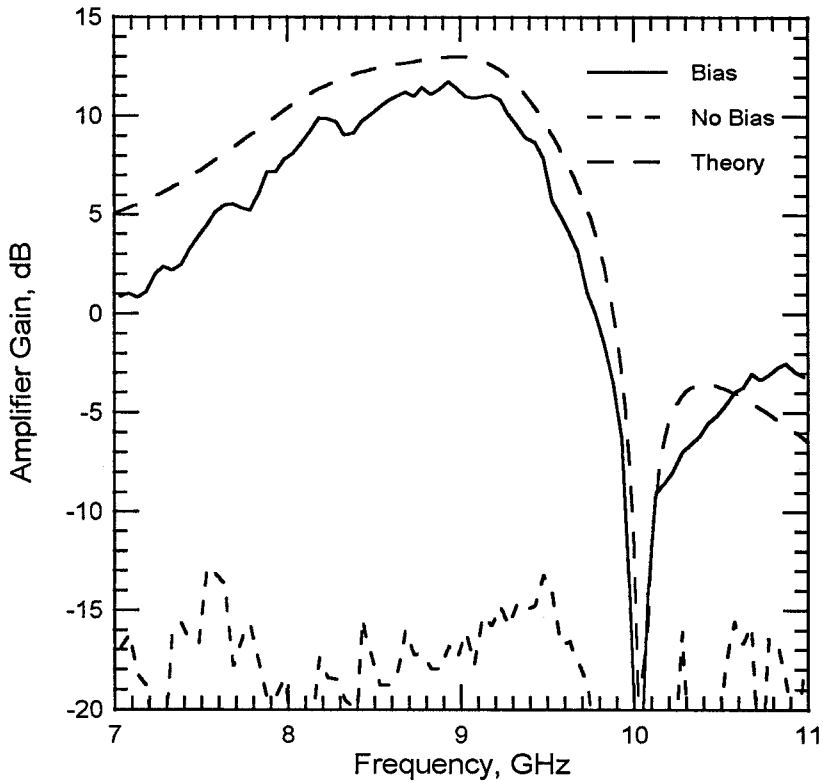

Fig. 3.26. Amplifier gain versus frequency. The grid is tuned for peak gain at 9 GHz.

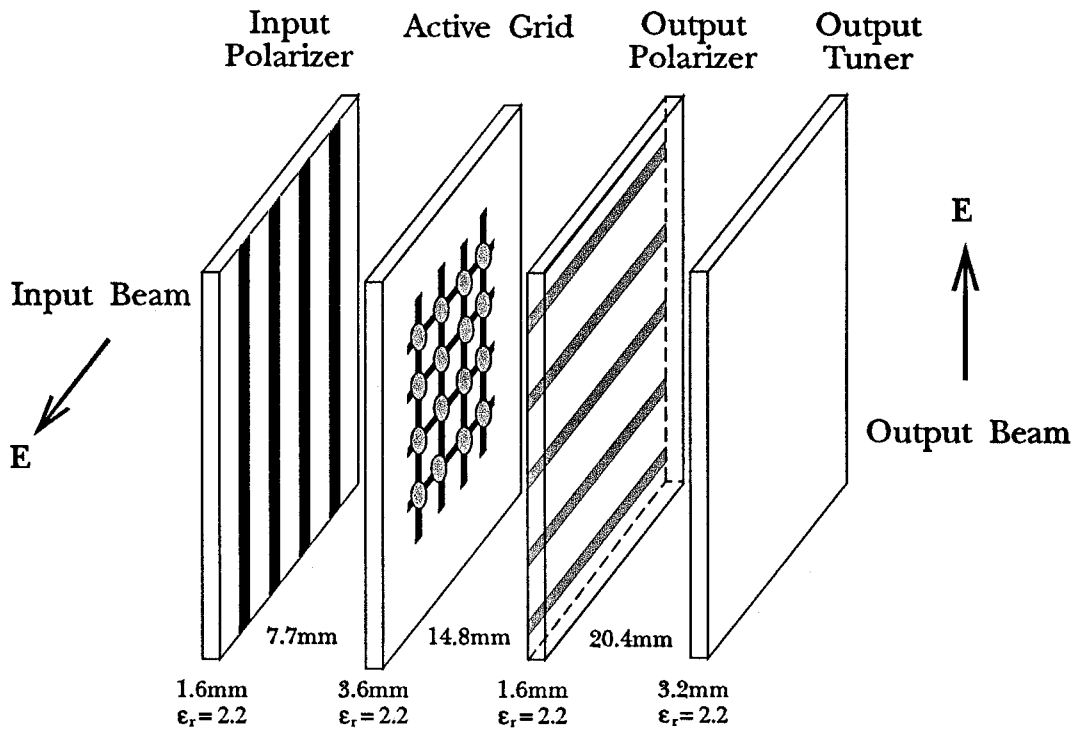

(a)

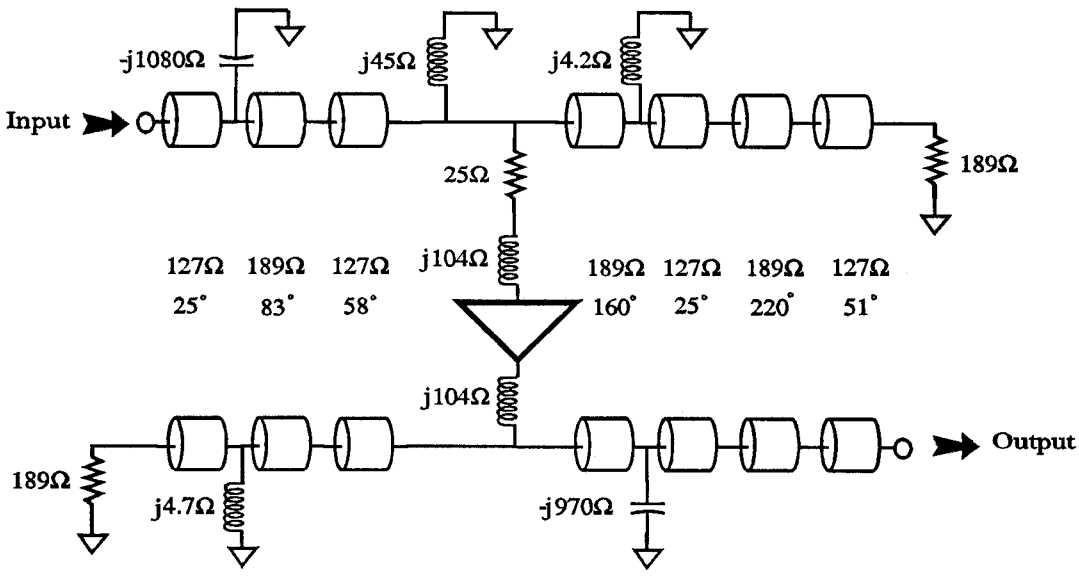

(b)

Fig. 3.27. The assembled amplifier grid (a), and the transmission-line equivalent circuit model (b) for the amplifier at 9 GHz.

the zero-bias gain is below −12 dB. The physical configuration and equivalent circuit at 9 GHz are shown in Fig. 3.27. In this case, the gain was maximized using a low-dielectric Duroid slab as an output tuner. The low-dielectric tuner has a lower quality factor Q than the high-dielectric tuner used in the 10 GHz configuration, which probably accounts for the higher percentage bandwidth.

3.5. Angular Dependence

The grid amplifier is also an antenna, and therefore has a radiation pattern. Fig. 3.28 shows the output H-plane radiation pattern at 10 GHz. This measurement was done by fixing the position of the amplifier and the input horn, and sampling the output pattern, as indicated in the figure. Both horns were in the far-field. Limitations in the measurement setup prevented measuring angles grater than 75°. Also plotted is a theoretical pattern generated assuming a uniform array of ten equally-spaced elementary dipoles. This will generate a pattern given by:

$$P(\theta) \propto \frac{\sin^2\left(\frac{10\pi a}{\lambda}\sin\theta\right)}{\sin^2\left(\frac{\pi a}{\lambda}\sin\theta\right)}, \tag{3.5}$$

where λ is the free-space wavelength and a is the element spacing. In this case, a is the unit cell size, 7.3 mm. The main beam of the measured pattern agrees very well with the theory. This indicates that the radiation pattern is diffraction-limited.

The grid is a multi-mode device, and should therefore be capable of amplifying beams at different incidence angles. The angular dependence of the gain is measured by rotating the grid between two fixed cross-polarized horns. The output tuner was not used. Fig. 3.29 shows the result at 10 GHz for input TM polarization, output TE. Fig. 3.30 shows the result for input TE polarization, output TM. For both orientations, the grid will amplify beams with incidence

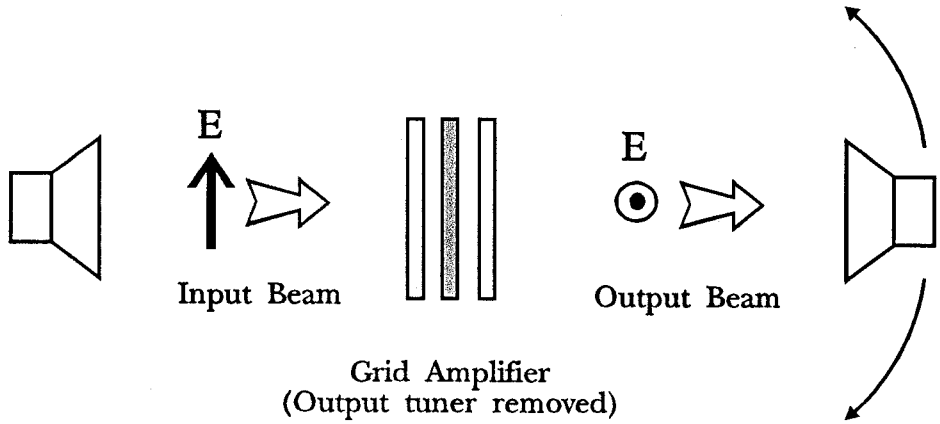

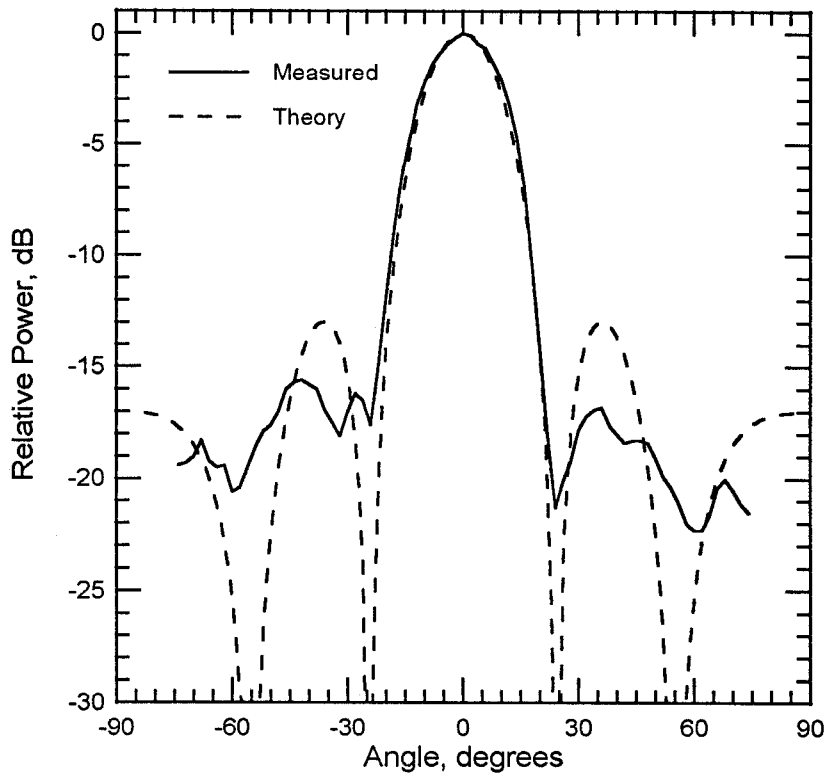

Fig. 3.28. Output H-plane radiation pattern. The input beam is normally-incident on the grid.

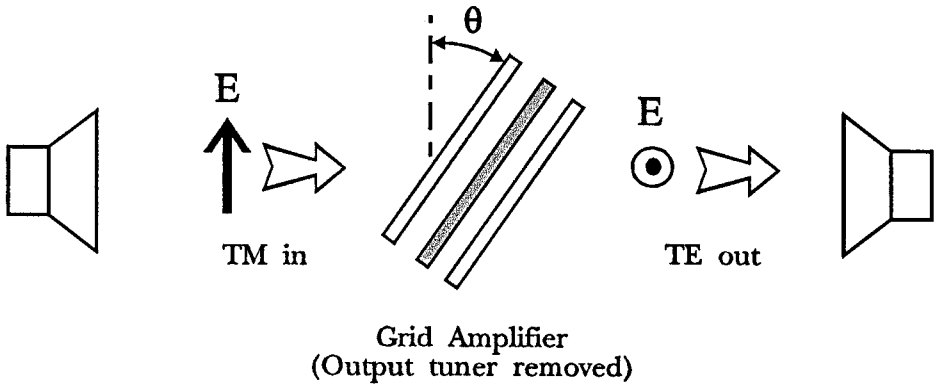

Grid Amplifier
(Output tuner removed)

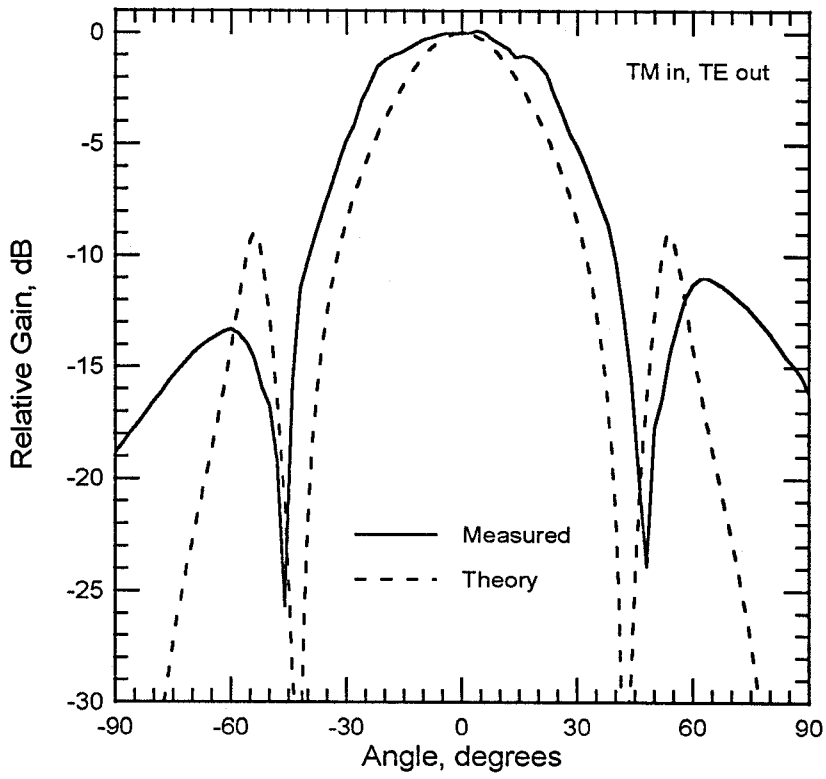

Fig. 3.29. Relative gain as a function of angle. Input TM polarization, output TE.

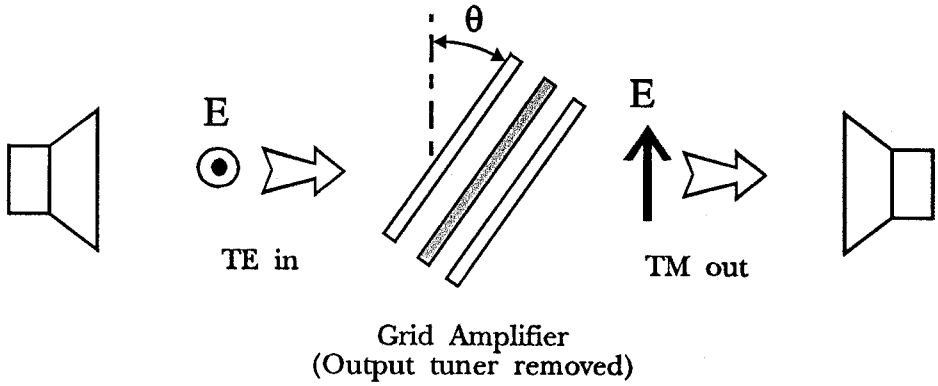

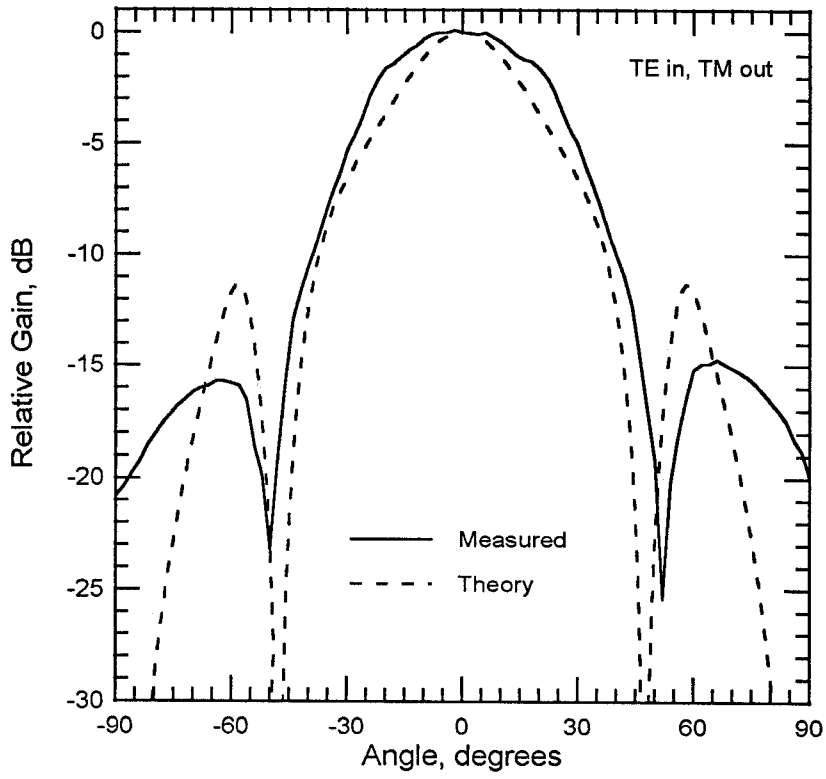

Fig. 3.30. Relative gain as a function of angle. Input TE polarization, output TM.

angles up to 25° with less than a 3-dB gain reduction. The theoretical curves were generated by scaling the lengths of each of the transmission lines in the gain equivalent circuit model by $\cos\theta_i$, where θ_i is the angle of incidence in the material, given by Snell's law. In addition, the characteristic impedance of each transmission line was multiplied by $\cos\theta_i$ for TM waves or $\sec\theta_i$ for TE waves. The pattern was then scaled by a $\cos^2\theta$ obliquity factor. The theory predicts the patterns well for small angles, but fails at larger angles where the finite size of the grid causes the simple transmission-line model to break down.

The theory for the angular dependence can be better understood by investigating a simplified example. Consider a "ideal" grid amplifier. This device is a two-dimensional active sheet, without polarizers or tuning slabs. It accepts a linearly polarized input wave, and re-radiates an orthogonally polarized output wave with unit gain. Both input and output are perfectly matched at normal incidence. A transmission-line equivalent circuit valid for oblique incidence is shown in Fig. 3.31(a). This model assumes the input polarization is TE and the output is TM. The gain of the circuit model $|S_{21}(\theta)|^2$ is given by:

$$|S_{21}(\theta)|^2 = \frac{16\cos^2\theta}{(1+\cos\theta)^4}. \tag{3.5}$$

An identical result is obtained using opposite polarizations for input and output. The gain of the idealized amplifier is obtained from this quantity by multiplying by a $\cos^2\theta$ obliquity factor. This factor accounts for the foreshortening of the grid's area for the input and output. Therefore, the gain as a function of angle for the ideal grid $T(\theta)$ is then:

$$T(\theta) = |S_{21}(\theta)|^2\cos^2\theta = \frac{16\cos^4\theta}{(1+\cos\theta)^4}. \tag{3.6}$$

The functions $T(\theta)$, $|S_{21}(\theta)|^2$, and $\cos^2\theta$ are plotted in Fig. 3.31(b). Since $|S_{21}(\theta)|^2$ is so flat at near-normal incidence angles, $T(\theta)$ is almost identical to the $\cos^2(\theta)$ obliquity factor. This simple example is the basis for the theoretical gain versus angle patterns shown earlier.

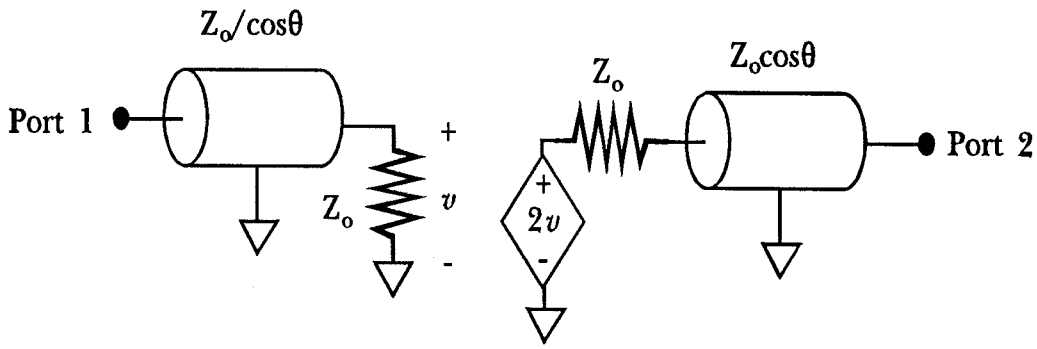

(a)

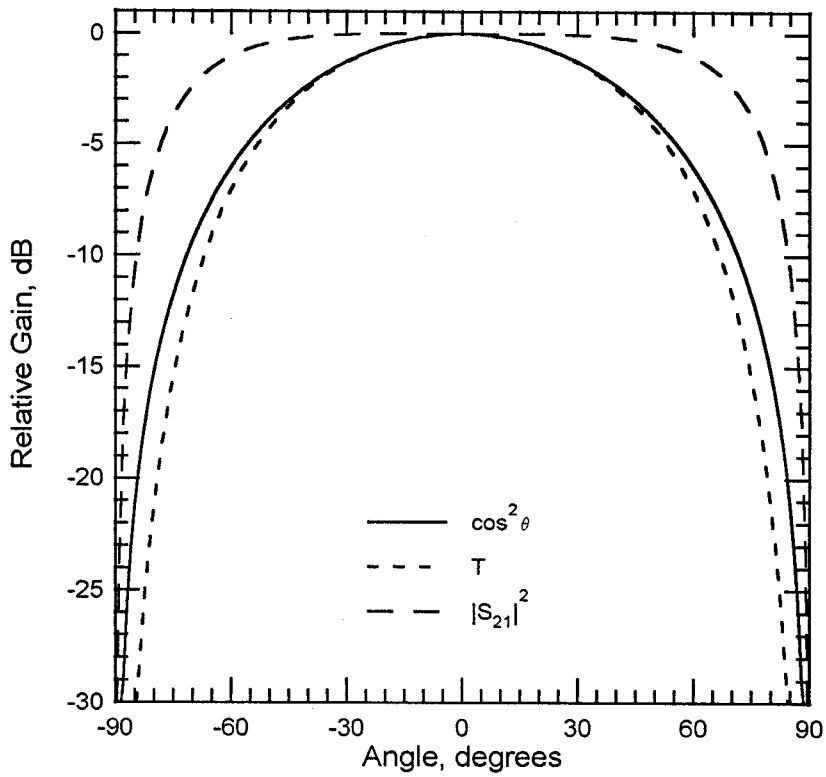

(b)

Fig. 3.31. Transmission-line model for the ideal unity-gain amplifier (a). Plot of several quantities related to the gain of the ideal amplifier as a function of incidence angle (b).

The nulls in the patters of Figs. 3.29 and 3.30 near ±50° are caused by the input polarizer being farther than a half wavelength from the active surface of the grid. The nulls disappear when the polarizer is moved closer to the grid by a half wavelength. This is shown in Fig. 3.32. Theoretically, moving a polarizer a half wavelength should not affect the gain at that frequency. The gain with the closer polarizer spacing, however, was 3 dB less. This can also be seen in the tuning curve, Fig. 3.24. This may be evidence of evanescent-wave coupling, a phenomena that occurs in closely spaced quasi-optical systems [32]. Nevertheless, in this configuration, the grid will amplify beams with incident angles up to 30° with less than a 3-dB gain reduction. The patterns approach the $\cos^2\theta$ obliquity limit.

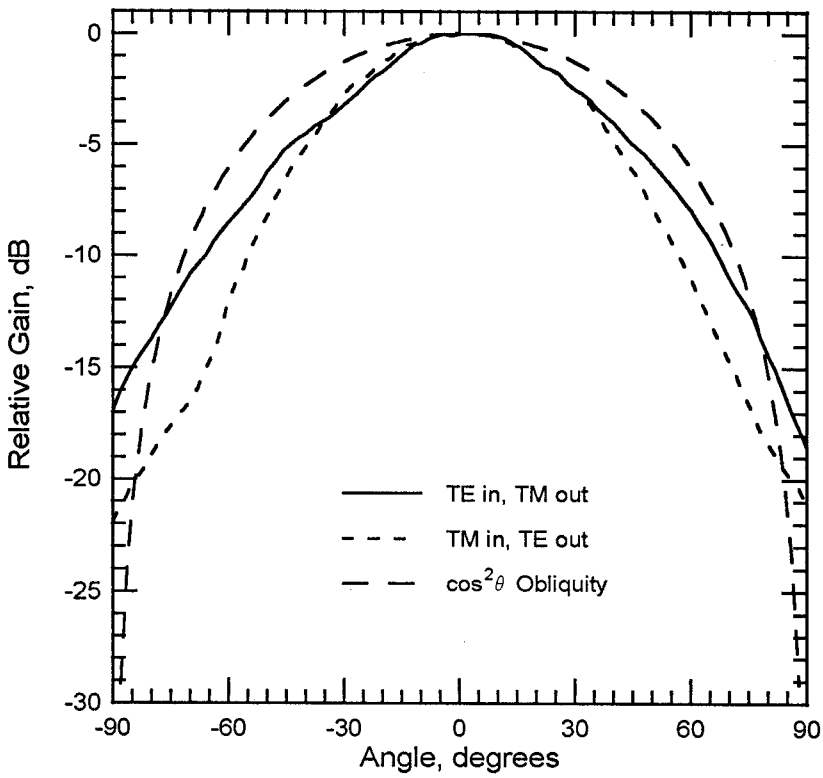

Fig. 3.32. Relative gain as a function of angle with the input polarizer moved closer by one-half wavelength. The peak gain is reduced by 3 dB.

3.6. Noise Figure

Because the noise from the individual elements are uncorreleated, the noise figure of a grid amplifier should be no worse than that of a single device. The noise figure was measured using the far-field approach detailed in [2]. Fig. 3.33 shows the measurement setup. An HP8970A noise figure meter was used to characterize the grid. The HP8350B sweep oscillator and Watkins-Johnson WJM17C mixer were used to upconvert the frequency range of the noise figure meter to X-band. To increase the accuracy of the measurement, a Noise Com NC3206 noise source with a high excess noise ratio (36 dB) was used. In addition, a low-noise preamplifier was added to further increase the sensitivity. This preamplifier was

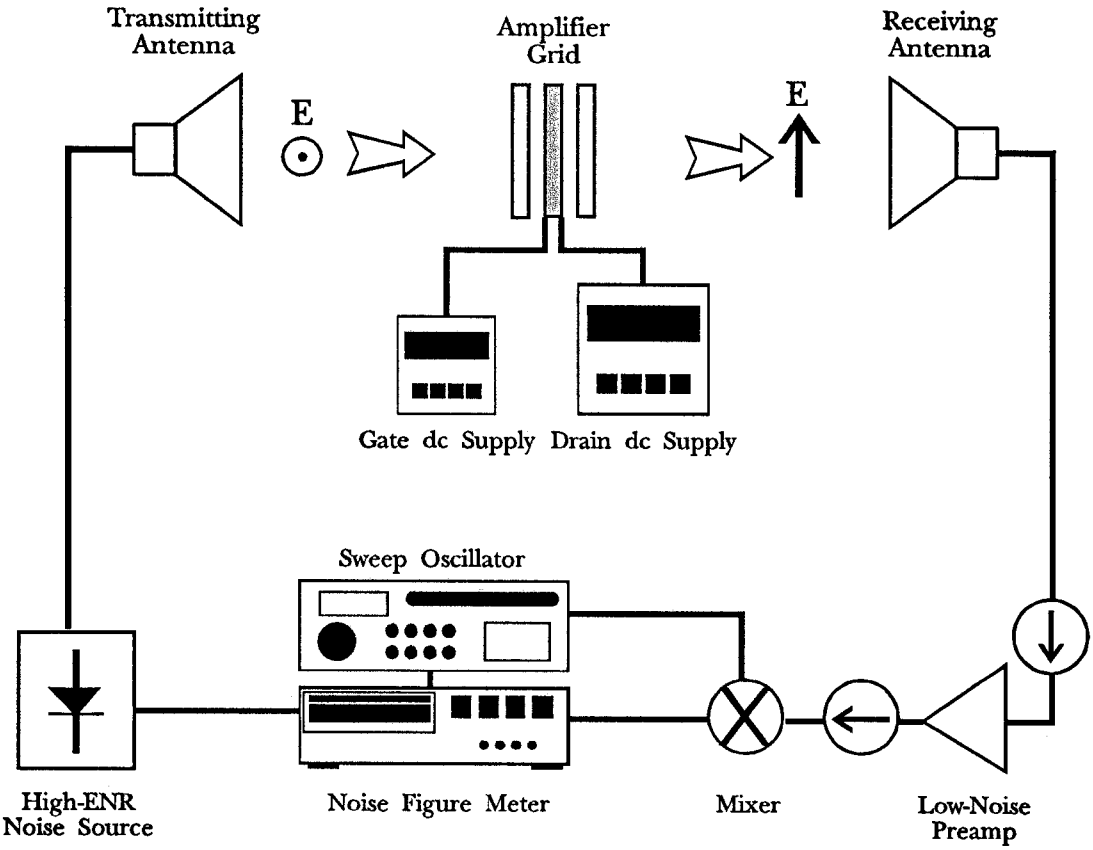

Fig. 3.33. The quasi-optical noise figure measurement setup.

made using a Fujitsu FHX35LG HEMT in a microstrip circuit. The gain of the preamplifier was 12 dB at 10 GHz, with a 2.5-dB noise figure.

Fig. 3.34 shows the measured result. The grid was tuned for 10 GHz, and the output tuner was included. The minimum noise figure is 3 dB for the 3 V bias. This is a 4-dB improvement over the HBT grid [2]. The predicted minimum noise figure F_{min} is given by Fukui's equation [33]:

$$F_{min} = 1 + 2\pi f K C_{gs} \sqrt{\frac{R_s + R_g + R_{st}}{g_m}}, \tag{3.7}$$

where the device source resistance R_s is 4.7 Ω, the device gate resistance R_g is 2.4 Ω, the device transconductance g_m is 98 mS, the device gate-source capacitance C_{gs} is 76 fF, and the material parameter K is assumed to be 5. With the gate stabilization resistance R_{st} included, the predicted F_{min} is 1.6 dB at 10 GHz.

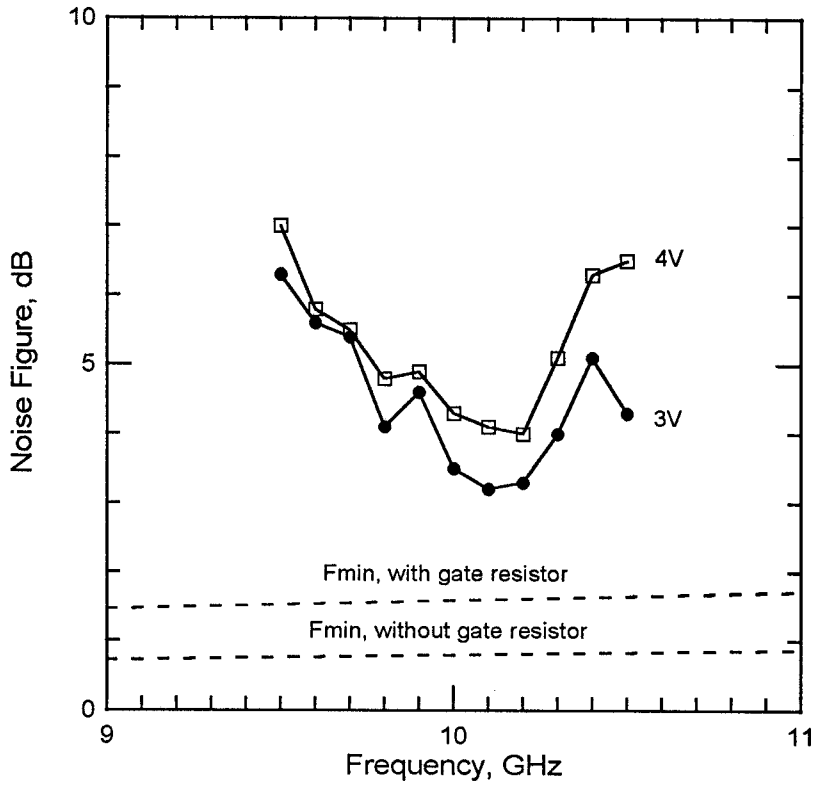

Fig. 3.34. Measured noise figure at two different bias points.

The gate stabilizing resistor R_{st} degrades F_{min} by 0.8 dB. The measured noise figure of 3 dB is only about 1.4 dB higher than the predicted minimum noise figure. It should be noted that no attempt was made to noise match the amplifier. This result shows that the noise figure of the grid amplifier is not considerably worse than that of a single pHEMT, as expected.

The gain of the amplifier can be determined from the noise figure measurement. Fig. 3.35 compares the amplifier gain measured from the noise figure measurement to the gain measured in the conventional way, as plotted in Fig. 3.21. The close agreement adds credibility to the noise measurement. In addition, one can extract the background temperature of the area surrounding the experimental setup from the noise measurement. Unlike the result in [2], the background

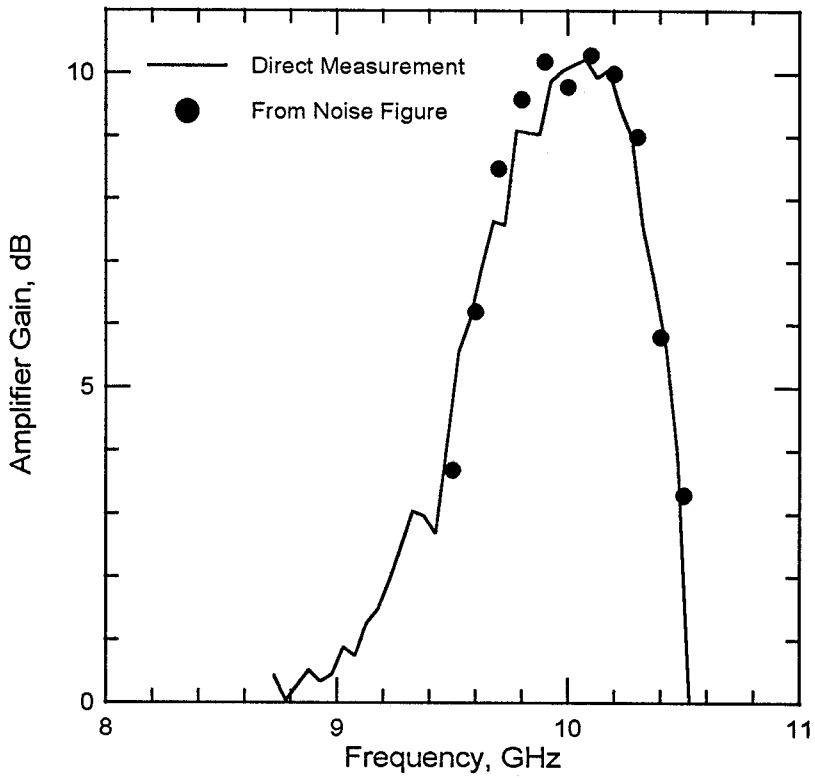

Fig. 3.35. Comparison of the amplifier gain extracted from the noise measurement to the gain in Fig. 3.21.

temperature did not vary strongly with frequency. The average temperature was 298K, with a standard deviation of only 2.5K, further validating the noise measurement.

3.7. Power

The grid's power saturation was also measured in the far-field [2]. The setup is shown in Fig. 3.36. A high-power Hughes 1277H02 Travelling-Wave Tube Amplifier (TWTA) was used as the source. An HP435B power meter and

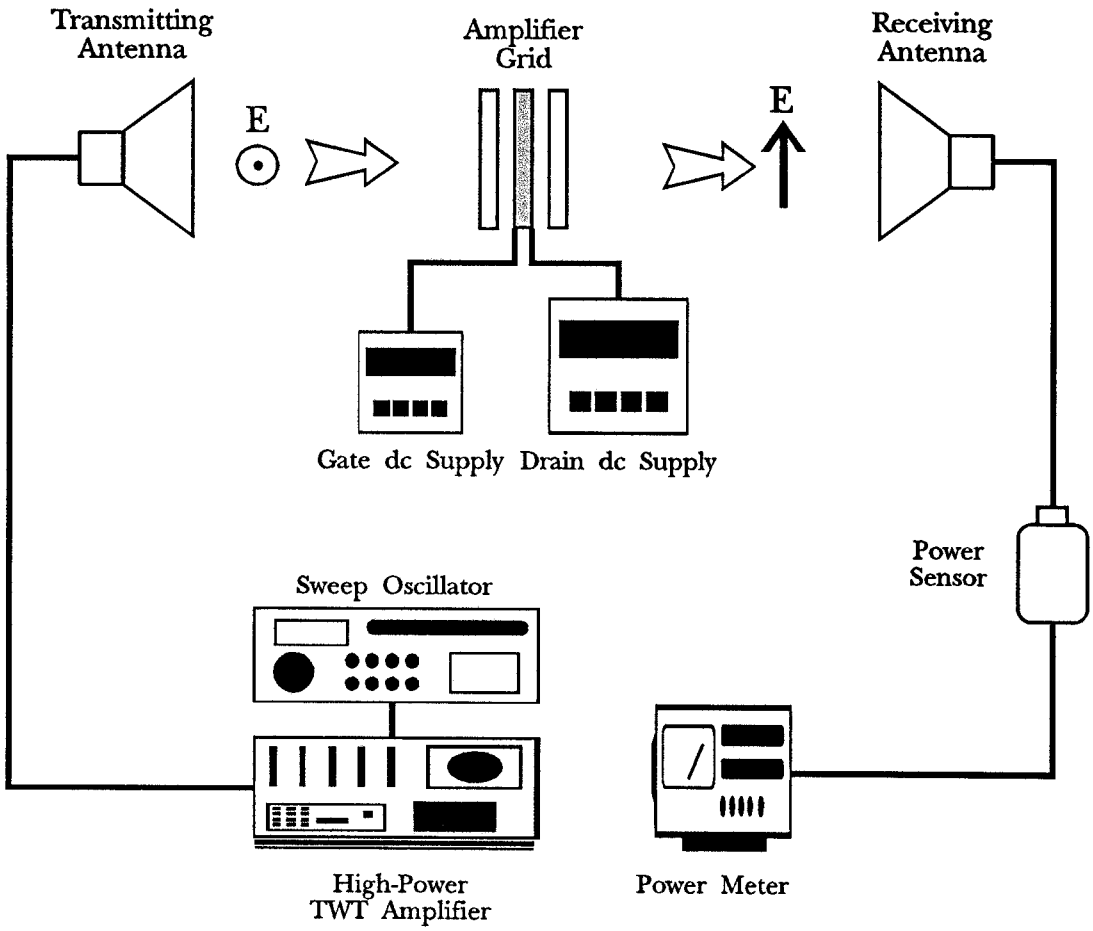

Fig. 3.36. The quasi-optical power saturation measurement setup.

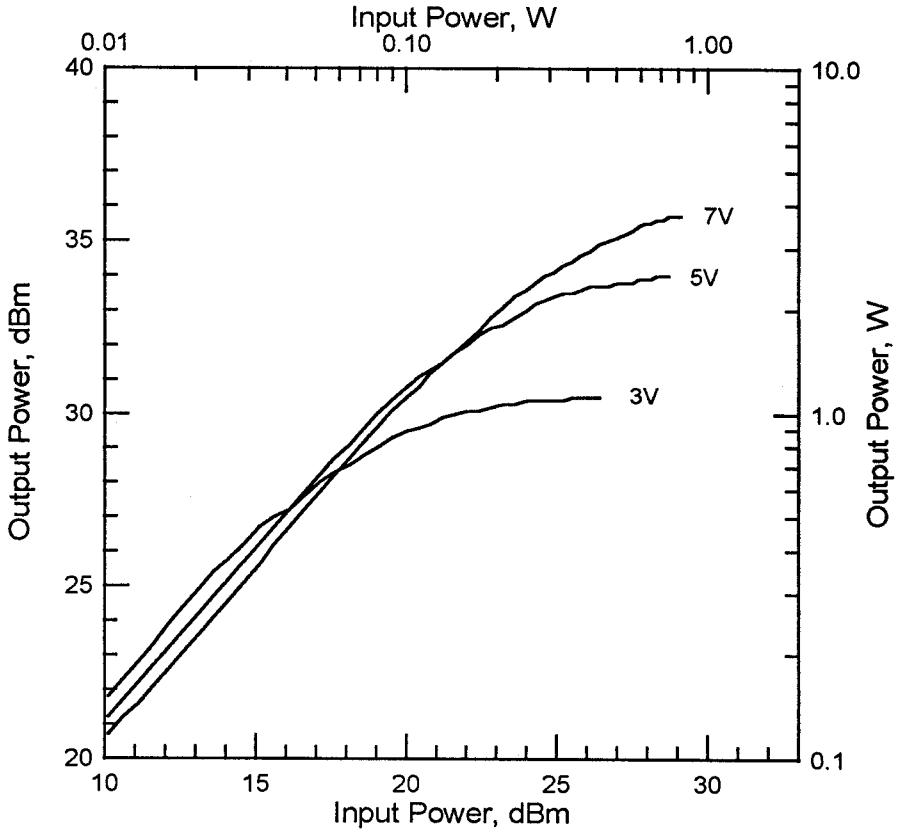

Fig. 3.37. Output power at 9 GHz for three bias points.

an HP8481A sensor were used to detect the output. The grid was tuned to 9 GHz to match the TWTA's output frequency. Fig. 3.37 shows the result. The highest output power is 3.7 W at the 7 V bias. This is an 8-dB improvement over the HBT grid amplifier [2], and is the highest recorded output power for a quasi-optical amplifier to date. Each pHEMT is providing about 18.5 mW, which corresponds to 185 mW per millimeter of gate length. Although output power densities higher than 800 mW/mm have been reported for X-band pHEMT's [19], this result is quite good for these particular devices. The total dc power supplied to the grid was 24.5 W. To avoid overheating, the grid was only biased for several seconds at a time.

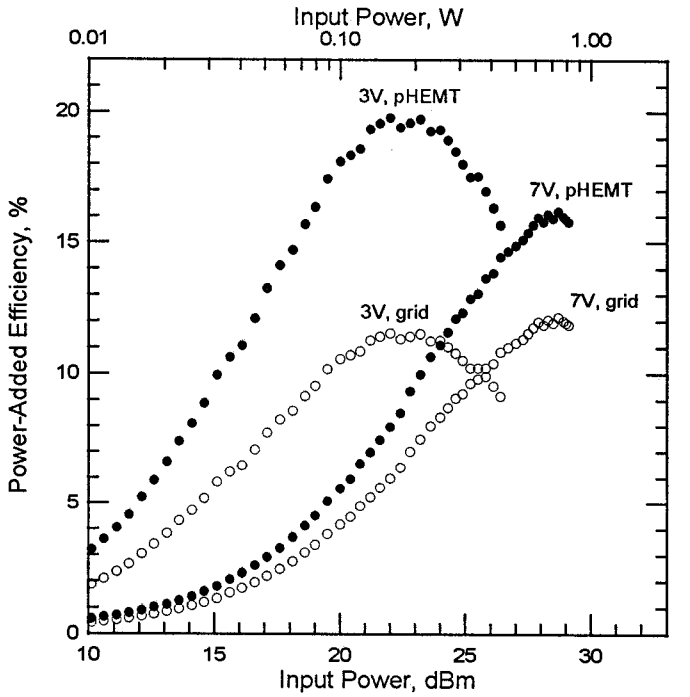

(a)

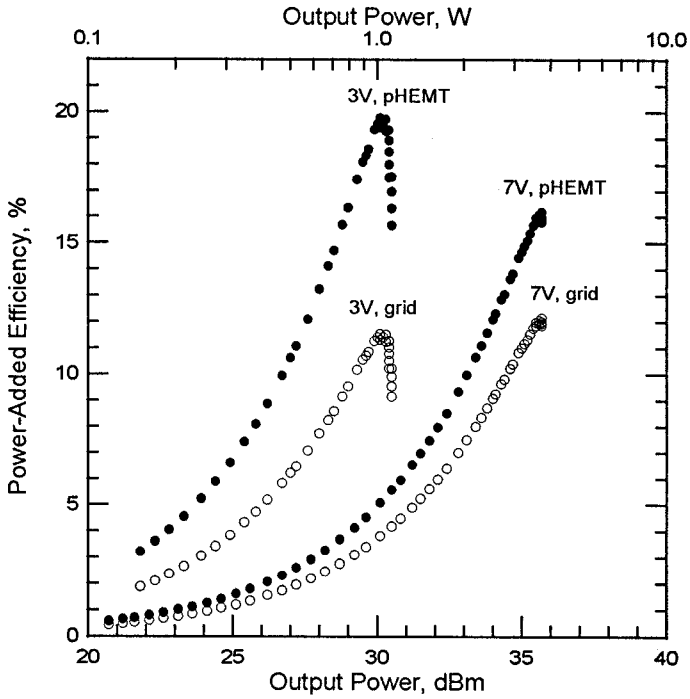

Fig. 3.38. Power-added efficiency at 9 GHz versus input power (a) and output power (b). The solid circles are the efficiency for the pHEMT alone, discounting the dc power dissipated in the source resistors.

Fig. 3.38 shows the power-added efficiency for the 3 V and 7 V bias. Efficiency is plotted as a function of input power in Fig. 3.38(a) and output power in Fig. 3.38(b). The peak efficiency is 12%. This is more than a factor of two higher than the HBT grid [2]. The efficiency for the pHEMT alone can be calculated by discounting the dc power lost in the 100-Ω source resistors. The peak device efficiency is 20% for the 3 V bias at an output power of 1 W. The amplifier is operating in the class-A mode, which has a maximum efficiency of 50%. It may be possible to achieve higher efficiencies by operating the grid in another mode. Power-added efficiencies over 70% have been reported in X-band pHEMT amplifiers [17]. Furthermore, highly efficient class-E switched-mode MESFET amplifiers have demonstrated power-added efficiencies of over 70% [34]. A quasi-optical amplifier employing one of these modes would be an efficient way to generate substantial power at microwave or millimeter-wave frequencies.

Fig. 3.39 shows the gain of the amplifier as a function of power for the two bias points. Gain is plotted as a function of input power in Fig. 3.39(a) and output power in Fig. 3.39(b). A figure of merit for amplifiers that is often quoted is the 1-dB gain compression point. This is the output power at which the gain is 1 dB lower than the small-signal gain. Judging from Fig. 3.39(b), the amplifier's 1-dB gain compression point is 680 mW for the 3 V bias, and 2.3 W for the 7 V bias.

The dynamic range of a amplifier is determined on the high end by the device's power-handling capability. The low end is determined by the amplifier's noise performance. These results have shown that the dynamic range can be greatly increased through quasi-optical power combining.

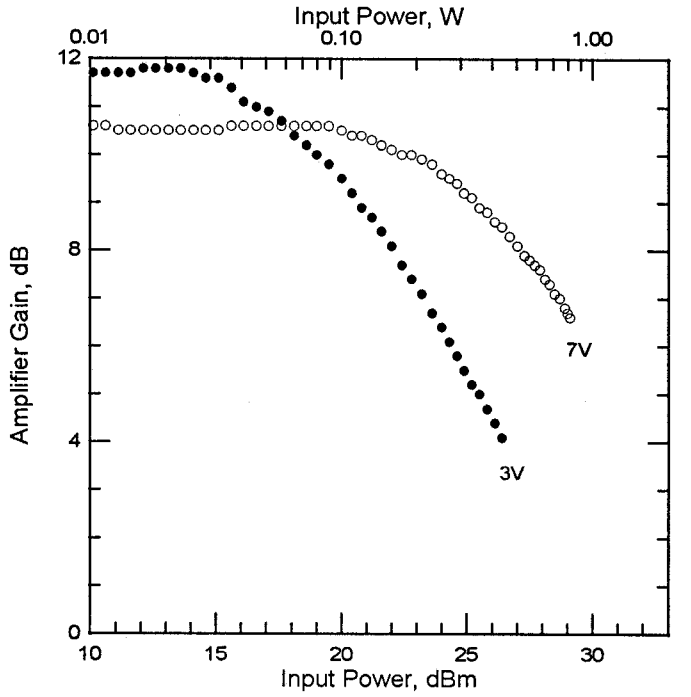

(a)

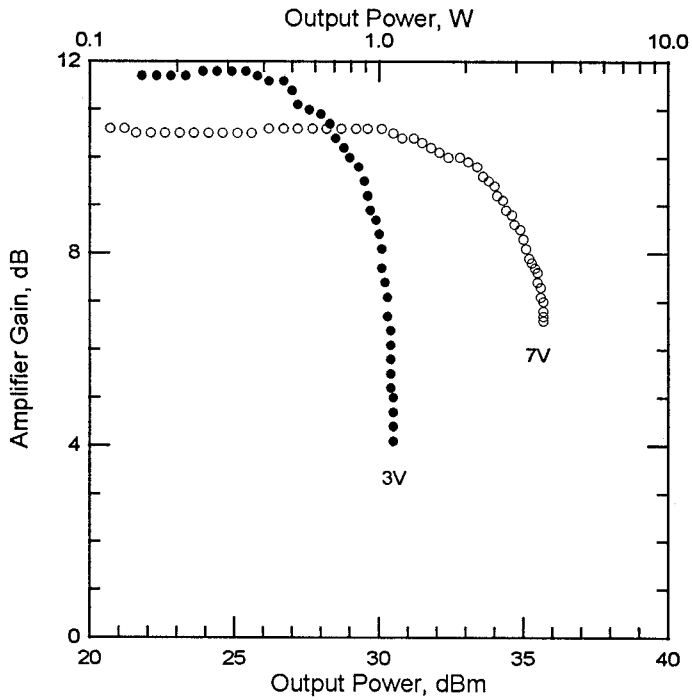

Fig. 3.39. Gain at 9 GHz versus input power (a) and output power (b).

References

[1] M. Kim, J.J. Rosenberg, R.P. Smith, R.M. Weikle, J.B. Hacker, M.P. De Lisio, D.B. Rutledge, "A Grid Amplifier," *IEEE Microwave Guided Wave Lett.*, vol. 1, pp. 322–324, Nov. 1991.

[2] M. Kim, E.A. Sovero, J.B. Hacker, M.P. De Lisio, J.-C. Chiao, S.-J. Li, D.R. Gagnon, J.J. Rosenberg, D.B. Rutledge, "A 100-Element HBT Grid Amplifier," *IEEE Trans. Microwave Theory Tech.*, vol. 41, pp. 1762–1771, Oct. 1993.

[3] C.-Y. Chi, G.M. Rebeiz, "A Quasi-Optical Amplifier," *IEEE Microwave Guided Wave Lett.*, vol. 3, pp. 164–166, June 1993.

[4] T.P. Budka, M.W. Trippe, S. Weinreb, G.M. Rebeiz, "A 75 GHz to 110 GHz Quasi-Optical Amplifier," *IEEE Trans. Microwave Theory Tech.*, vol. 42, pp. 899–901, May 1994.

[5] N. Kolias, R.C. Compton, "A Microstrip-Based Unit Cell for Quasi-Optical Amplifier Arrays," *IEEE Microwave Guided Wave Lett.*, vol. 3, pp. 330–332, Sept. 1993.

[6] T. Mader, J. Schoenberg, L. Harmon, Z.B. Popović, "Planar MESFET Transmission Wave Amplifier," *Electronics Lett.*, vol. 29, pp. 1699–1701, Sept. 1993.

[7] H.S. Tsai, R.A. York, "Polarisation-Rotating Quasioptical Reflection Amplifier Cell," *Electronics Lett.*, vol 29, pp. 2125–2127, Nov. 1993.

[8] N. Sheth, T. Ivanov, A. Balasubramaniyan, A. Mortazawi, "A Nine HEMT Spatial Amplifier," *1994 IEEE MTT-S Int. Microwave Symp. Dig.*, pp. 1239–1242, 1994.

[9] J.S.H. Schoenberg, S.C. Bundy, Z.B. Popović, "Two-Level Power Combining Using a Lens Amplifier," *IEEE Trans. Microwave Theory Tech.*, vol. 42, pp. 2480–2485, Dec. 1994.

[10] T. Ivanov, A. Mortazawi, "Two Stage Double Layer Microstrip Spatial Amplifiers," *1995 IEEE MTT-S Int. Microwave Symp. Dig.*, pp. 589–592, 1995.

[11] J. Schoenberg, T. Mader, B. Shaw, Z.B. Popović, "Quasi-Optical Antenna Array Amplifiers," *1995 IEEE MTT-S Int. Microwave Symp. Dig.*, pp. 605–608, 1995.

[12] J.S.H. Schoenberg, T.B. Mader, J.W. Dixon, B.L. Shaw, Z.B. Popović, "Quasi-Optical Antenna Array Amplifiers," submitted to *IEEE Trans. Microwave Theory Tech.*, March 1995.

[13] T. Ivanov, A. Balasubramaniyan, A. Mortazawi, "One- and Two-Stage Spatial Amplifiers," *IEEE Trans. Microwave Theory Tech.*, vol. 43, pp. 2138–2143, Sept. 1995.

[14] H.S. Tsai, M.J.W. Rodwell, R.A. York, "Planar Amplifier Array With Improved Bandwidth Using Folded-Slots," *IEEE Microwave Guided Wave Lett.*, vol. 4, pp. 112–114, April 1994.

[15] H.S. Tsai, R.A. York, "Quasi-Optical Amplifier Array using Direct Integration of MMICs and 50 Ω Multi-Slot Antennas," *1995 IEEE MTT-S Int. Microwave Symp. Dig.*, pp. 593–596, 1995.

[16] J. Hubert, J. Schoenberg, Z.B. Popović, "High-Power Hybrid Quasi-Optical Ka-Band Amplifier Design," *1995 IEEE MTT-S Int. Microwave Symp. Dig.*, pp. 585–588, 1995.

[17] D.-W. Tu, S.W. Duncan, A. Eskandarian, B. Golja, B.C. Kane, S.P. Svenson, S. Weinreb, N.E. Byer, "High Gain Monolithic W-Band Low Noise Amplifiers Based on Pseudomorphic High Electron Mobility Transistors," *IEEE Trans. Microwave Theory Tech.*, vol. 42, pp. 2590–2597, Dec. 1994.

[18] P.M. Smith, D.W. Ferguson, W.F. Kopp, P.C. Chao, W. Hu, P. Ho, J.M. Ballingall, "A High Power, High Efficiency Millimeter Wave Pseudomorphic HEMT," *1991 IEEE MTT-S Int. Microwave Symp. Dig.*, pp. 717–720, 1991.

[19] S. Shanfield, A. Platzker, L. Aucoin, T. Kazior, B.I. Patel, A. Bertand, W. Hoke, P. Lyman, "One-Watt, Very High Efficiency 10 and 18 GHz Pseudomorphic HEMT's Fabricated by Dry First Recess Etching," *1992 IEEE MTT-S Int. Microwave Symp. Dig.*, pp. 639–641, 1992.

[20] S.T. Fu, L.F. Lester, T. Rogers, "Ku-Band High Power High Efficiency Pseudomorphic HEMT," *1994 IEEE MTT-S Int. Microwave Symp. Dig.*, pp. 793–796, 1994.

[21] D.B. Rutledge, A. Moussessian, M.P. DeLisio, C.-M. Liu, J.J. Rosenberg, "Modelling of Transistor Grid Amplifiers," *1994 IEEE MTT-S Int. Microwave Symp.*, Workshop Notes, WFFA: Circuit Level Design and Modelling of Quasi-Optical Circuits and Systems, pp. C.1–C.16, 1994.

[22] M. Kim, "Grid Amplifiers," Ph.D. Thesis, California Institute of Technology. Pasadena, CA, 1993.

[23] M.P. DeLisio, S.W. Duncan, D.-W. Tu, C.-M. Liu, A. Moussessian, J.J. Rosenberg, D.B. Rutledge, "Modelling and Performance of a 100-Element pHEMT Grid Amplifier," submitted to *IEEE Trans. Microwave Theory Tech.*, April 1995.

[24] C.-M. Liu, E.A. Sovero, M.P. DeLisio, A. Moussessian, J.J. Rosenberg, D.B. Rutledge, "Gain and Stability Models for HBT Grid Amplifiers," *1995 IEEE AP-S Int. Symp. Dig.*, pp. 1292–1295, 1995.

[25] C.-M. Liu, E.A. Sovero, W.J. Ho, J.A. Higgins, M.P. DeLisio, D.B. Rutledge, "Monolithic 40-GHz 670-mW HBT Grid Amplifier," submitted to *1996 IEEE MTT-S Int. Microwave Symp.*, Oct. 1995.

[26] M.P. DeLisio, S.W. Duncan, D.-W. Tu, S. Weinreb, C.-M. Liu, D.B. Rutledge, "A 44-60 GHz Monolithic pHEMT Grid Amplifier," submitted to *1996 IEEE MTT-S Int. Microwave Symp.*, Oct. 1995.

[27] "HP 85180A High Frequency Structure Simulator," Hewlett-Packard, Networks Measurements Division, Santa Rosa, CA.

[28] R.S. Carson, *High-Frequency Amplifiers*, second ed., John Wiley & Sons, Inc., New York, 1982, pp. 228–268.

[29] G. Gonzalez, *Microwave Transistor Amplifiers*, Prentice-Hall, Inc., Englewood Cliffs, NJ, 1984, pp. 91–138.

[30] R.D. Martinez, R.C. Compton, "A General Approach for the S-Parameter Design of Oscillators with 1 and 2-Port Active Devices," *IEEE Trans. Microwave Theory Tech.*, vol. 40, pp. 596–574, March 1992.

[31] D.R. Gagnon, "Highly Sensitive Measurements With a Lens-Focused Reflectometer," *IEEE Trans. Microwave Theory Tech.*, vol. 39, pp. 2237–2240, Dec. 1991.

[32] J. Bae, J.-C. Chiao, K. Mizuno, D.B. Rutledge, "Metal Mesh Couplers Using Evanescent Waves at Millimeter and Submillimeter Wavelengths," *1995 IEEE MTT-S Int. Microwave Symp. Dig.*, pp. 597–600, 1995.

[33] H. Fukui, "Optimal Noise Figure of Microwave GaAs MESFET's" *IEEE Trans. Electron Devices*, vol. 26, pp. 1032–1037, July 1979.

[34] T.B. Mader, A.B. Popović, "The Transmission-Line High-Efficiency Class-E Amplifier," *IEEE Microwave Guided Wave Lett.*, vol. 5, pp. 290–292, Sept. 1995.

Chapter 4

Monolithic U-Band pHEMT Amplifier Grid

In this chapter, a 36-element monolithic U-band amplifier grid is presented. The active devices are pHEMT differential-pairs, monolithically fabricated by Lockheed Martin Laboratories. A first iteration design produced limited gain. A second iteration was fabricated, with the grids redesigned to reduce parasitic source inductance. In addition, the second fabrication produced pHEMT's with markedly improved performance characteristics. These second-iteration grids were successful, producing 6.5 dB gain at 44 GHz. Simply by changing the positions of external polarizers and tuning slabs, the amplifier could be tuned to operate as high as 60 GHz, with 2.5 dB gain. The highest measured 3-dB bandwidth was 6% with the grid tuned for 54 GHz. The measured gain and tuning curves are consistent with modelled predictions. This is the first successful millimeter-wave monolithic grid amplifier using pHEMT's.

4.1. Introduction

The advantages of quasi-optical power combining become apparent at millimeter-wave frequencies. Traditional power combining—namely resonant waveguide and transmission-line combiners—perform very well at microwave frequencies. As the frequency increases, however, the traditional approaches begin to suffer from serious limitations. Conductor losses in the waveguide walls or transmission lines become greater, ultimately limiting the combining efficiency. By combining the power in free space, quasi-optics minimizes these losses.

Furthermore, the resonant cavities in waveguide combiners become increasingly difficult to machine as the wavelength becomes shorter. Moreover, the individual devices must often be painstakingly inserted and tuned by hand, making this approach practical for a only a relatively small number of elements. On the other hand, the planar nature of quasi-optical devices makes monolithic wafer-scale integration possible. The spacing between individual elements tends to scale with the wavelength; thus at higher frequencies, more devices can be incorporated into a chip of a given area. These increasing numbers tend to compensate for the natural power rolloff for the device, which is usually proportional with the inverse-square of the frequency.

To illustrate this point, consider the following hypothetical example. At 10 GHz, say a 1-inch square GaAs chip will accommodate a grid of 16 devices. If each device can produce 100 mW, the 16-element quasi-optical source will produce 1.6 W of power. At 100 GHz, these sources will only generate about 1 mW each. The same 1-inch chip, however, will now hold 1,600 devices. The total source power is still 1.6 W.

A number of passive monolithic diode grid arrays have been successful at millimeter-wave frequencies. These include multiplier arrays [1,2] which have been demonstrated as high as 1 THz [3], as well as phase shifters [4], and arrays for beam control [5]. However, until recently, the most successful active grid oscillators [6–8] and amplifiers [9–11] have all been hybrid constructions operating at microwave frequencies. Monolithic active grids have been more elusive.

This has not been due to lack of effort. In collaboration with Lockheed Martin Laboratories, an attempt was made at monolithic pHEMT grid oscillators. Grids designed to operate at 60 GHz and 94 GHz were fabricated and tested. Fig. 4.1 shows a portion of a monolithic grid designed for 94 GHz. The results were disappointing. On a positive note, the arrays did oscillate with single-frequency locked output spectra, as illustrated in Fig. 4.2. The grids designed

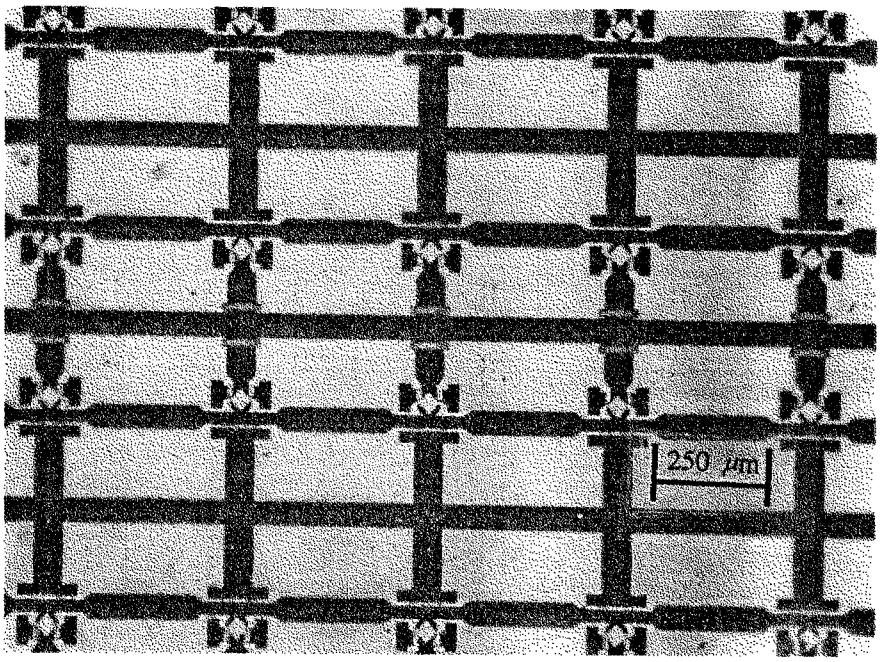

Fig. 4.1. Microscope photograph of a monolithic pHEMT grid oscillator designed for 94 GHz. The unit cell size is 440 μm.

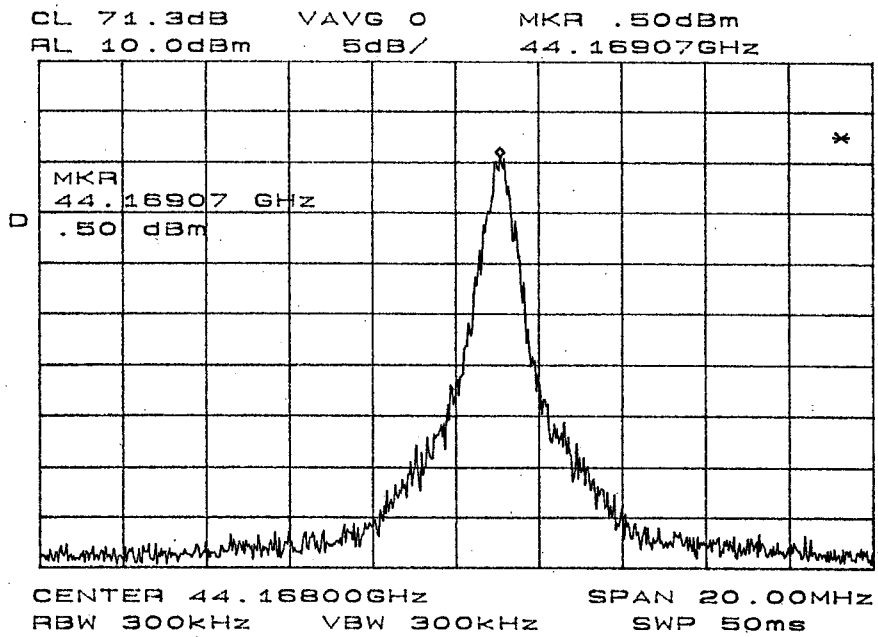

Fig. 4.2. Output spectrum of a monolithic grid designed to oscillate at 60 GHz. The center frequency is 44.2 GHz. The vertical scale is 5 dB/division, and the horizontal scale is 2 MHz/division.

for 60 GHz tended to oscillate at 44 GHz, while the grids designed for 94 GHz operated near 65 GHz. The low output power, poor radiation patterns, and high cross-polarization levels, however, led to the conclusion that the grids were dominated by substrate-mode oscillations, like the ones described in [12]. Much time was spent and a variety of methods were attempted—including using a laser to trim parts of the grid—to suppress these undesirable oscillations. Unfortunately, none of these attempts were successful. Although these substrate modes are not completely understood, it is suspected that the rather high dielectric constant of the GaAs substrate is the likely suspect. All previous hybrid grid oscillators were built on low-dielectric Duroid. In the monolithic arrays, the devices were probably spaced too far apart relative to a dielectric wavelength, and substrate modes dominated. Experiments with hybrid grids on high-dielectric substrates support this conclusion. Somewhat better results have been measured from monolithic HBT oscillator grids [13], but again the radiation patterns show stong evidence of the existence of substrate modes. More detailed studies of substrate modes and their suppression are currently being performed by Polly Preventza at Caltech.

Very recently, however, successful monolithic quasi-optical amplifiers have been demonstrated at millimeter-wave frequencies. Researchers at Rockwell International have reported gain from slot-patch arrays using HBT [14] and pHEMT [15] devices. Furthermore, a 36-element monolithic HBT grid amplifier has produced 5 dB gain at 40 GHz, with 670 mW of saturated output power [16]. The remainder of this chapter will discuss the design and performance of a 44-60 GHz pHEMT grid amplifier [17].

4.2. First Iteration Grid

Based on the success of early hybrid grid amplifiers [9,10], an attempt was made at a monolithic millimeter-wave grid amplifier. This project was a collaborative effort between Caltech and Lockheed Martin Laboratories. The grids were fabricated using the 0.1-μm pHEMT technology developed by Lockheed Martin. The devices are similar to the ones used for the hybrid 100-element amplifier discussed in the previous chapter. Amplifiers using these pHEMT's have produced gain at frequencies as high as 100 GHz [18].

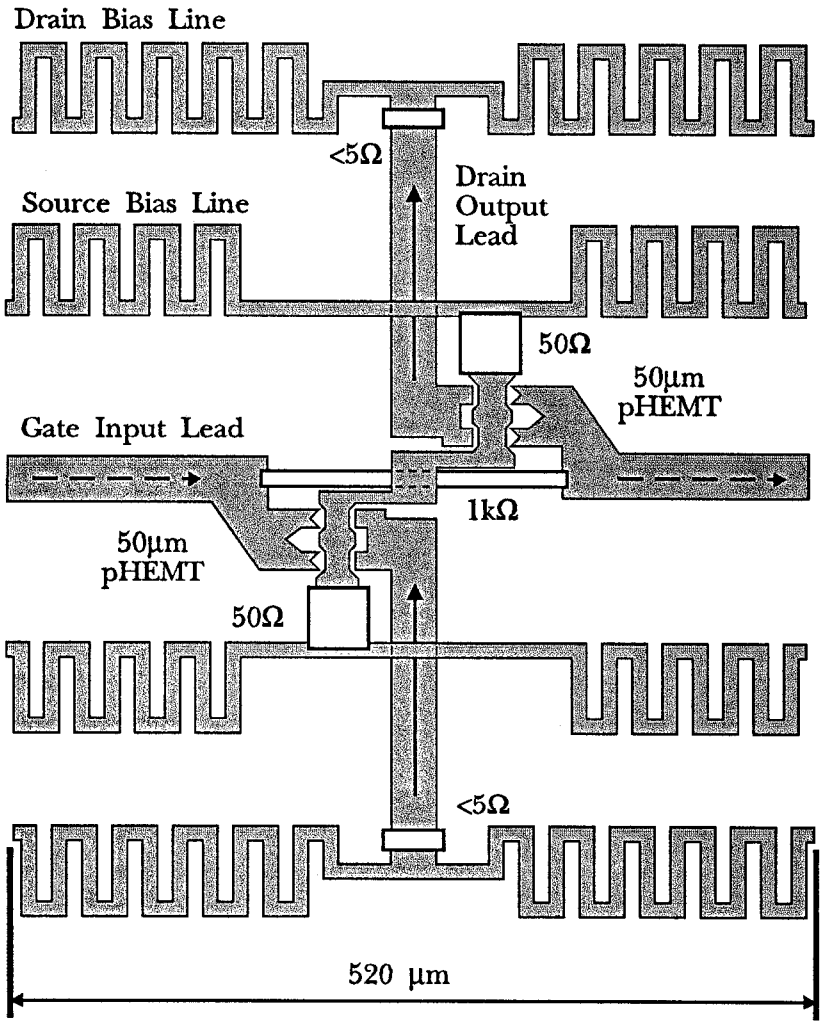

Fig. 4.3. The grid amplifier unit cell. Arrows indicate the directions of rf currents.

Fig. 4.3 shows the unit cell layout. Each cell contains two 0.1-μm pHEMT's, with the sources tied together to form a differential pair. Each transistor has a gate width totalling 50 μm, distributed among four fingers. The 1-kΩ resistor allows the gate bias to pass from cell to cell. This is possible because the gate draws very little bias current. The gate bias resistor passes under the air-bridged source connection. The two 50-Ω source resistors are intended to reduce the common-mode gain. The unit cell is 520 μm on a side, intentionally kept small in an attempt to avoid exciting substrate modes, as discussed earlier. The input beam is coupled to the gates of the transistor pair through the horizontal input leads. These leads also supply bias to the gates. The output beam is radiated from the vertical drain leads. The small resistors in the drain leads are used for probing and diagnostics. The thin meandering lines supply bias to the drain and source. The entire array is fabricated on a 15-mil GaAs substrate. Figs. 4.4 and 4.5 are photographs of the monolithic grids.

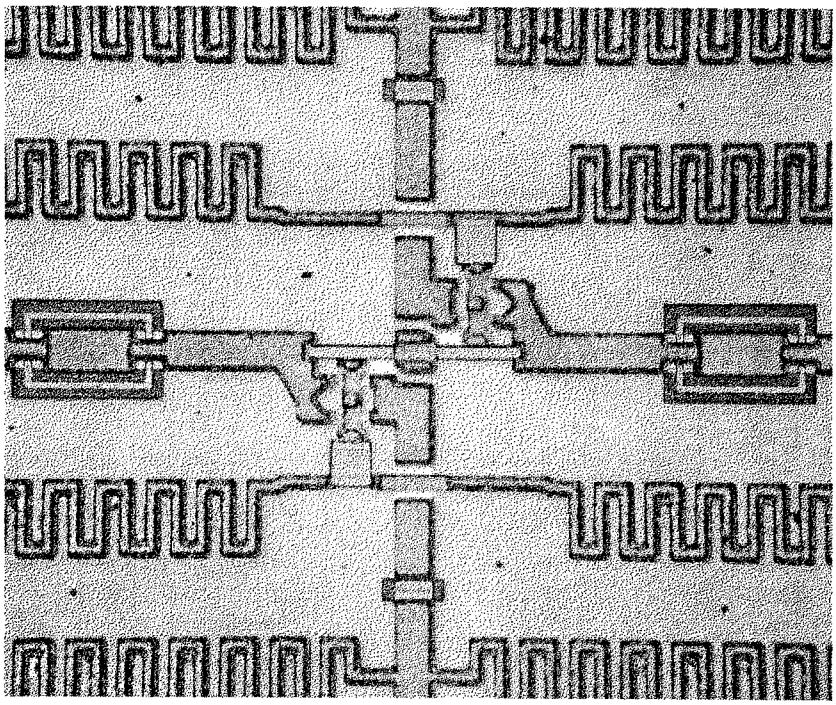

Fig. 4.4. Microscope photograph of a unit cell. The cell size is 520 μm.

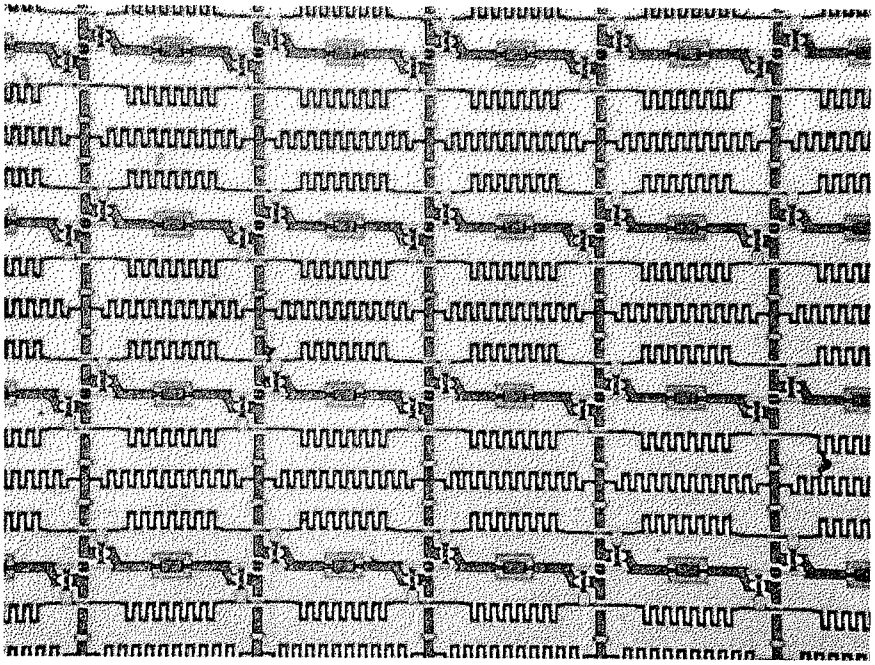

Fig. 4.5. Several unit cells. The cell size is 520 μm.

4.2.1. Measurements

The 36-element grids were dc probed to screen out chips with poor device yields. The rf gain was measured using the far-field approach [9,10], as illustrated in Fig. 4.6. The grid is placed in between two cross-polarized horn antennas, each with an effective area A_h. The active area of the grid is A_g. The power intercepted by the grid P_g is then given by Friis transmission formula [19]:

$$\frac{P_g}{P_t} = \frac{A_h A_g}{(\lambda R_{ff})^2}, \tag{4.1}$$

where P_t is the transmitted power and λ is the wavelength. The grid-horn spacing

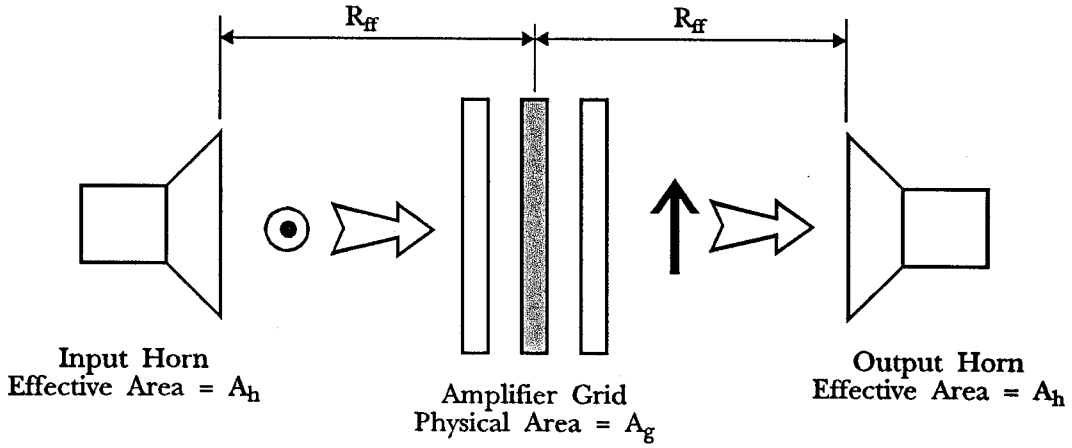

Fig. 4.6. Far-field setup used to measure the monolithic amplifier grids.

R_{ff} is set at the far-field distance [19]:

$$R_{ff} = \frac{2D^2}{\lambda} \approx \begin{cases} 2A_h/\lambda & A_h > A_g \\ 2A_g/\lambda & A_g > A_h. \end{cases} \tag{4.2}$$

This gives a grid power given by:

$$\frac{P_g}{P_t} \approx \begin{cases} A_g/(4A_h) & A_h > A_g \\ A_h/(4A_g) & A_g > A_h. \end{cases} \tag{4.3}$$

This function is plotted in Fig. 4.7. In order to maximize the power intercepted by the grid, the area of the horns should be roughly equal to the active area of the array. Originally, the gain measurements were performed using standard-gain pyramidal horn antennas with effective areas much greater than that of the grid. This results in a vanishingly small fraction of the transmitted power actually incident of the array. Not surprisingly, very little difference between the response with the grid biased and unbiased could be measured.

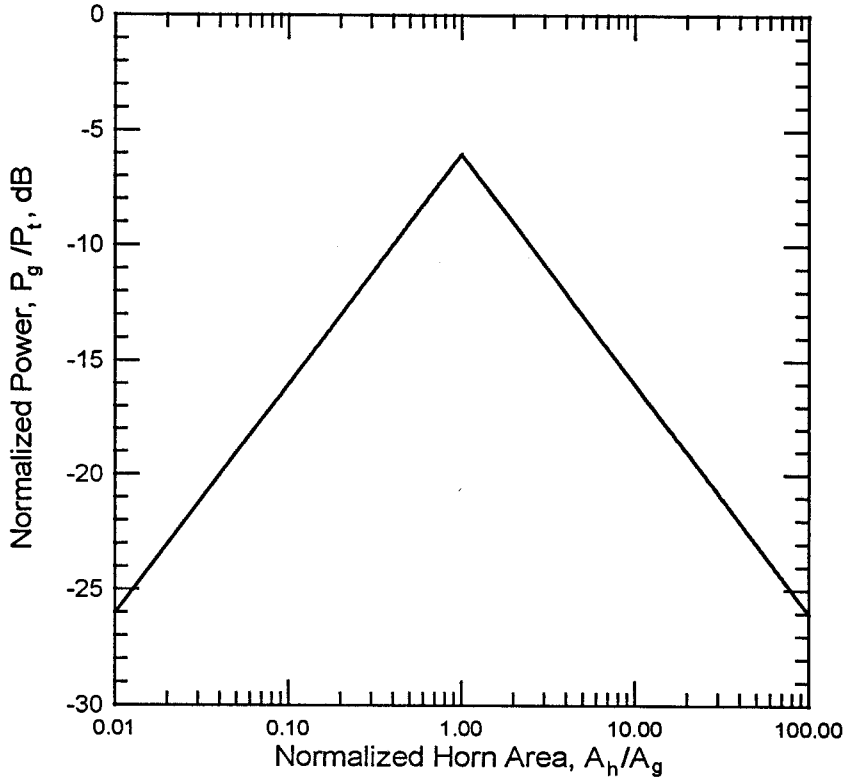

Fig. 4.7. Power intercepted by the grid as a function of the effective area of the input and output horns. The power is maximum when the horn area is the same as the active area of the grid.

Better results were obtained using open-ended waveguide as the input and output antennas. The waveguide apertures had an area comparable to that of the grid. This allowed the antennas to be placed much closer to the amplifier, resulting in a higher power incident on the array. Fig. 4.8 shows the measured gain versus frequency. The on-off ratio at 48 GHz is 15 dB. The peak gain of the grid, however, is only slightly greater than 0 dB.

Row-by-row measurements of the pHEMT's dc characteristics give an indication as to why the gain of the grid is so low. Perhaps the most important parameter of any FET is the transconductance, g_m. This quantity relates the

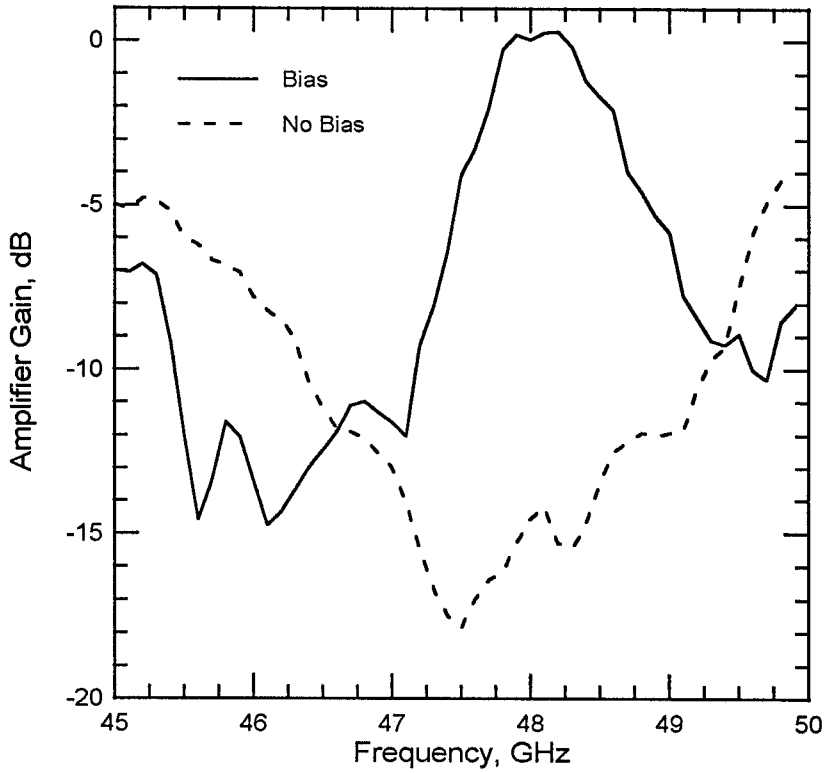

Fig. 4.8. Measured gain versus frequency for the first iteration monolithic grid amplifier. The peak gain is 0 dB.

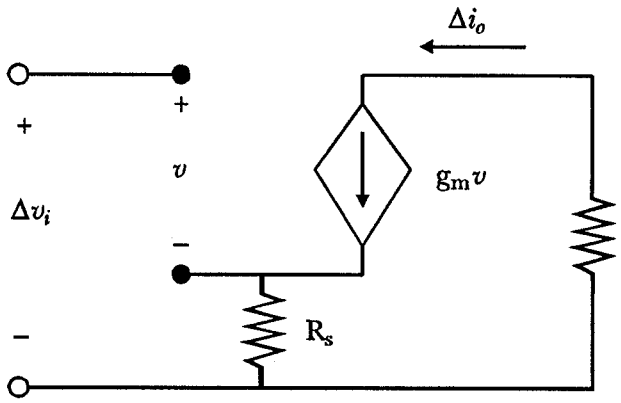

Fig. 4.9. FET equivalent circuit model used to relate the intrinsic transconductance g_m to the external transconductance g_m^{ext}. In the dc measurement, $g_m^{ext} = \Delta i_o / \Delta v_i$.

output drain current to the input gate voltage. If there is any resistance in the source of the device R_s, the extrinsic transconductance g_m^{ext} that one measures from the accessible device terminals will be lower than the intrinsic transconductance g_m of the device itself. Fig. 4.9 shows the device equivalent circuit model used to relate g_m and g_m^{ext}. The extrinsic transconductance is measured directly:

$$g_m^{ext} = \frac{\Delta i_o}{\Delta v_i}, \tag{4.4}$$

where i_o is the output drain current and v_i is the input gate voltage. The intrinsic g_m is related to this measurement through the relation:

$$\frac{1}{g_m^{ext}} = \frac{1}{g_m} + R_s. \tag{4.5}$$

For these grids, the average measured g_m^{ext} was 11.1 mS per transistor. The total source resistance, including the 50-Ω common-mode gain reduction resistor, is about 58 Ω. This yields an intrinsic transconductance of 31 mS. The amplifier grids were designed assuming a g_m of 54 mS. This difference could account for as much as 5 dB of gain reduction.

The designer of a monolithic circuit often has very little control over the fabricated device performance. A flaw in the design of these first iteration grids that can be corrected, however, is evident in the unit cell layout of Fig. 4. The connection between the sources is a rather long, thin metal trace. Associated with this trace will be a considerable inductance. Excess source inductance is notorious for reducing the gain of high-frequency amplifiers. Quasi-static modelling indicates that this excess parasitic source inductance may be as high as 33 pH per transistor. This inductance was not accounted for in the original grid design. A second iteration design would have to greatly reduce the inductance of this source connection.

4.3. Second Iteration Grid

The unit cell layout for the second iteration grids is shown in Fig. 4.10. The devices are rearranged so that the sources are much closer together, resulting in a greatly reduced source inductance. Quasi-static analysis indicates that the parasitic source inductance in the new design is 7 pH per transistor, as opposed to 33 pH for the original design. The cell is otherwise identical to the first iteration design.

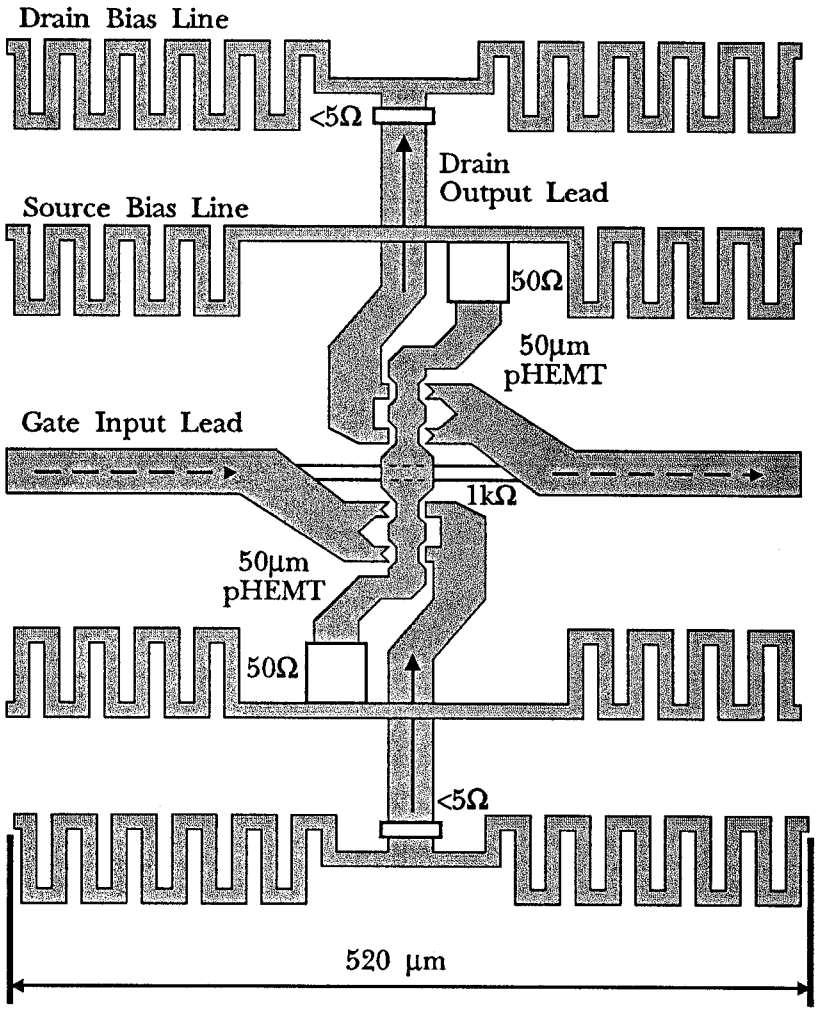

Fig. 4.10. The grid amplifier unit cell. Arrows indicate the directions of rf currents.

Fig. 4.11 plots the maximum gain for the pHEMT's for the two designs. The first iteration includes an additional parasitic source inductance of 33 pH. In this case, the device is unconditionally stable, so we plot the Maximum Available Gain (MAG). In the second iteration, the parasitic source inductance is reduced to 7 pH. The device is potentially unstable below 58 GHz, so we plot the Maximum Stable Gain (MSG). Above this frequency, we plot the MAG. At 50 GHz, the new design has about 3 dB higher gain.

dc measurements also indicate that the device performance was much improved in the second iteration. The average extracted intrinsic transconductance was 43 mS. This is still lower than the design value of 54 mS, but is considerably better than the value of 31 mS for the first iteration grids. This improvement in the devices should account for a gain improvement of about 3 dB.

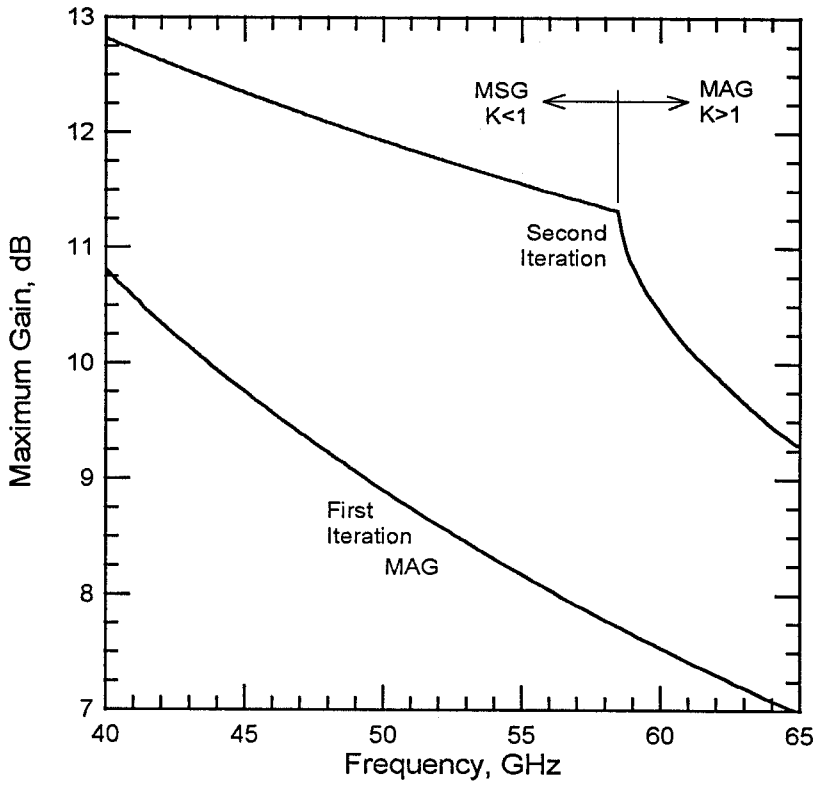

Fig. 4.11. Maximum gain of the pHEMT's for the two iterations. The first iteration includes a parasitic source inductance of 33 pH; for the second iteration this inductance is reduced to 7 pH.

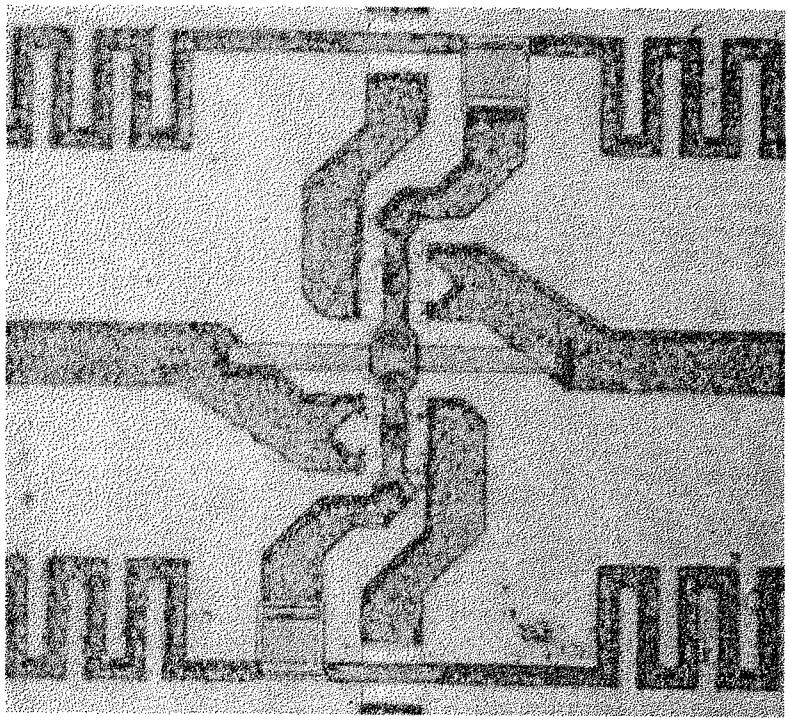

Fig. 4.12. Microscope photograph showing the differential pair layout for the second iteration grids.

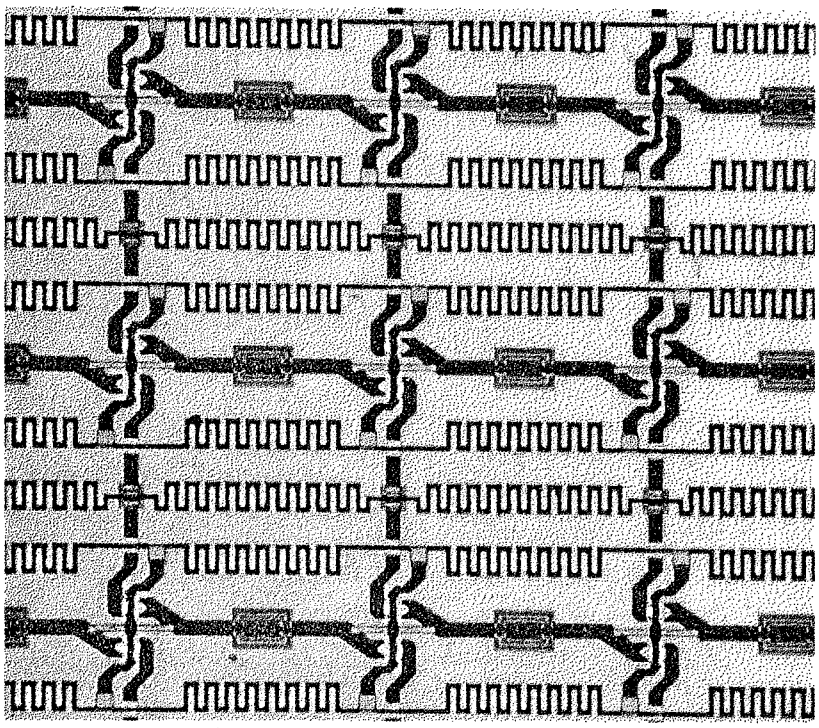

Fig. 4.13. Several unit cells of the second iteration grids. The cell size is 520 μm.

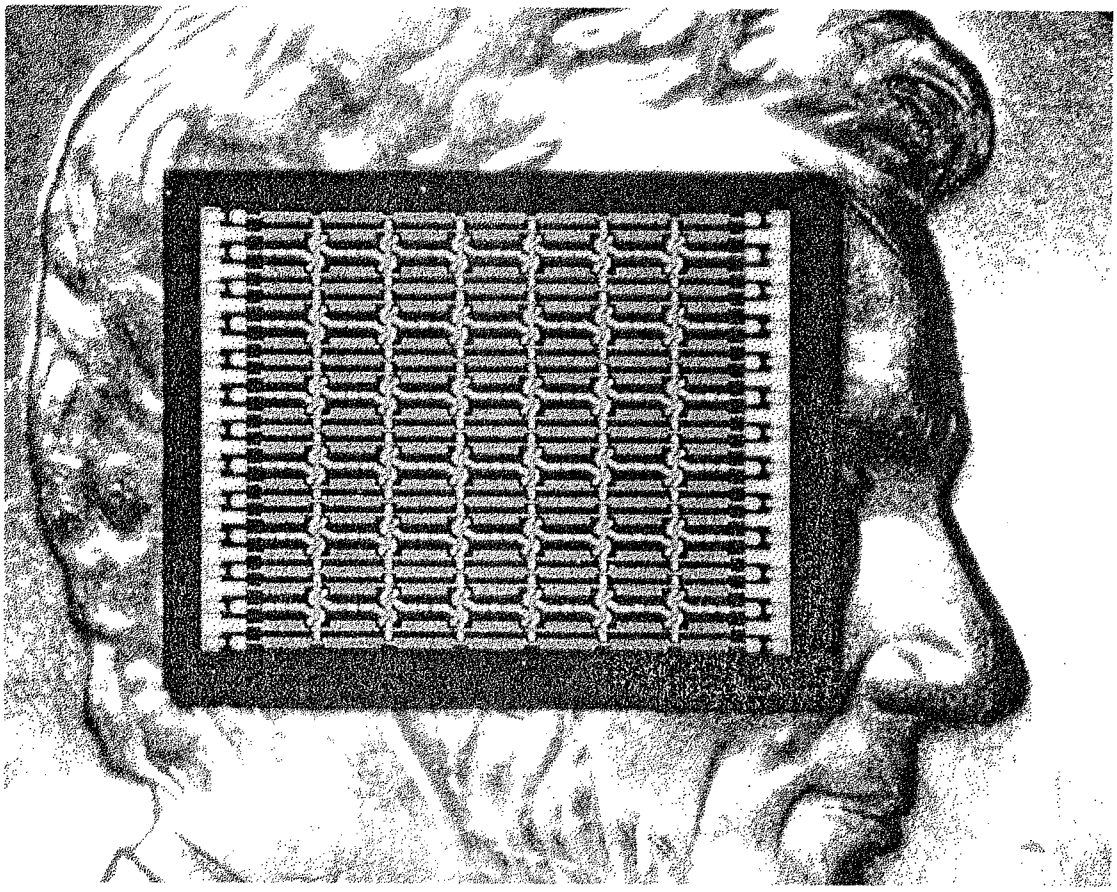

Fig. 4.14. Photograph of the 36-element grid compared with a penny. The active area of the grid is 3.1 mm on a side.

Figs. 4.12 and 4.13 are photographs of the fabricated arrays. A photograph of an entire 6×6 array is shown in Fig. 4.14. Larger 18×18 arrays were also fabricated. dc probing of the larger arrays, however, revealed that these grids were unusable due to poor device yields.

4.3.1. Gain Measurements

Fig. 4.15 shows the setup used to measure the gain. To increase the power incident on the grid, the input and output antennas were open-ended WR-22 or WR-15 waveguide with the flanges sawed off. An HP83620A synthesizer fed an HP8355-series multiplier to generate the millimeter-wave power. An HP8563A

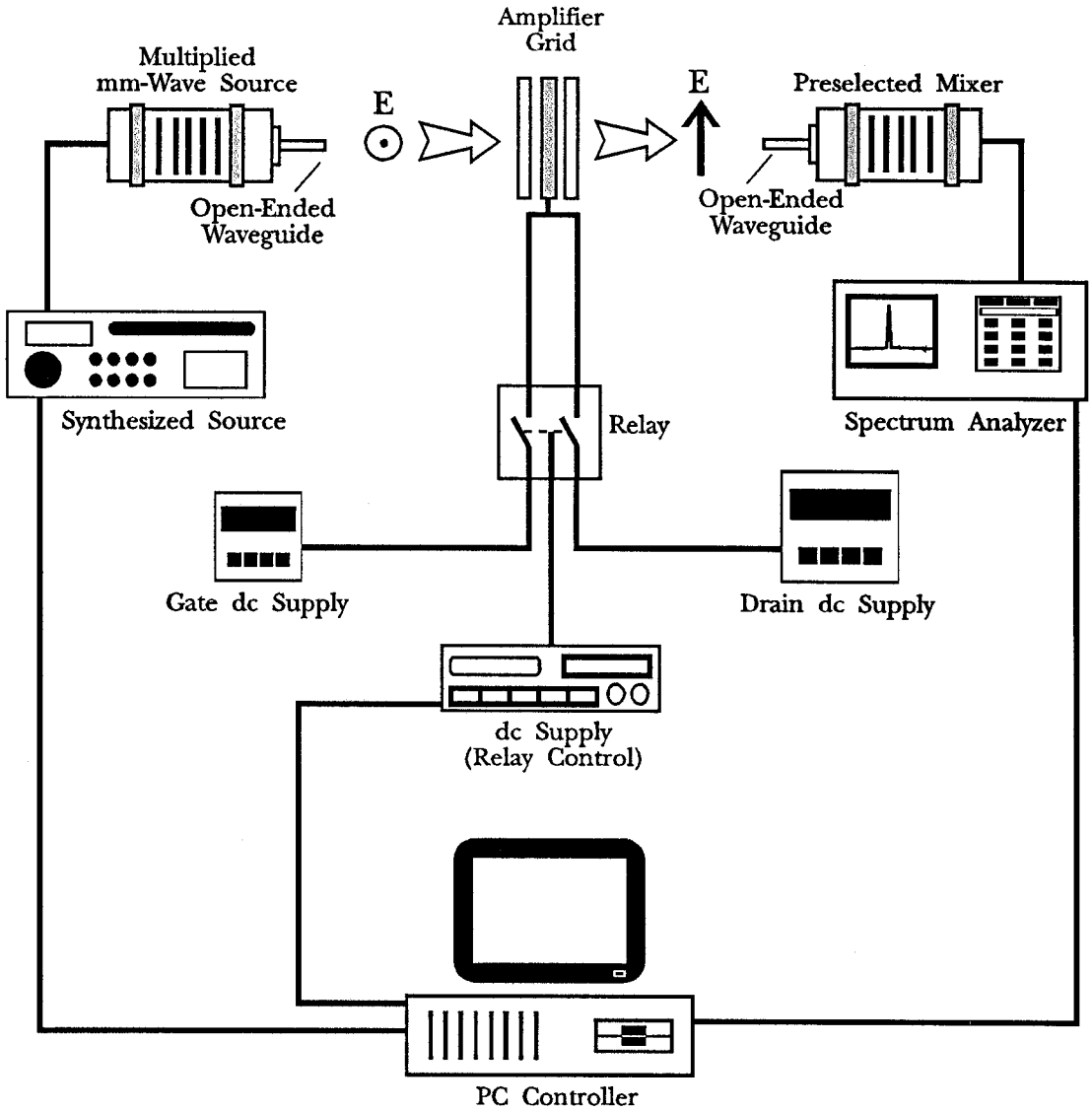

Fig. 4.15. Setup used to measure the millimeter-wave gain

spectrum analyzer with an HP11974-series preselected mixer was used to receive the amplifier output. The gate and drain bias were each supplied by a single dc source. To avoid overheating, the grid was only biased for a second at a time. The entire setup was computer-controlled, using software written by Cheh-Ming Liu, to facilitate data collection.

The assembled amplifier is shown in Fig. 4.16(a). The grid is fabricated on a 15-mil GaAs substrate and then mounted on a Duroid board with a relative dielectric constant of 2.33. The polarizers are also fabricated on low-dielectric Duroid. The corresponding transmission-line equivalent circuit is shown in Fig. 4.16(b). This is a half-cell model, so free space is represented by the 189-Ω resistors. The air gaps and substrates appear as transmission lines. The gate and drain leads are modelled as inductors. The polarizers appear as low-impedance inductors or high-impedance capacitors, depending on the polarization. Numerical values for these reactive elements were computed using the method of moments to estimate the surface current distribution, and then using the induced emf method to calculate the impedance. The meandering bias lines appear as a shunt inductance at the input surface of the grid. Numerical values for this element were determined empirically, with the aid of Hewlett-Packard's High Frequency Structure Simulator (HFSS) [20]. Further details regarding the modelling can be found in Chapter 3 and Appendix A of this thesis.

Fig. 4.17 shows the measured small-signal gain of the amplifier. The grid is completely stable; no spurious oscillations were observed. The peak gain is 6 dB at 48 GHz. The 3-dB gain bandwidth is 1.7 GHz, which corresponds to 3.5%. Without bias, the gain is below –5 dB over the entire frequency range. At peak gain, the on-off ratio is over 30 dB. An on-off ratio this high is a good indication that the amplifier is operating correctly. The gain modelled from the equivalent circuit shown in Fig. 4.16(b) is also plotted. The agreement is quite good, although the model overpredicts the gain by about 3 dB. It should be

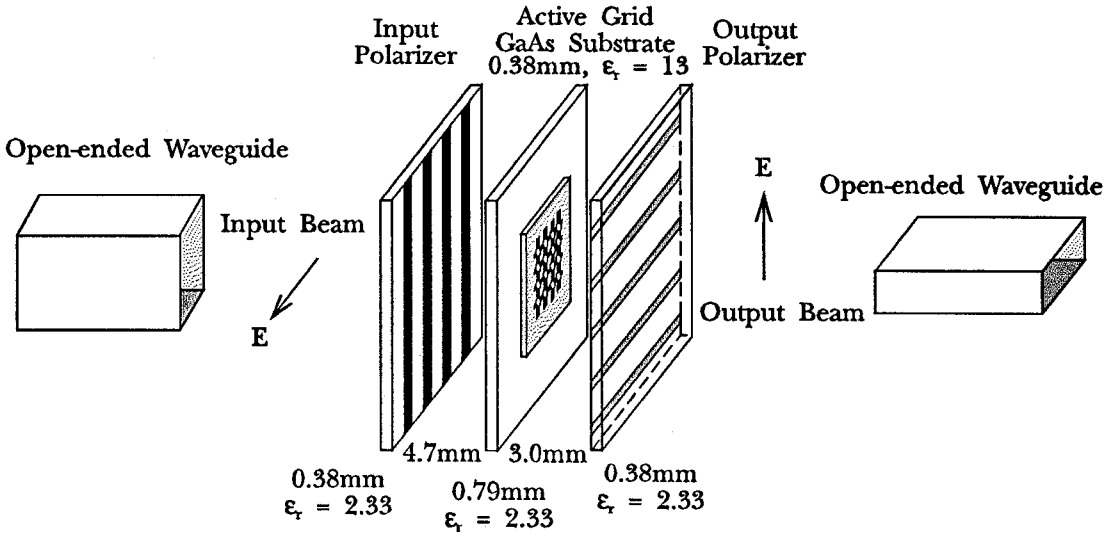

(a)

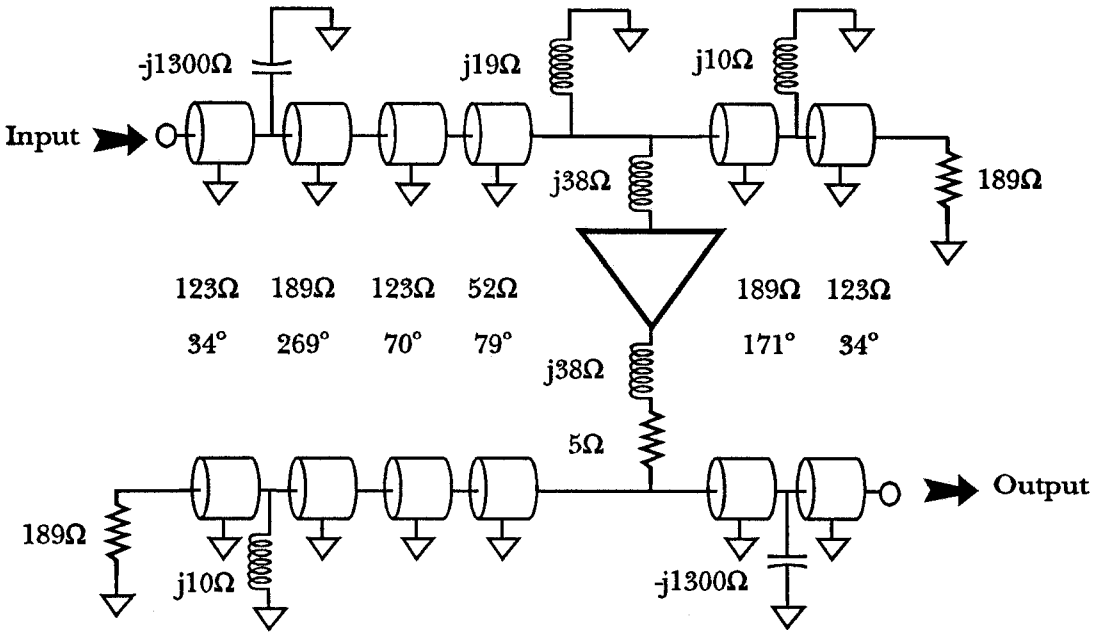

(b)

Fig. 4.16. The assembled amplifier grid (a), and the transmission-line equivalent circuit model (b) for the grid at 48 GHz.

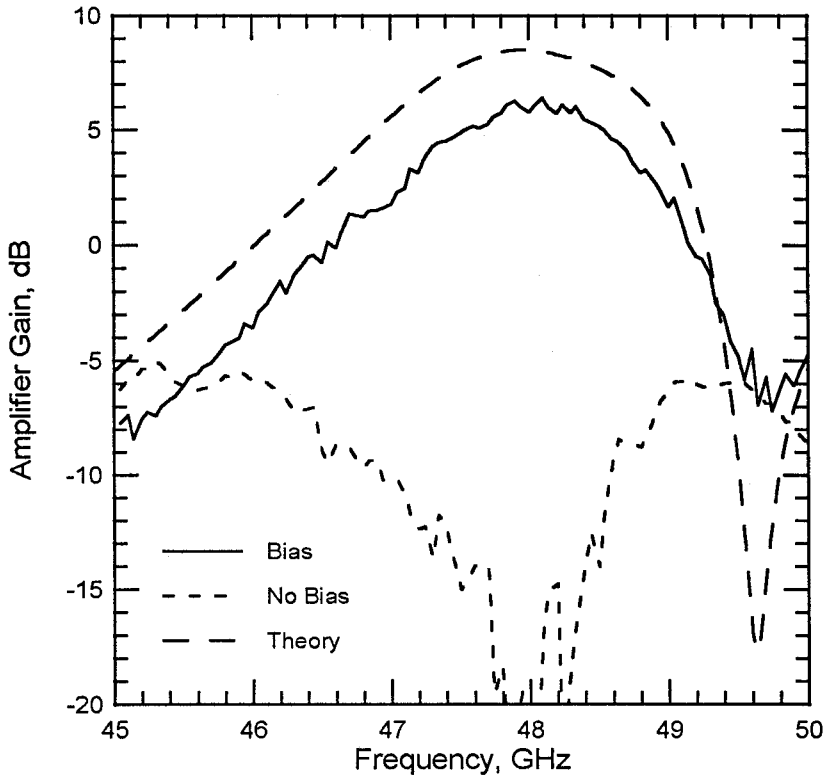

Fig. 4.17. Measured amplifier gain versus frequency. The polarizer positions are shown in Fig. 4.16.

noted that the theoretical curve was generated assuming the transconductance of the pHEMT was 43 mS, as indicated by dc row-by-row measurements. Gain at 48 GHz as a function of bias current is shown in Fig. 4.18. The current was varied under a constant drain bias of 3 V by changing the gate bias. The amplifier reaches its maximum gain at a transistor current of 8 mA.

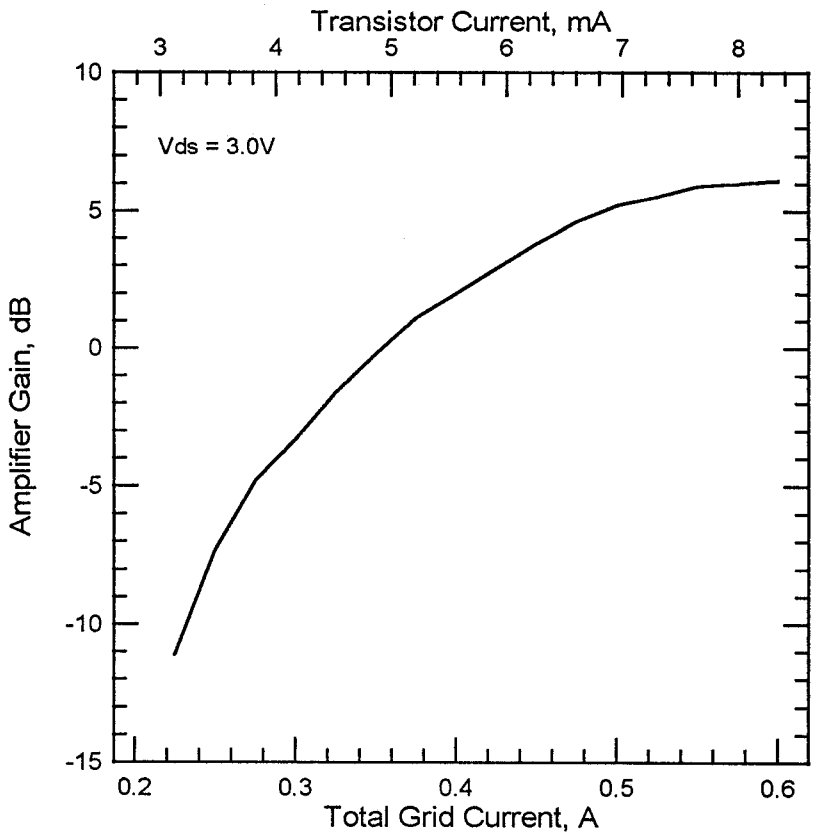

Fig. 4.18. Amplifier gain at 48 GHz as a function of bias current. Further increases in the current are unlikely to increase the gain significantly.

To further validate the modelling, the gain was measured as a function of polarizer position. Fig. 4.19 shows the gain at 48 GHz versus input polarizer position. The input polarizer actually tunes the output circuit of the grid. Fig. 4.20 shows the gain as a function of output polarizer position. Again, aside from a gain overprediction, the model agrees quite well with the measured results.

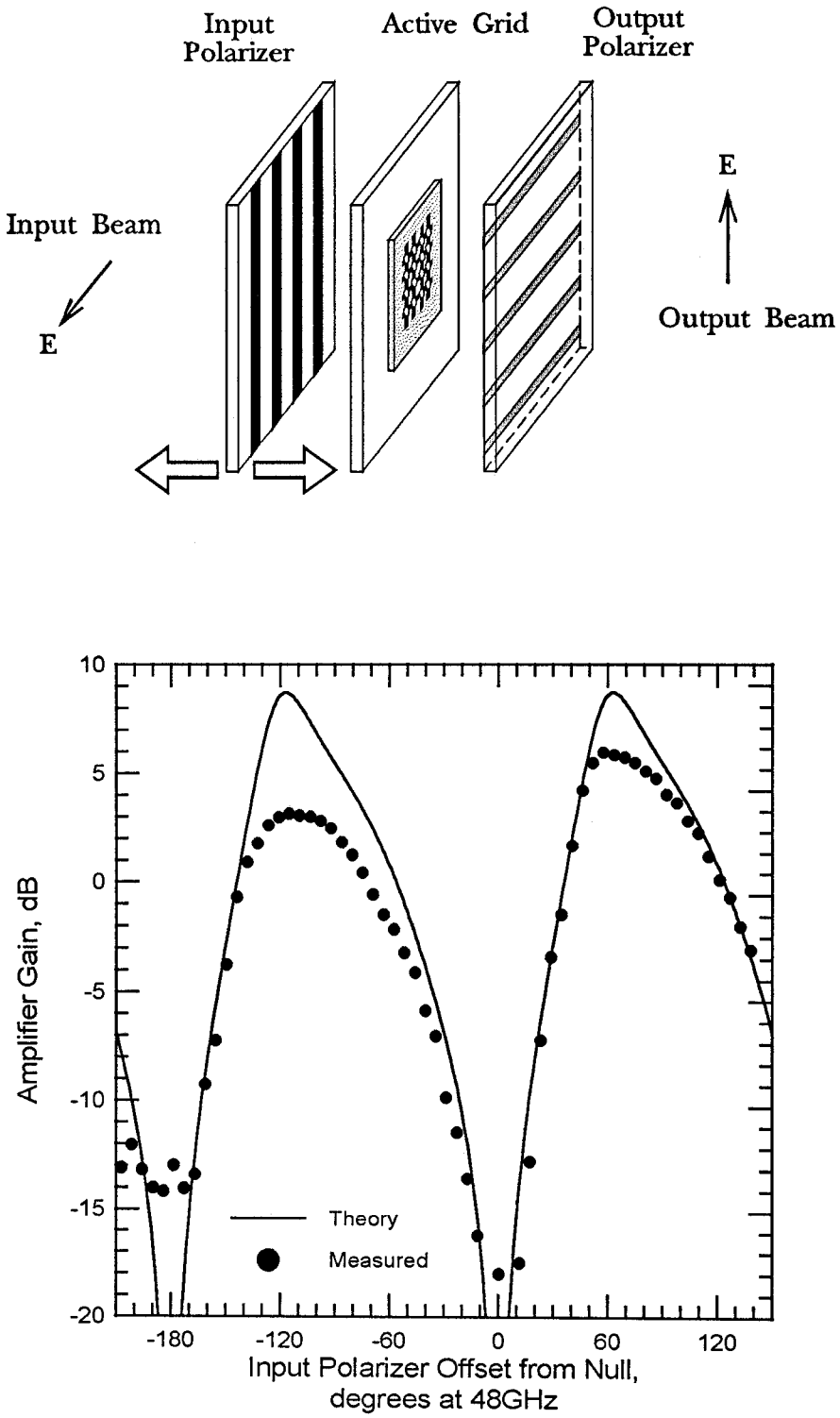

Fig. 4.19. Amplifier gain at 48 GHz as a function of input polarizer position.

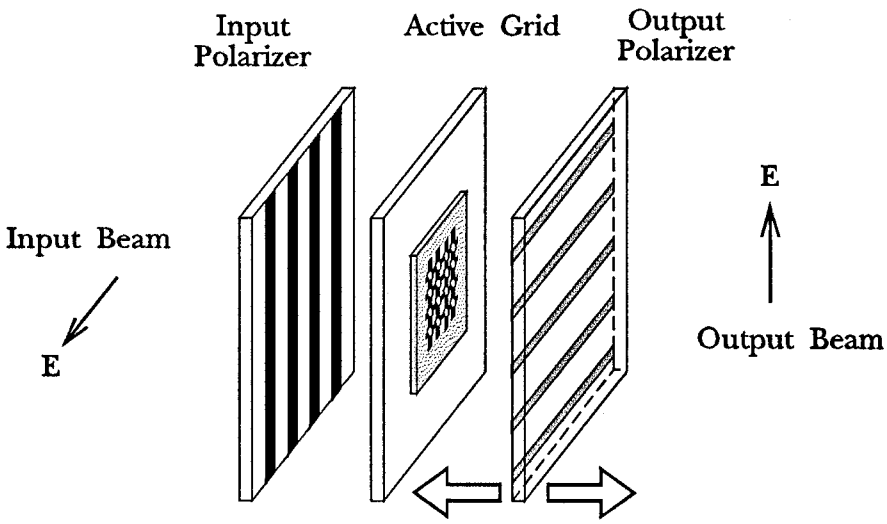

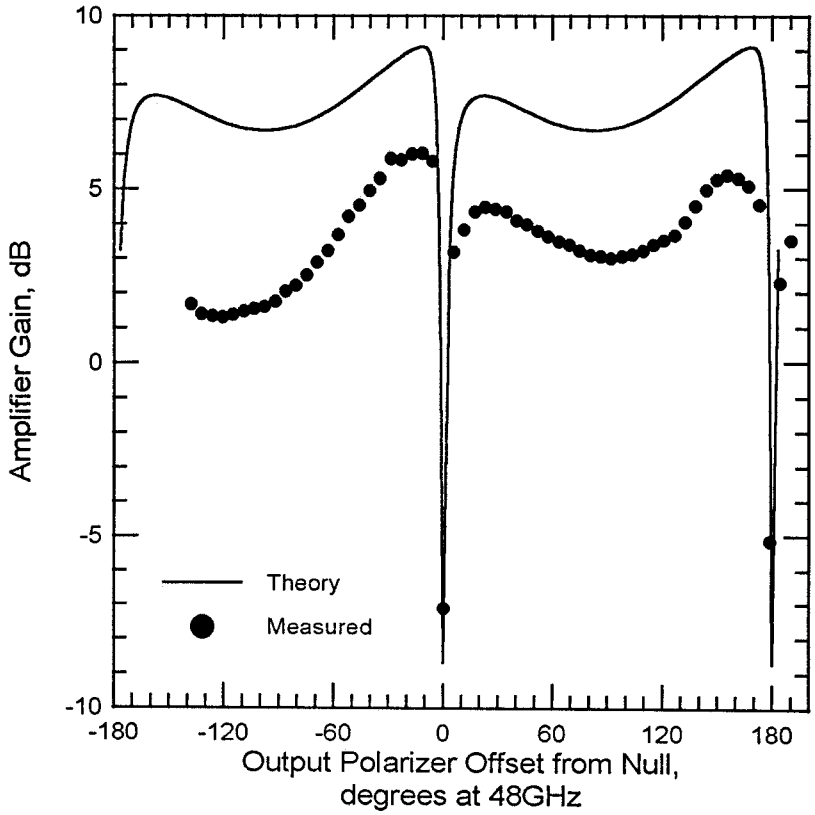

Fig. 4.20. Amplifier gain at 48 GHz as a function of input polarizer position.

4.3.2. Tuning Range

Simply by changing the positions of the input and output polarizers, the amplifier can be tuned to operate at other frequencies. Figs. 4.21 through 4.23 show the amplifier configurations and equivalent circuit models for the amplifier tuned for 44, 54, and 60 GHz. The measured gain curves are shown in Figs. 4.24 through 4.26. The peak gain when tuned for 44 GHz is 6.5 dB, with a 3-dB bandwidth of 2.0 GHz (4.5%). The peak gain when tuned for 54 GHz is 4 dB, with a 3.2 GHz (6%) bandwidth. The highest frequency the amplifier was tuned to was 60 GHz. The peak gain is 2.5 dB, with a bandwidth of 2.0 GHz (3.3%). This is the highest operating frequency for a quasi-optical amplifier to date. It should be noted that in the 60 GHz measurement, a high-dielectric Duroid slab was used as an output tuner to increase the gain. In addition, the noise floor of the spectrum analyzer prevented measuring gain below –15 dB for the 54 and 60 GHz measurements. All four gain curves are plotted in Fig. 4.27, along with the maximum gain of the device for comparison. The performance characteristics are summarized in Table 4.1.

Frequency GHz	Gain dB	On-Off Ratio dB	Bandwidth GHz	Bandwidth %
44	6.5	30	2.0	4.5
48	6.0	30	1.7	3.5
54	4.0	> 20	3.2	6.0
60	2.5	> 15	2.0	3.3

Table 4.1. Summary of the grid's performance when tuned for various U-band frequencies.

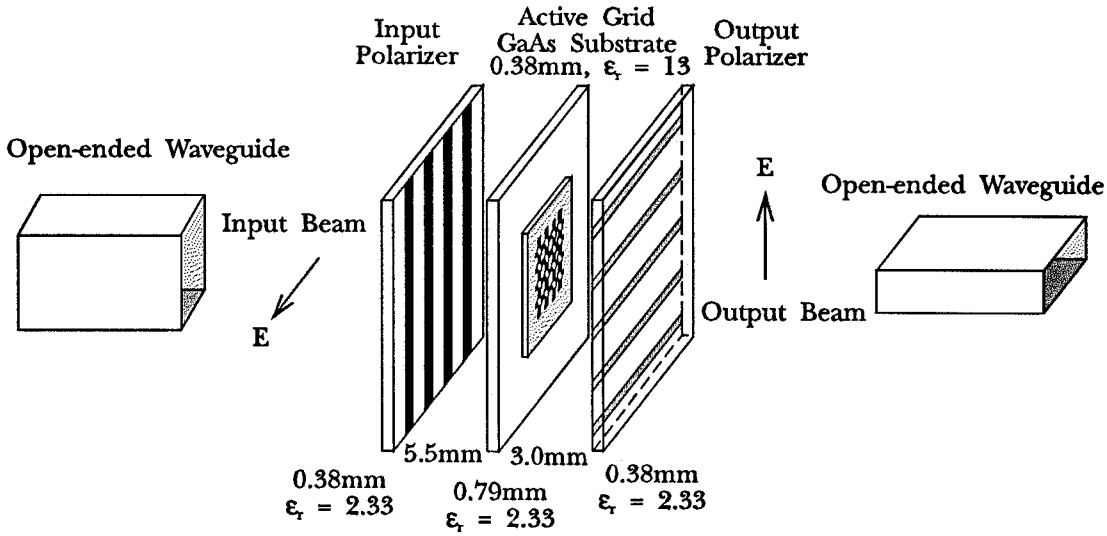

(a)

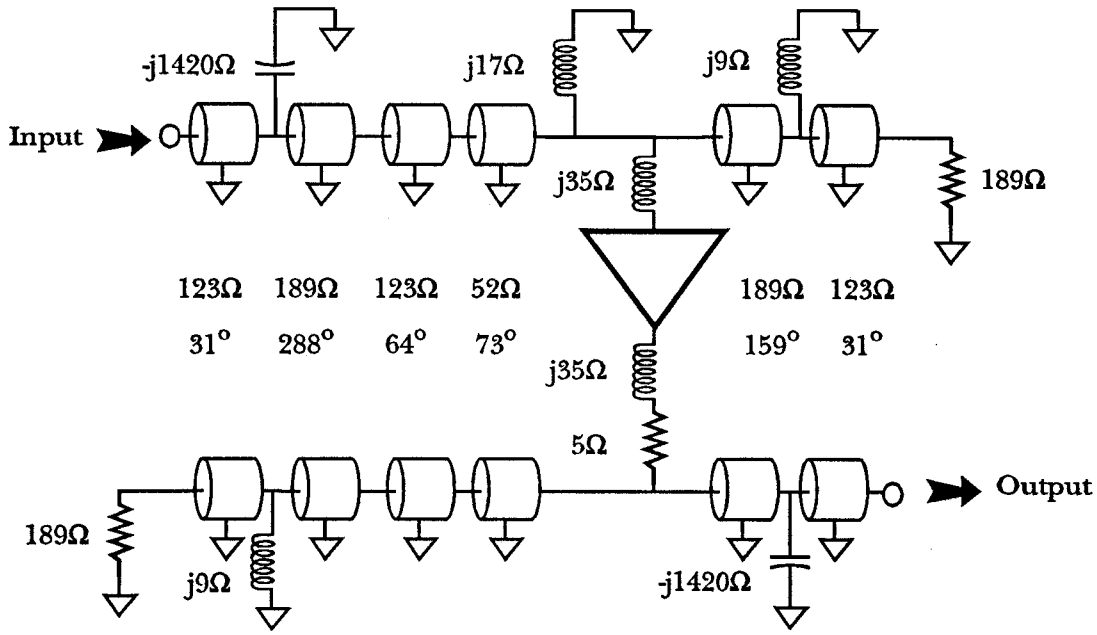

(b)

Fig. 4.21. The assembled amplifier grid when tuned for 44 GHz (a), and the transmission-line equivalent circuit model (b) for the grid at 44 GHz.

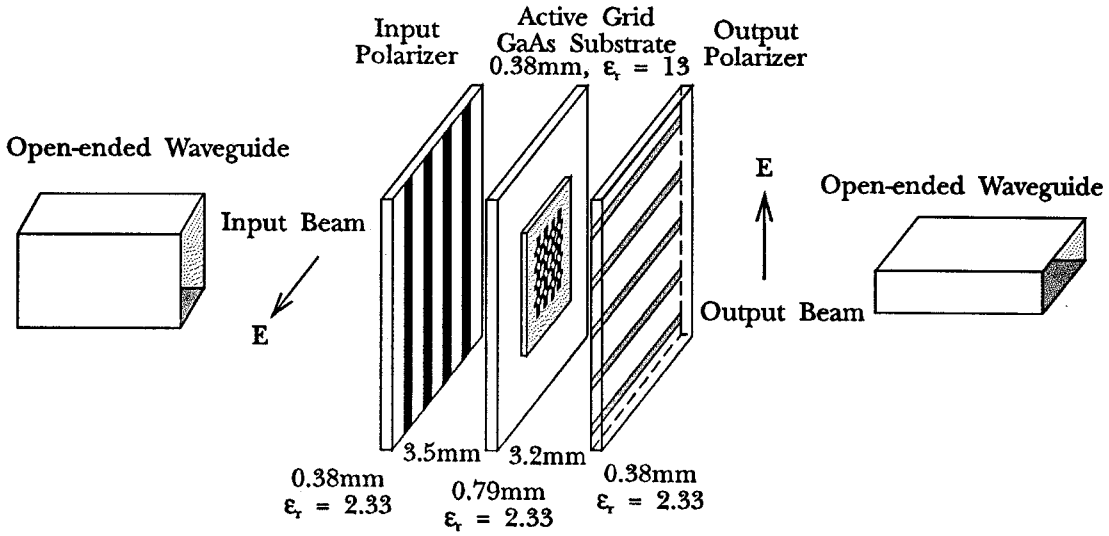

(a)

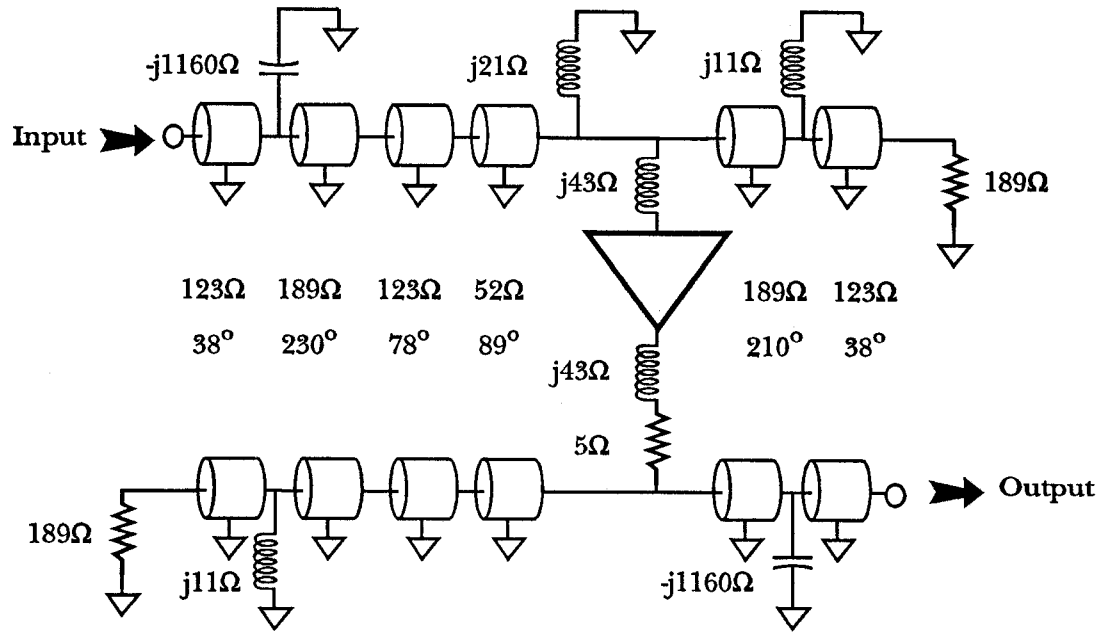

(b)

Fig. 4.22. The assembled amplifier grid when tuned for 54 GHz (a), and the transmission-line equivalent circuit model (b) for the grid at 54 GHz.

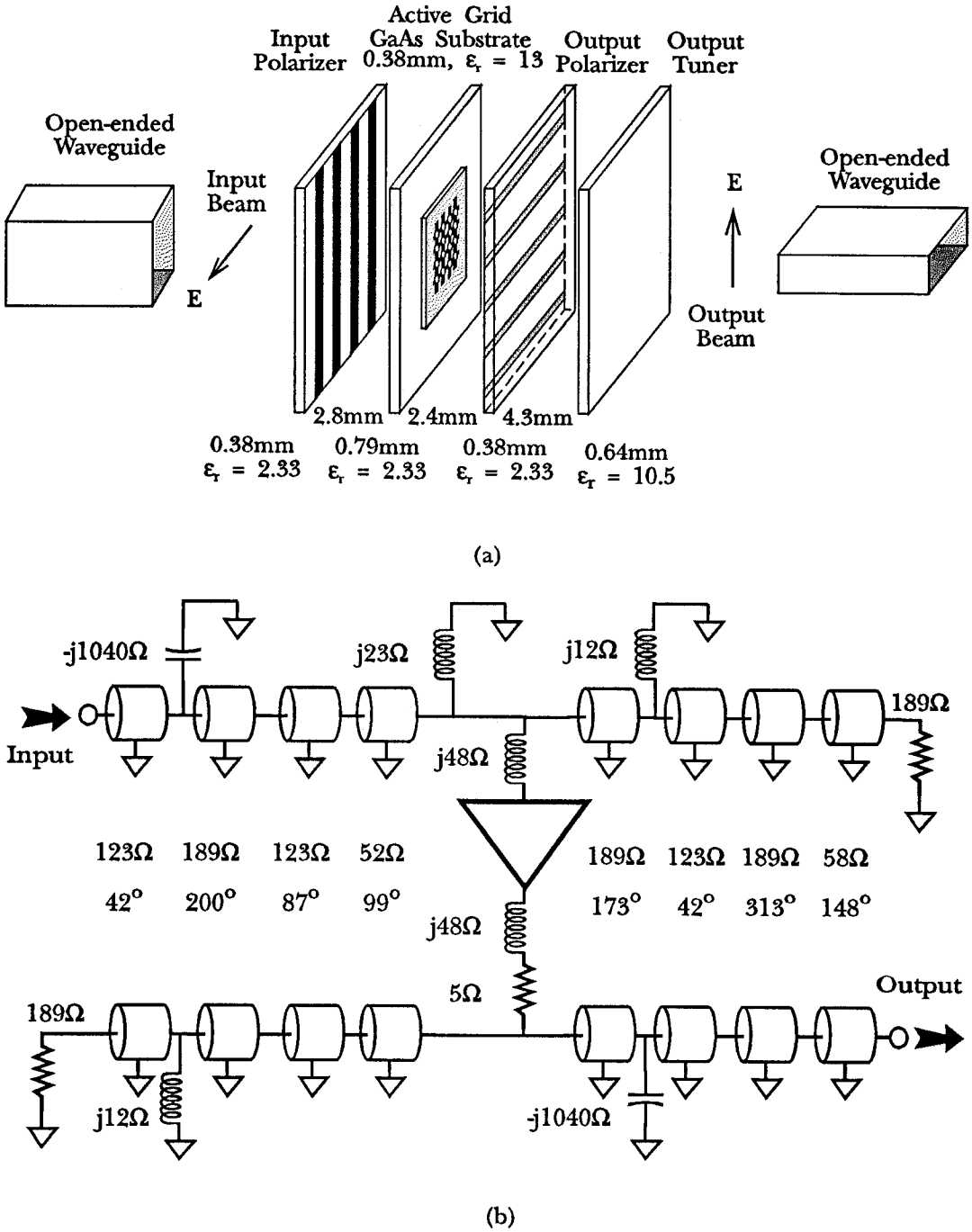

Fig. 4.23. The assembled amplifier grid when tuned for 60 GHz (a), and the transmission-line equivalent circuit model (b) for the grid at 60 GHz.

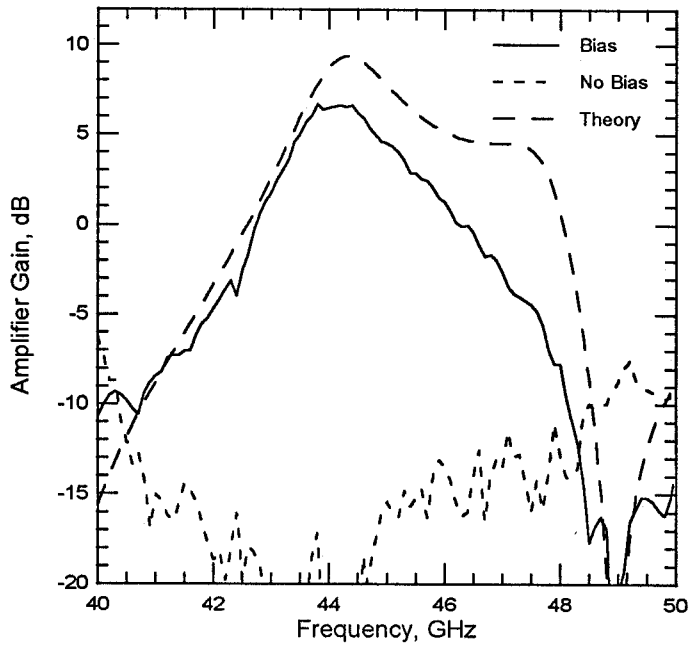

Fig. 4.24. Grid amplifier gain versus frequency for the amplifier tuned for 44 GHz. The polarizer positions are shown in Fig. 4.21.

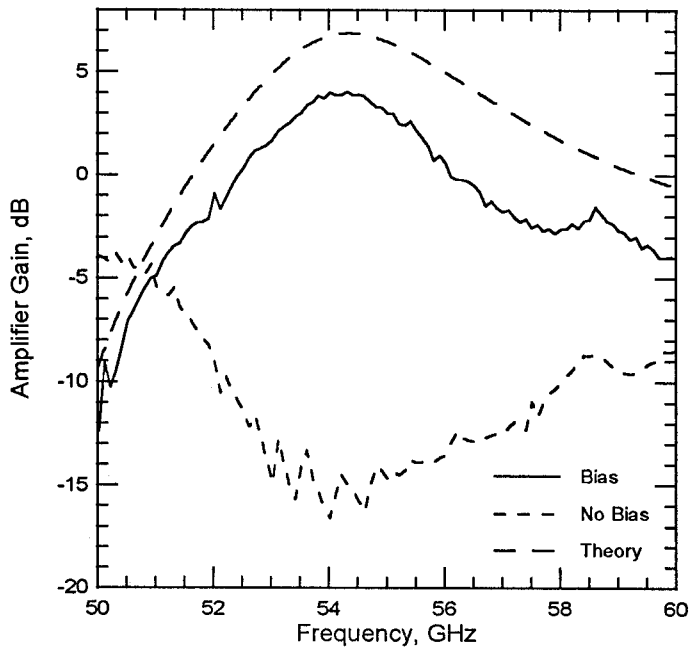

Fig. 4.25. Grid amplifier gain versus frequency for the amplifier tuned for 54 GHz. The noise floor of the spectrum analyzer prevent measuring gain below −15 dB. The polarizer positions are shown in Fig. 4.22.

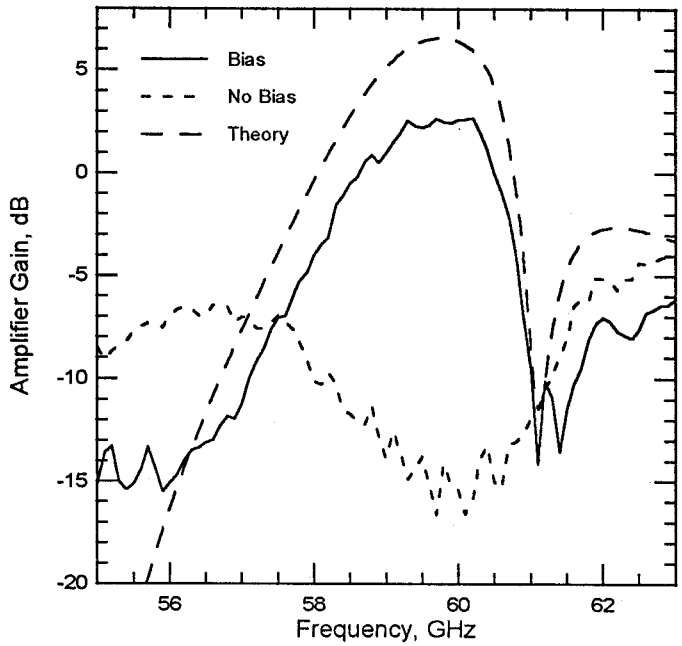

Fig. 4.26. Grid amplifier gain versus frequency for the amplifier tuned for 60 GHz. The noise floor of the spectrum analyzer prevent measuring gain below −15 dB. The polarizer and tuner positions are shown in Fig. 4.23.

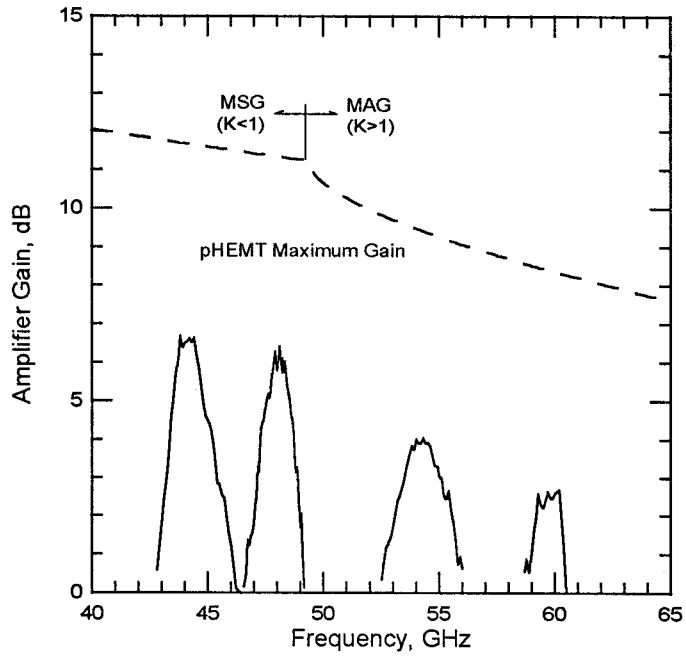

Fig. 4.27. Tuning range of the amplifier. The 60 GHz curve includes an output tuner. The MSG/MAG was calculated assuming a g_m of 43 mS and an excess source inductance of 7 pH.

References

[1] C.F. Jou, W.W. Lam, H. Chen, K. Stolt, N.C. Luhmann, Jr., D.B. Rutledge, "Millimeter-Wave Monolithic Schottky Diode-Grid Frequency Doubler," *IEEE Trans. Microwave Theory Tech.*, vol. 36, pp. 1507–1514, Nov. 1988.

[2] H-.X.L. Liu, L.B. Sjogren, C.W. Domier, N.C. Luhmann, Jr., D.L. Sivco, A.Y. Cho, "Monolithic Quasi-Optical Frequency Tripler Array with 5-W Output Power at 99 GHz," *IEEE Electron Device Lett.*, vol. 14, pp. 329–331, July 1993.

[3] J.-C. Chiao, A. Markelz, Y. Li, J. Hacker, T. Crowe, J. Allen, D.B. Rutledge, "Terahertz Grid Frequency Doublers," presented at *The 6th Int. Symp. Space Terahertz Tech.*, March 1995.

[4] W.W. Lam, H.Z. Chen, K.S. Stolt, C.F. Jou, N.C. Luhmann, Jr., D.B. Rutledge, "Millimeter-Wave Diode Grid Phase Shifters," *IEEE Trans. Microwave Theory Tech.*, vol. 36, pp. 902–907, May 1988.

[5] L.B. Sjogren, H.-X.L. Liu, X.-H. Qin, C.W. Domier, N.C. Luhmann, Jr., "Phased Array Operation of a Diode Grid Impedance Surface," *IEEE Trans. Microwave Theory Tech.*, vol. 42, pp. 565–572, April 1994.

[6] Z.B. Popović, R.M. Weikle, M. Kim, D.B. Rutledge, "A 100-MESFET Planar Grid Oscillator," *IEEE Trans. Microwave Theory Tech.*, vol. 39, pp. 193–200, March 1990.

[7] R.M. Weikle, M. Kim, J.B. Hacker, M.P. De Lisio, D.B. Rutledge, "Planar MESFET Grid Oscillators Using Gate Feedback," *IEEE Trans. Microwave Theory Tech.*, vol. 40, pp. 1997–2003, Nov. 1992.

[8] J.B. Hacker, M.P. De Lisio, M. Kim, C.-M. Liu, S.-J. Li, S.W. Wedge, D.B. Rutledge, "A 10-Watt X-Band Grid Oscillator," *1994 IEEE MTT-S Int. Microwave Symp. Dig.*, pp. 823–826, 1994.

[9] M. Kim, J.J. Rosenberg, R.P. Smith, R.M. Weikle, J.B. Hacker, M.P. DeLisio, D.B. Rutledge, "A Grid Amplifier," *IEEE Microwave Guided Wave Lett.*, vol. 1, pp. 322–324, Nov. 1991.

[10] M. Kim, E.A. Sovero, J.B. Hacker, M.P. DeLisio, J.-C. Chiao, S.-J. Li, D.R. Gagnon, J.J. Rosenberg, D.B. Rutledge, "A 100-Element HBT Grid Amplifier," *IEEE Trans. Microwave Theory Tech.*, vol. 41, pp. 1762–1771, Oct. 1993.

[11] M.P. DeLisio, S.W. Duncan, D.-W. Tu, C.-M. Liu, A. Moussessian, J.J. Rosenberg, D.B. Rutledge, "Modelling and Performance of a 100-Element pHEMT Grid Amplifier," submitted to *IEEE Trans. Microwave Theory Tech.*, April 1995.

[12] D.W. Griffin, "Monolithic Active Array Limitations Due to Substrate Modes," *1995 IEEE AP-S Int. Symp. Dig.*, pp. 1300–1303, 1995.

[13] M. Kim, E.A. Sovero, R.M. Weikle, J.B. Hacker, M.P. DeLisio, D.B. Rutledge, "A 35 GHz Monolithic Grid Oscillator," *17th Int. Conf. Infrared Millimeter Waves Dig.*, pp. 402–403, 1992.

[14] J.A. Higgins, E.A. Sovero, W.J. Ho, "44-GHz Monolithic Plane Wave Amplifiers," *IEEE Microwave Guided Wave Lett.*, vol. 5, pp. 347–348, Oct. 1995.

[15] E.A. Sovero, Y. Kwon, D.S. Deakin, A.L. Sailer, J.A. Higgins, "A PHEMT Based Monolithic Plane Wave Amplifier for 42 GHz," submitted to *1996 IEEE MTT-S Int. Microwave Symp.*, 1995.

[16] C.-M. Liu, E.A. Sovero, W.J. Ho, J.A. Higgins, M.P. DeLisio, D.B. Rutledge, "Monolithic 40-GHz 670-mW HBT Grid Amplifier," submitted to *1996 IEEE MTT-S Int. Microwave Symp.*, Oct. 1995.

[17] M.P. DeLisio, S.W. Duncan, D.-W. Tu, S. Weinreb, C.-M. Liu, D.B. Rutledge, "A 44-60 GHz Monolithic pHEMT Grid Amplifier," submitted to *1996 IEEE MTT-S Int. Microwave Symp.*, Oct. 1995.

[18] D.-W. Tu, S.W. Duncan, A. Eskandarian, B. Golja, B.C. Kane, S.P. Svenson, S. Weinreb, N.E. Byer, "High Gain Monolithic W-Band Low Noise Amplifiers Based on Pseudomorphic High Electron Mobility Transistors," *IEEE Trans. Microwave Theory Tech.*, vol. 42, pp. 2590–2597, Dec. 1994.

[19] J.D. Kraus, *Antennas*, second ed., McGraw-Hill Book Co., New York, 1988, pp. 48–61.

[20] "HP 85180A High Frequency Structure Simulator," Hewlett-Packard, Networks Measurements Division, Santa Rosa, CA.

Chapter 5

Discussion and Suggestions for Future Work

The past five years have been an exciting time for quasi-optical power combining. In the past, only a handful of academic groups were investigating quasi-optics. At the *1991 IEEE International Microwave Symposium*, a few papers dealing with this new field were given in a session primarily reserved for traditional phased array antennas [1]. Today, many groups at research institutions around the world are actively pursuing various quasi-optical projects. In addition, major government and industrial efforts are underway. The past two Microwave Symposia have each had two full sessions dedicated to quasi-optics [2,3], as well as several workshops. A special issue of the *IEEE Transactions on Microwave Theory and Techniques* was devoted to quasi-optical techniques in 1993 [4]. A 100-MESFET oscillator grid [5] won the 1993 Microwave Prize, awarded by the IEEE Microwaves Society to the paper "judged to be the most significant contribution in the field." Chapters on grid arrays have been published in a book [6]; another text solely dedicated to quasi-optics is currently being planned. Five years ago, most quasi-optical power combiners were low-power proof-of-concept experiments. Quasi-optical amplifiers had not yet been demonstrated. Since then, Watt-level quasi-optical power combining has been demonstrated [7,8,11]. The first quasi-optical amplifier grids have been developed [9,10], ultimately leading to several millimeter-wave monolithic amplifier arrays [12–15], with many more being planned.

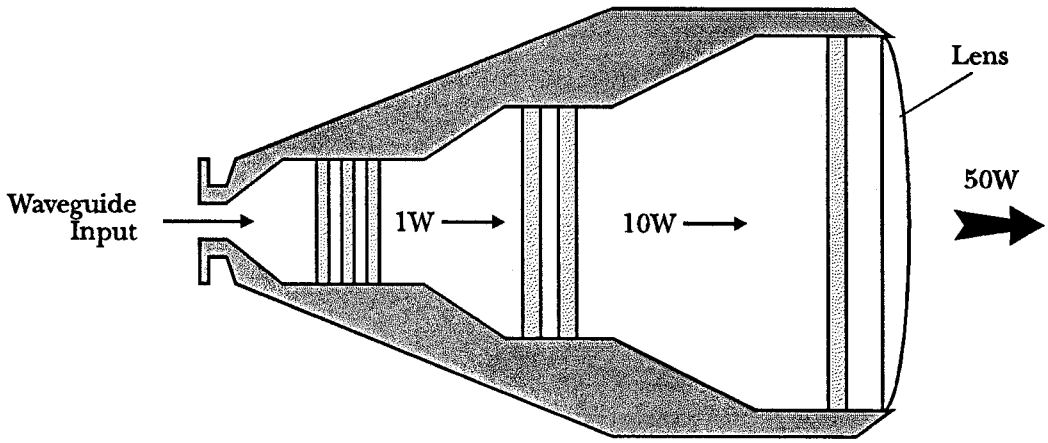

Fig. 5.1. Proposed 50-W quasi-optical TWT replacement using six amplifier arrays.

The promise of quasi-optics has always been large-scale power combining of solid-state millimeter-wave sources. The goal would be a long-awaited Travelling Wave Tube (TWT) replacement, like the one shown in Fig. 5.1. Many pieces of the puzzle have already been found. Large-scale power combining has been demonstrated in hybrid arrays [7,8,11]. Monolithic amplifier arrays have demonstrated gain at millimeter-wave frequencies [12–15]. A hard-horn feed system has been developed and shown to effectively confine the radiated beam, resulting in a system with real flange-to-flange power gain [16].

Many questions remain unanswered. In order to be able to confidently design grids, more extensive electromagnetic modelling is required. Thermal modelling is also a huge concern. Multiple-element quasi-optical systems are just now being explored. Predicting future trends is never easy. At this point, however, it seems safe to say that with the level of academic, industrial, and government involvement, the potential of quasi-optics may soon be fulfilled.

References

[1] *1991 IEEE MTT-S Int. Microwave Symp. Dig.*, session OO, 1991.

[2] *1994 IEEE MTT-S Int. Microwave Symp. Dig.*, sessions WE3B and WE4B, 1994.

[3] *1995 IEEE MTT-S Int. Microwave Symp. Dig.*, sessions WE3B and WE4B, 1995.

[4] *IEEE Trans. Microwave Theory Tech.*, special issue on quasi-optical techniques, vol. 41, Oct. 1993.

[5] Z.B. Popović, R.M. Weikle, M. Kim, D.B. Rutledge, "A 100-MESFET Planar Grid Oscillator," *IEEE Trans. Microwave Theory Tech.*, vol. 39, pp. 193–200, March 1990.

[6] *Frequency Selective Surface and Grid Array*, T.K. Wu, ed., John Wiley & Sons, Inc., New York, 1995.

[7] J.B. Hacker, M.P. DeLisio, M. Kim, C.-M. Liu, S.-J. Li, S.W. Wedge, D.B. Rutledge, "A 10-Watt X-Band Grid Oscillator," *1994 IEEE MTT-S Int. Microwave Symp. Dig.*, pp. 823–826, 1994.

[8] P. Liao, R.A. York, "A High Power Two-Dimensional Coupled-Oscillator Array at X-band," *1995 IEEE MTT-S Int. Microwave Symp. Dig.*, pp. 909–912, 1995.

[9] M. Kim, J.J. Rosenberg, R.P. Smith, R.M. Weikle, J.B. Hacker, M.P. DeLisio, D.B. Rutledge, "A Grid Amplifier," *IEEE Microwave Guided Wave Lett.*, vol. 1, pp. 322–324, Nov. 1991.

[10] M. Kim, E.A. Sovero, J.B. Hacker, M.P. DeLisio, J.-C. Chiao, S.-J. Li, D.R. Gagnon, J.J. Rosenberg, D.B. Rutledge, "A 100-Element HBT Grid Amplifier," *IEEE Trans. Microwave Theory Tech.*, vol. 41, pp. 1762–1771, Oct. 1993.

[11] M.P. De Lisio, S.W. Duncan, D.-W. Tu, C.-M. Liu, A. Moussessian, J.J. Rosenberg, D.B. Rutledge, "Modelling and Performance of a 100-Element pHEMT Grid Amplifier," submitted to *IEEE Trans. Microwave Theory Tech.*, April 1995.

[12] J.A. Higgins, E.A. Sovero, W.J. Ho, "44-GHz Monolithic Plane Wave Amplifiers," *IEEE Microwave Guided Wave Lett.*, vol. 5, pp. 347–348, Oct. 1995.

[13] E.A. Sovero, Y. Kwon, D.S. Deakin, A.L. Sailer, J.A. Higgins, "A PHEMT Based Monolithic Plane Wave Amplifier for 42 GHz," submitted to *1996 IEEE MTT-S Int. Microwave Symp.*, 1995.

[14] C.-M. Liu, E.A. Sovero, W.J. Ho, J.A. Higgins, M.P. De Lisio, D.B. Rutledge, "Monolithic 40-GHz 670-mW HBT Grid Amplifier," submitted to *1996 IEEE MTT-S Int. Microwave Symp.*, Oct. 1995.

[15] M.P. De Lisio, S.W. Duncan, D.-W. Tu, S. Weinreb, C.-M. Liu, D.B. Rutledge, "A 44-60 GHz Monolithic pHEMT Grid Amplifier," submitted to *1996 IEEE MTT-S Int. Microwave Symp.*, Oct. 1995.

[16] T. Ivanov, A. Mortazawi, "A Two Stage Spatial Amplifier With Hard Horn Feeds," accepted to *IEEE Microwave Guided Wave Lett.*, 1995.

Appendix A

Modelling of Periodic Structures

This appendix discusses the technique used throughout this thesis to model the two-dimensional periodic grid structure. This method is a refinement of the very elegant technique developed by Robert Weikle at Caltech [1]. Weikle's method begins by assuming a simple, yet plausible, surface current distribution on the conducting surfaces of the array. Next, the induced emf technique is used to determine the driving-point impedance of the structure. The approach presented here uses the method of moments to better approximate the surface current distribution, resulting in a more accurate solution for the impedance.

This approach is by no means original. Periodic structures, and the intimately related problem of obstacles in metal waveguides, have been extensively studied since the 1940's [2,3]. In 1967, Harrington developed the modern method of moments, a powerful matrix technique useful for solving a variety of electromagnetic problems on a digital computer [4,5]. This method was soon applied to the study of periodic structures and waveguide obstacles [6–10]. Even today, with the advent of extremely fast computers, these problems remain to be the subjects of active ongoing research [11–16].

A.1. Discussion of the Method

Many of the grids analyzed in this thesis are quite similar to the grating structure shown in Fig. A.1. The grating is a two-dimensional infinite array of thin metallic strips of width $2w$ and spaced a uniform distance $2a$ apart. This

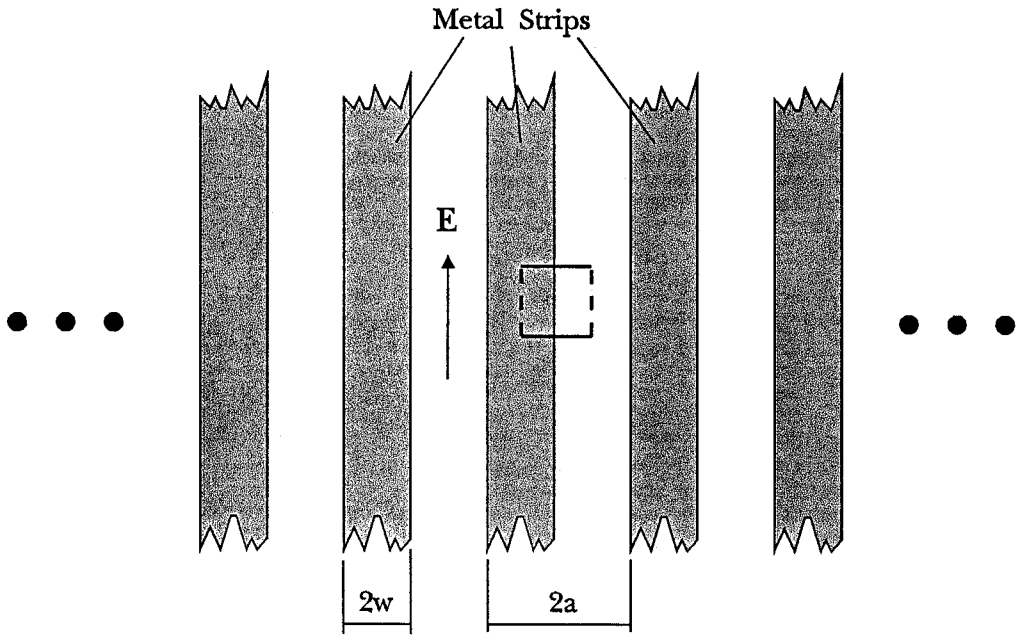

Fig. A.1. The metal-strip grating. A unit cell for the array can be defined, exploiting the symmetry of the structure.

structure is illuminated by a normally incident plane wave, with the electric field polarized along the direction of the strips. The goal of the problem is to determine the impedance this grating presents to the incident wave.

The problem can be simplified by taking advantage of the symmetry of the structure. Following the approach in [1], we define certain symmetry planes where the tangential electric and magnetic fields will vanish. This reduces the problem of the infinite grating to an obstacle in an equivalent waveguide, as shown in Fig. A.2. The waveguide consists of electric walls on the top and bottom, and magnetic walls on the sides. The waveguide extends in the $\pm z$-direction, with the metal strip located at $z = 0$. We assume that only the TEM waveguide mode propagates. The only other modes this structure will excite are TE_{n0} modes; these higher-order modes are assumed to be evanescent. The incident field excites a y-directed surface current in the strip. We are interested in finding this surface current and the resulting scattered field.

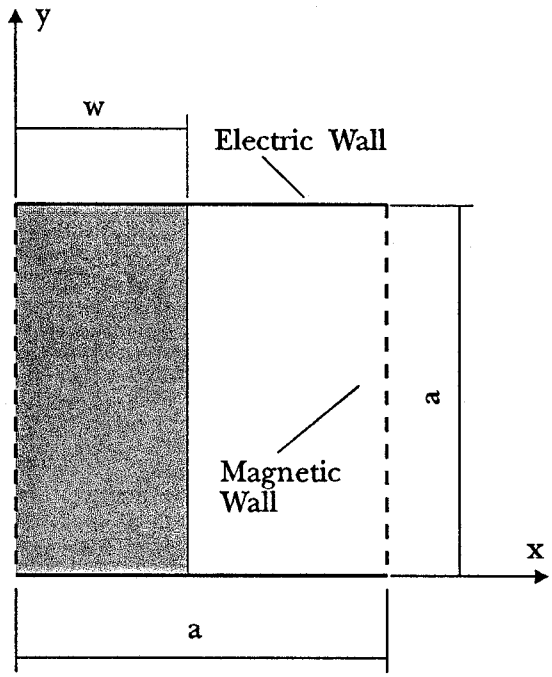

Fig. A.2. The unit cell for the inductive grating. The cell is bounded by electric walls on the top and bottom, and magnetic walls on the sides.

At $z = 0$, we can express the surface current $K_y(x)$ and scattered E-field $E_y^s(x)$ in terms of the waveguide modes:

$$K_y(x) = K_o + \sum_{n=1}^{\infty} K_n \cos\left(\frac{n\pi x}{a}\right) \tag{A.1}$$

$$E_y^s(x) = E_o^s + \sum_{n=1}^{\infty} E_n^s \cos\left(\frac{n\pi x}{a}\right). \tag{A.2}$$

The symmetry of the problem demands that there be no y-variation in the fields. For a given surface current distribution $K_y(x)$, the coefficients K_n can be determined using the orthogonal property of the cosine function:

$$K_o = \frac{1}{a}\int_0^a K_y(x)\,dx \tag{A.3}$$

$$K_n = \frac{2}{a}\int_0^a K_y(x)\cos\left(\frac{n\pi x}{a}\right)\,dx. \tag{A.4}$$

The electric field E_y must be continuous. The magnetic field H_x, however, will be discontinuous at $z = 0$ due to the surface current K_y. This can be written using Maxwell's boundary conditions:

$$K_y(x) = H_x^+(x) - H_x^-(x), \tag{A.5}$$

where the $+$ and $-$ superscripts denote the H-field at $z = 0^+$ and $z = 0^-$. The H-fields are related to the E-field through the modal impedances:

$$H_x^+ = -\frac{E_o^s}{Z^{TEM+}} - \sum_{n=1}^{\infty}\frac{E_n^s}{Z_n^{TE+}}\cos\left(\frac{n\pi x}{a}\right) \tag{A.6}$$

$$H_x^- = \frac{E_o^s}{Z^{TEM-}} + \sum_{n=1}^{\infty}\frac{E_n^s}{Z_n^{TE-}}\cos\left(\frac{n\pi x}{a}\right), \tag{A.7}$$

where $Z^{TEM\pm}$ is the impedance of the TEM mode looking in the $+z$ or $-z$-direction. Similarly, Z_n^{TE} represents the impedance of the TE_{n0} mode, looking in the appropriate direction. This keeps the problem fairly general; substrates and mirrors placed in front or behind the grating can be accommodated through these modal impedances. The expressions can be combined to give the electric field at $z = 0$ in terms of the surface current:

$$E_y^s(x) = -K_o(Z^{TEM+}||Z^{TEM-}) - \sum_{n=1}^{\infty}K_n(Z_n^{TE+}||Z_n^{TE-})\cos\left(\frac{n\pi x}{a}\right), \tag{A.8}$$

where the $||$ denotes the parallel combination of the two impedances.

Often, it is convenient to consider the response of a system to an impulse excitation. We assume the surface current is a delta function at $x = x'$:

$$K_y(x) = \delta(x - x'). \tag{A.9}$$

The E-field at $z = 0$ is given by $(A.8)$, using $(A.3)$ and $(A.4)$ to solve for the K_n coefficients:

$$\begin{aligned} G_E^s(x,x') = &-\frac{1}{a}(Z^{TEM+}||Z^{TEM-}) \\ &-\frac{2}{a}\sum_{n=1}^{\infty}(Z_n^{TE+}||Z_n^{TE-})\cos\left(\frac{n\pi x}{a}\right)\cos\left(\frac{n\pi x'}{a}\right), \end{aligned} \tag{A.10}$$

This function $G_E^s(x,x')$ is known as the Green's function for the problem.

Weikle [1] now proceeds by assuming a simple surface current distribution $K_y(x)$ on the strip. The new approach uses the method of moments to obtain a more exact estimate for $K_y(x)$. We break the metallic strip up into M subsectional basis functions. We can expand $K_y(x)$ in terms of these basis functions:

$$K_y(x) = \sum_{m=1}^{M} k_m f_m(x). \tag{A.11}$$

The basis functions $f_m(x)$ are simple pulses of width w/M:

$$f_m(x) = \begin{cases} 1 & |x - x_m| \leq w/(2M) \\ 0 & \text{else,} \end{cases} \tag{A.12}$$

where x_m is the center point of the basis:

$$x_m = \frac{w}{M}\left(m - \frac{1}{2}\right) \qquad m = 1, \ldots, M. \tag{A.13}$$

The scattered field is then given by:

$$E_y^s(x) = \sum_{m=1}^{M} k_m \int_0^a G_E^s(x,x') f_m(x')\, dx'. \tag{A.14}$$

The total field $E_y(x)$ must vanish on the conducting strip. The total field is the sum of the incident field $E_y^i(x)$ and the scattered field $E_y^s(x)$:

$$E_y(x) = E_y^i(x) + E_y^s(x) = 0 \qquad 0 \leq x \leq w. \tag{A.15}$$

The incident field is in the form of a plane wave, and therefore has no x-variation. For convenience we give it a unit strength. This implies:

$$-E_y^s(x) = E_y^i(x) = 1 \qquad 0 \leq x \leq w. \tag{A.16}$$

The point-matching technique evaluates $-E_y^s(x)$ at the M points on the strip x_1 through x_M, resulting in:

$$-E_y^s(x_l) = -\sum_{m=1}^{M} k_m \int_0^a G_E^s(x_l,x') f_m(x')\, dx' \qquad l = 1, \ldots, M. \tag{A.17}$$

This can be expressed as a matrix equation:

$$[g_{lm}][k_m] = [u], \tag{A.18}$$

where $[u]$ is a unit vector and $g_{lm} = -E_y^s(x_l)$. For the problem at hand, g_{lm} is given by:

$$\begin{aligned} g_{lm} =& \frac{w}{Ma}(Z^{TEM+}||Z^{TEM-}) \\ &+ \sum_{n=1}^{\infty} \frac{4}{n\pi}(Z_n^{TE+}||Z_n^{TE-}) \cos\left(\frac{n\pi x_l}{a}\right) \cos\left(\frac{n\pi x_m}{a}\right) \sin\left(\frac{n\pi w}{2Ma}\right). \end{aligned} \tag{A.19}$$

The matrix equation $(A.18)$ is now inverted to solve for $[k_m]$. We now have an estimate for the actual surface current distribution. Generally speaking, the larger the number of bases M, the more accurate the estimate. The computation time, however, will become longer with increasing M. This is not only due to the matrix $[g_{lm}]$ becoming larger, but also due to the fact that more waveguide modes must be summed in $(A.19)$ to insure convergence for the narrower pulse function.

We are now in a position to use the induced emf technique to determine the impedance the grating presents to the incident wave. This, in effect, will determine the reflected field. While it is true that the reflected field could be found directly using $(A.14)$, the induced emf technique is stationary with respect to variations in the current distribution $K_y(x)$ [1,17]. The impedance calculated using this technique is therefore more forgiving to inaccuracies in the estimate for the current distribution. The induced emf method is based on the conservation of complex power, and can be expressed as:

$$Z = -\frac{1}{|I|^2} \int_S \mathbf{E} \cdot \mathbf{K}^* \, dS, \tag{A.20}$$

where I is the current in the strip and the integration is performed over the square unit cell at $z = 0$. For the problem at hand, this becomes:

$$Z = (Z^{TEM+}||Z^{TEM-}) + \frac{1}{2|K_o|^2} \sum_{n=1}^{\infty} |K_n|^2 (Z_n^{TE+}||Z_n^{TE-}), \tag{A.21}$$

where the K coefficients are given by:

$$K_o = \frac{I}{a} = \frac{w}{Ma} \sum_{m=1}^{M} k_m \tag{A.22}$$

$$K_n = \frac{4}{n\pi} \sin\left(\frac{n\pi w}{2Ma}\right) \sum_{m=1}^{M} k_m \cos\left(\frac{m\pi x_m}{a}\right). \tag{A.23}$$

One of our original assumptions was that the TEM mode is the only propagating mode. The impedances of the evanescent TE modes are primarily inductive, which gives an equivalent circuit model for the grating shown in Fig. A.3. The TEM impedances are represented by transmission lines, and the coupling to the TE modes is modelled by the inductance jX. If the frequency is high enough, the TE modes will begin to propagate, with real mode impedances. In this case, in series with the inductance will be a resistance R. Power lost in this resistor represents energy scattered into the higher-order grating lobes of the structure.

This technique was used to model the radiating leads of the tunnel diode grid oscillator, the input and output leads of the amplifier grids, and the inductance of the metal-strip polarizers. These structures are similar enough to the inductive grating to warrant the simpler grating analysis. The approach, however, can be generalized to accommodate more complicated grid structures with both x and y-variation.

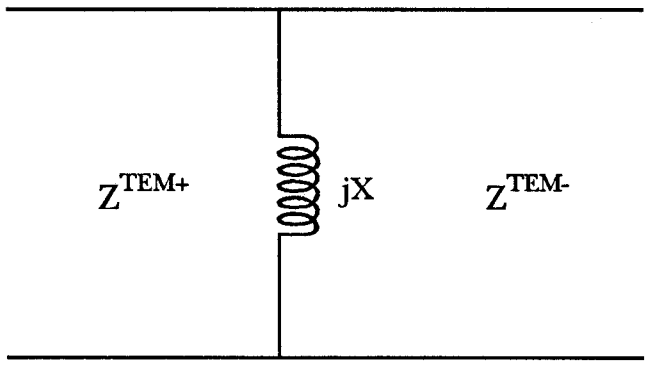

Fig. A.3. Equivalent circuit model for the inductive grating.

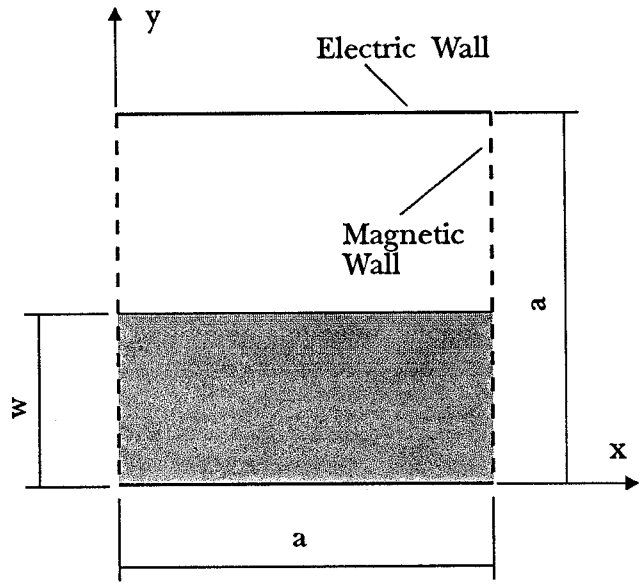

Fig. A.4. The unit cell for the capacitive grating.

A similar technique is used to model the response when the incident field is polarized orthogonal to the metal strips. This structure will have an impedance that is primarily capacitive. The unit cell for the capacitive grating is shown in Fig. A.4. The approach follows along the same lines as the inductive grating; only the differences will be highlighted here.

In this case, the surface current and electric field will have only a y-variation, and can be expressed in terms of the TM_{0n} modes of the waveguide:

$$K_y(y) = K_o + \sum_{n=1}^{\infty} K_n \cos\left(\frac{n\pi y}{a}\right) \tag{A.24}$$

$$E_y^s(y) = E_o^s + \sum_{n=1}^{\infty} E_n^s \cos\left(\frac{n\pi y}{a}\right). \tag{A.25}$$

The Green's function is:

$$G_E^s(y,y') = -\frac{1}{a}(Z^{TEM+}||Z^{TEM-}) \\ -\frac{2}{a}\sum_{n=1}^{\infty}(Z_n^{TM+}||Z_n^{TM-})\cos\left(\frac{n\pi y}{a}\right)\cos\left(\frac{n\pi y'}{a}\right). \tag{A.26}$$

As before, we expand the surface current in terms of basis functions:

$$K_y(y) = \sum_{m=1}^{M} k_m f_m(y). \tag{A.27}$$

We use overlapping raised cosine functions as the basis to insure convergence:

$$f_m(y) = \begin{cases} \cos^2\left(\frac{\pi(y-y_m)M}{2w}\right) & |y-y_m| \le w/M \\ 0 & \text{else,} \end{cases} \tag{A.28}$$

where y_m is the center point of the basis:

$$y_m = \frac{w}{M}(m-1) \qquad m = 1,\ldots,M. \tag{A.29}$$

The result is a matrix equation identical to $(A.18)$, with the matrix elements g_{lm} given by:

$$g_{lm} = -\int_0^a G_E^s(y_l,y')f_m(y')\,dy'. \tag{A.30}$$

We then solve for the current vector $[k_m]$, and use the induced emf technique to solve for the impedance:

$$Z = (Z^{TEM+}||Z^{TEM-}) + \frac{1}{2|K_o|^2}\sum_{n=1}^{\infty}|K_n|^2(Z_n^{TM+}||Z_n^{TM-}), \tag{A.31}$$

where

$$K_o = \frac{1}{a}\sum_{m=1}^{\infty}k_m\int_0^a f_m(y)\,dy \tag{A.32}$$

$$K_n = \frac{2}{a}\sum_{m=1}^{\infty}k_m\int_0^a f_m(y)\cos\left(\frac{n\pi y}{a}\right)\,dy. \tag{A.33}$$

This technique was used to model the capacitive polarizers in the grid amplifier circuits, as well as the metal mesh couplers reported in [18,19].

A.2. Discussion of the Results

A convenient grating to analyze in order to test that the method is working correctly is the very special case of a semi-iris. This means that the metal strip width $2w$ is exactly one-half of the strip spacing $2a$. For this special case only, the impedance can be written exactly. Collin [20] solves the problem through a clever integration in the complex plane. The solution for the reactance X_C of a capacitive semi-iris is written as a converging series:

$$\frac{\eta_o}{X_C} = -2\tan\left[\sum_{n=1}^{\infty}\sin^{-1}\left(\frac{a/\lambda_o}{n-\frac{1}{2}}\right) - \sin^{-1}\left(\frac{a/\lambda_o}{n}\right)\right], \qquad (A.34)$$

where λ_o is the free-space wavelength, and η_o is the characteristic impedance of free-space:

$$\eta_o = \sqrt{\frac{\mu_o}{\varepsilon_o}}. \qquad (A.35)$$

The grating is suspended in mid-air, without any dielectrics. The reactance for an inductive semi-iris X_L can be determined from X_C using Booker's relation:

$$X_L X_C = -\frac{\eta_o^2}{4} \qquad (A.36)$$

Table A.1 compares the reactances for a semi-iris obtained using Weikle's method [1] and the Method of Moments (MoM) to Collin's exact solution. For this problem, a is 5 mm, w is 2.5 mm, and the frequency is 10 GHz. For a grating suspended in free space, the modal impedances are given by:

$$Z^{TEM+} = Z^{TEM-} = \eta_o \qquad (A.37)$$

$$Z^{TE+} = Z^{TE-} = \frac{j\eta_o}{\sqrt{\left(\frac{n\lambda_o}{2a}\right)^2 - 1}} \qquad (A.38)$$

$$Z^{TM+} = Z^{TM-} = -j\eta_o\sqrt{\left(\frac{n\lambda_o}{2a}\right)^2 - 1}. \qquad (A.39)$$

Method	X_L, Ω	% error	X_C, Ω	% error
Exact [20]	45.5	0	–779.5	0
Weikle [1]	56.7	24.6	–626.0	–19.7
MoM, 5 elements	47.9	5.3	–869.6	11.6
MoM, 10 elements	46.7	2.6	–825.5	5.9
MoM, 20 elements	46.1	1.3	–803.3	3.1
MoM, 50 elements	45.8	0.7	–789.5	1.3

Table A.1. Comparison of the inductive and capacitive reactances for the semi-iris.

Weikle's method is accurate to 20% for the capacitive case and 25% for the inductive iris. The moment method is accurate to within 6% using only 10 elements. When 50 elements are used, this method is accurate to 2%. The results for the inductive semi-iris are more accurate than those for the capacitive iris. This is most likely due to the different basis functions used in the two cases.

Fig. A.5 shows the current distribution on the inductive semi-iris as a function of position. The surface current distribution quickly converges as the number of elements used in the moment method increases. The familiar singularity at the edge of the strip is evident. Fig. A.6 shows the current distribution of the capacitive semi-iris. The current goes to zero at the edge of the strip. The distribution converges more slowly than the inductive case, again probably due to the different basis functions.

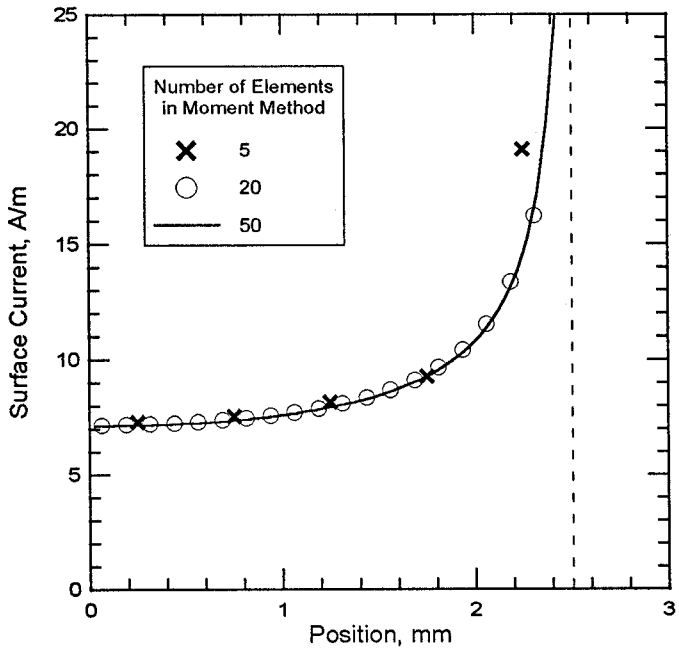

Fig. A.5. Surface current distribution for the inductive semi-iris.

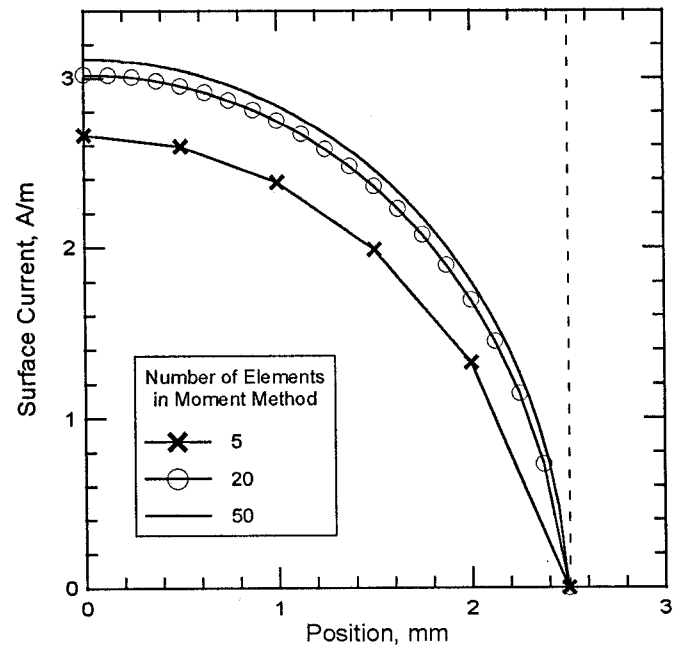

Fig. A.6. Surface current distribution for the capacitive semi-iris.

References

[1] R.M. Weikle, "Quasi-Optical Planar Grids for Microwave and Millimeter-Wave Power Combining," Ph.D. Thesis, California Institute of Technology, Pasadena, CA, 1992.

[2] N. Marcuvitz, *Waveguide Handbook*, Peter Peregrinus Ltd. on behalf of IEE Press, London, 1986. Previously published as part of the MIT Radiation Laboratory Series, McGraw-Hill, 1948.

[3] J. Schwinger, D. Saxon, *Discontinuities in Waveguides*, Gordon and Breach Science Publishers, 1968. Originally circulated as unpublished notes in the 1940's.

[4] R.F. Harrington, "Matrix Methods for Field Problems," *Proc. IEEE*, vol. 55, pp. 136–149, Feb. 1967.

[5] R.F. Harrington, *Field Computation by Moment Methods*, IEEE Press, New York, 1993. Originally published by Macmillan Publishing Co., 1968.

[6] R.H. Ott, R.G. Kouyoumijian, L. Peters, "Scattering by a Two-Dimensional Periodic Array of Narrow Plates," *Radio Science*, vol. 2, pp. 1347–1349, Nov. 1967.

[7] C.-C. Chen, "Transmission Through a Conducting Screen Perforated Periodically with Apertures," *IEEE Trans. Microwave Theory Tech.*, vol. 18, pp. 627–632, Sept. 1970.

[8] C.-C. Chen, "Scattering by a Two-Dimensional Periodic Array of Conducting Plates," *IEEE Trans. Antennas Propagation*, vol. 18, pp. 660–665, Sept. 1970.

[9] R.L. Eisenhart, P.J. Khan, "Theoretical and Experimental Analysis of a Waveguide Mounting Structure," *IEEE Trans. Microwave Theory Tech.*, vol. 19, pp. 706–719, Aug. 1971.

[10] J.P. Montgomery, "Scattering by an Infinite Periodic Array of Thin Conductors on a Dielectric Sheet," *IEEE Trans. Antennas Propagation*, vol. 23, pp. 70–75, Jan. 1975.

[11] S.D. Gedney, J.F. Lee, R. Mittra, "A Combined FEM/MoM Approach to Analyze the Plane Wave Diffraction by Arbitrary Gratings," *IEEE Trans. Microwave Theory Tech.*, vol. 40, pp. 363–370, Feb 1992.

[12] W.-J. Tsay, D.M. Pozar, "Application of the FDTD Technique to Periodic Problems in Scattering and Radiation," *IEEE Microwave Guided Wave Lett.*, vol. 3, pp. 250–252, Aug. 1993.

[13] A.M. Lerer, A.G. Schuchinsky, "Full-Wave Analysis of Three-Dimensional Planar Structures," *IEEE Trans. Microwave Theory Tech.*, vol. 41, pp. 2002–2015, Nov. 1993.

[14] A.E. Sheiman, "A New Method for Solving Irises in Waveguides," Ph.D. Thesis, California Institute of Technology, Pasadena, CA, 1993.

[15] S.C. Bundy, Z.B. Popović, "A Generalized Analysis for Grid Oscillator Design," *IEEE Trans. Microwave Theory Tech.*, vol. 42, pp. 2486–2491, Dec. 1994.

[16] *Frequency Selective Surface and Grid Array*, T.K. Wu, ed., John Wiley & Sons, Inc., New York, 1995.

[17] R.H. Harrington, *Time-Harmonic Electromagnetic Fields*, McGraw-Hill, Inc., New York, 1961, pp. 348–355.

[18] J. Bae, J.-C. Chiao, K. Mizuno, D.B. Rutledge, "Metal Mesh Couplers Using Optical Tunneling Effect at Millimeter and Submillimeter Wavelengths," *1994 IEEE MTT-S Int. Microwave Symp. Dig.*, pp. 787–790, 1994.

[19] J. Bae, J.-C. Chiao, K. Mizuno, D.B. Rutledge, "Metal Mesh Couplers Using Evanescent Waves at Millimeter and Submillimeter Wavelengths," *1995 IEEE MTT-S Int. Microwave Symp. Dig.*, pp. 597–600, 1995.

[20] R.E. Collin, *Field Theory of Guided Waves*, second ed., IEEE Press, New York, 1991, p. 694.

Appendix B

Thermal Modelling

This appendix will discuss techniques useful for modelling the thermal behavior of grid arrays. Any electronic design where high powers are dissipated requires a careful thermal analysis to avoid destroying or shortening the lifetime of the solid-state devices. This is especially true for large, high-power quasi-optical arrays, where the heat may need to be removed in a rather inefficient manner so as not to interfere with the grid's electrical performance. The methods presented here are applicable to amplifier grids, like the ones reported in Chapters 3 and 4, and high power oscillator grids, like the 10 W array built and tested by Jon Hacker at Caltech [1].

B.1. Array with Heat Sinking from the Edges

Consider the grid array mounted as illustrated in Fig. B.1. Heat sinks remove the heat from all four edges. The heat sinks could be a metal frame surrounding the array, or possibly the walls of a waveguide in which the array is mounted. This approach is attractive for an amplifier grid, as the microwave beam must be free to propagate from both the front and back surfaces. The grid is assumed to be square, with length a on a side, and thickness c. A heat flux $\psi_z^o(x,y)$ is added from the top surface. The bottom surface is thermally insulating.

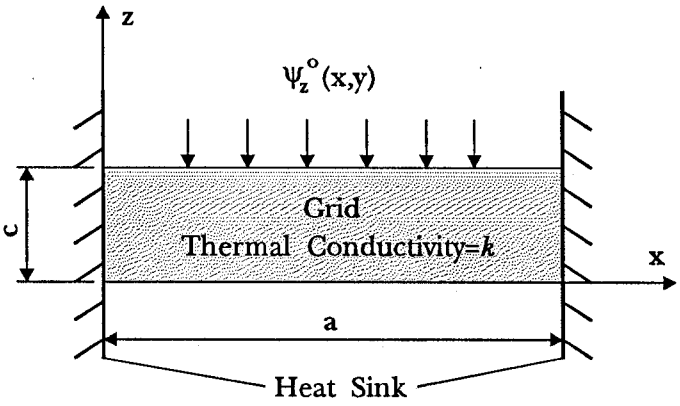

Fig. B.1. Configuration for a grid array with heat removal from the edges.

The steady-state temperature distribution $T(x, y, z)$ in the substrate must satisfy Laplace's equation [2]:

$$\nabla^2 T(x, y, z) = 0. \tag{B.1}$$

The vector heat flux $\vec{\psi}(x, y, z)$ is related to this temperature distribution by the material's thermal conductivity k [2]:

$$\vec{\psi}(x, y, z) = -k\nabla T(x, y, z). \tag{B.2}$$

The following expression is a solution of $(B.1)$ and satisfies the specified boundary conditions:

$$T(x, y, z) = \sum_{m=1}^{\infty}\sum_{n=1}^{\infty} T_{mn} \sin\left(\frac{m\pi x}{a}\right) \sin\left(\frac{n\pi y}{a}\right) \frac{\cosh(\gamma_{mn} z)}{\sinh(\gamma_{mn} c)}, \tag{B.3}$$

where γ_{mn} is given by:

$$\gamma_{mn} = \frac{\pi}{a}\sqrt{m^2 + n^2}. \tag{B.4}$$

The heat flux distribution at the front surface of the array is then:

$$\psi_z^o(x, y) = k\frac{\partial T}{\partial z}\bigg|_{z=c} = k\sum_{m=1}^{\infty}\sum_{n=1}^{\infty} T_{mn}\gamma_{mn} \sin\left(\frac{m\pi x}{a}\right) \sin\left(\frac{n\pi y}{a}\right). \tag{B.5}$$

Solving for T_{mn}, we get:

$$T_{mn} = \frac{4}{ka^2\gamma_{mn}} \int_0^a \int_0^a \psi_z^o(x,y) \sin\left(\frac{m\pi x}{a}\right) \sin\left(\frac{n\pi y}{a}\right) dxdy. \qquad (B.6)$$

For the special case of a unit heat flux uniformly distributed over a square area of dimension w on a side and centered at (x', y'), this becomes:

$$T_{mn} = \frac{4w^2}{ka^2\gamma_{mn}} \sin\left(\frac{m\pi x'}{a}\right) \sin\left(\frac{n\pi y'}{a}\right) \operatorname{sinc}\left(\frac{m\pi w}{2a}\right) \operatorname{sinc}\left(\frac{n\pi w}{2a}\right), \qquad (B.7)$$

where the sinc function is defined as:

$$\operatorname{sinc}\xi = \frac{\sin\xi}{\xi}. \qquad (B.8)$$

For the very special case of a uniform source covering the entire top surface of the array, the thermal resistance (temperature rise per unit power dissipated) can be approximated as:

$$R_{th} \approx \frac{0.29}{ka} \sqrt[2.55]{1 + \left(\frac{0.254a}{c}\right)^{2.55}}. \qquad (B.9)$$

As an example, we will examine an amplifier array similar to the 36-element monolithic grid described in Chapter 4. The size of the monolithic chip a is 4.5 mm on a side, and the thickness c is 0.38 mm. The substrate is GaAs, which has a thermal conductivity k of 46 W/m/°C [3]. Physically, the heat is generated by the transistor pair and bias resistors in each unit cell. We model these as a uniform heat flux through a square area 65 μm on a side, centered in each unit cell. The aggregate flux, then, is a 6×6 array of these sources, spaced 0.52 mm apart. We will assume that each transistor dissipates 50 mW. The entire grid, then, dissipates 3.6 W.

The temperature profile is plotted in Fig. B.2. The plot is a section taken through a central row in the array. Not surprisingly, the devices at the center get the hottest. The peak temperature rise is 44° C. Although for this particular example, the temperature rise is not unreasonably high, this method of heat

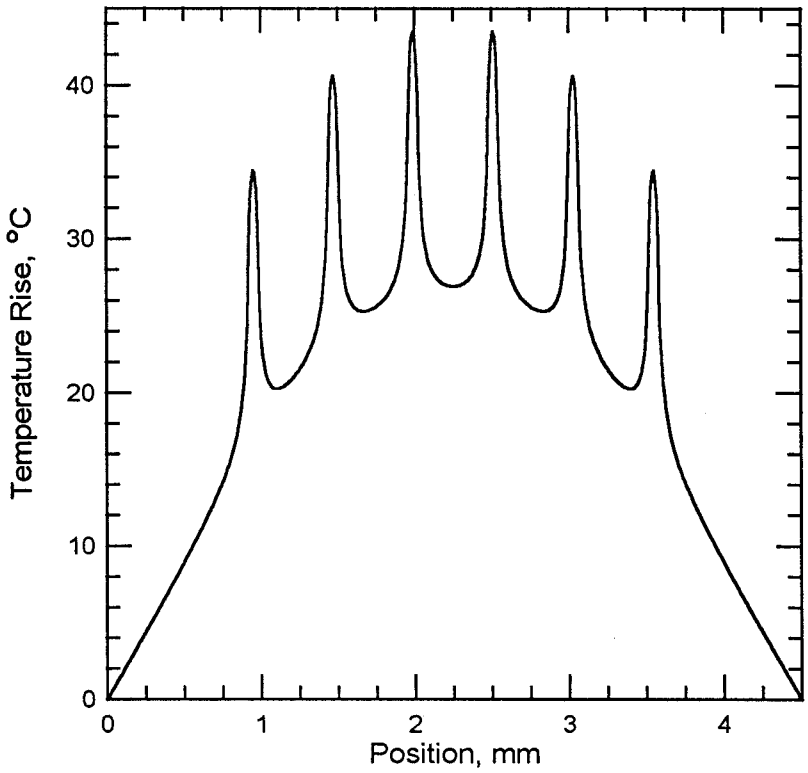

Fig. B.2. Temperature profile for a section through a central row of the array. The peak temperature rise is 44° C, assuming each transistor dissipates 50 mW.

removal is not very efficient. The thin GaAs chip is a relatively poor thermal conductor, especially for the lateral heat flow this configuration demands. Temperature rises for larger arrays using more powerful devices could easily become unacceptable.

B.2. Array with Heat Sinking from the Back

A better configuration is illustrated in Fig. B.3. The grid is mounted on a dielectric carrier, presumably with a high thermal conductivity. The heat is transferred through the grid substrate in the transverse direction, then conducted to the heat sink laterally by the carrier. If this configuration is to be used for a grid amplifier, the carrier should have a low loss tangent, to avoid attenuating the microwave beam. This configuration is also suitable for an array mounted

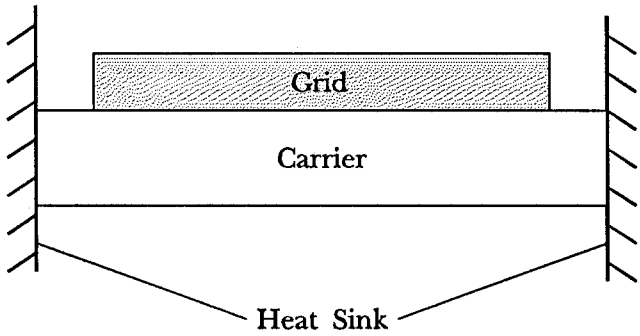

Fig. B.3. A grid mounted on a thermal conducting dielectric carrier.

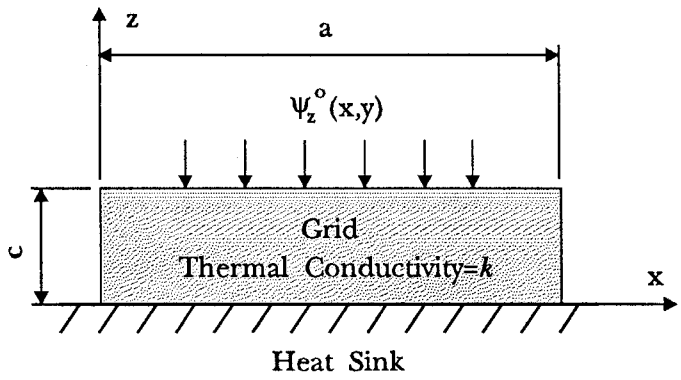

Fig. B.4. Configuration for a grid array with heat removal from the bottom.

directly on a large metal heat sink. Fig. B.4 shows the configuration used for the analysis. Again, the grid is square with length a on a side, and the thickness is c. A heat flux $\psi_z^o(x, y)$ enters the grid from the top, and is removed from the bottom by a perfect heat sink of constant temperature. Modelling the carrier as a perfect heat sink is a good approximation for carriers with high thermal conductivities. All other surfaces are thermally insulating.

The analysis proceeds in a similar manner as before. A temperature distribution that satisfies the boundary conditions is:

$$T(x,y,z) = \frac{T_{00}z}{c} + \sum_{m=0}^{\infty} \sum_{\substack{n=0 \\ n+m\neq 0}}^{\infty} T_{mn}\gamma_{mn} \cos\left(\frac{m\pi x}{a}\right) \cos\left(\frac{n\pi y}{a}\right). \qquad (B.10)$$

The coefficients are computed as before, taking advantage of the orthogonality of the cosine function:

$$T_{00} = \frac{c}{ka^2} \int_0^a \int_0^a \psi_z^o(x,y)\, dxdy \qquad (B.11)$$

$$T_{mn} = \frac{\epsilon_m \epsilon_n}{k\gamma_{mn}a^2} \int_0^a \int_0^a \psi_z^o(x,y) \cos\left(\frac{m\pi x}{a}\right) \cos\left(\frac{n\pi y}{a}\right) dxdy, \qquad (B.12)$$

where ϵ_i is defined by:

$$\epsilon_i = \begin{cases} 1 & i = 0 \\ 2 & \text{else.} \end{cases} \qquad (B.13)$$

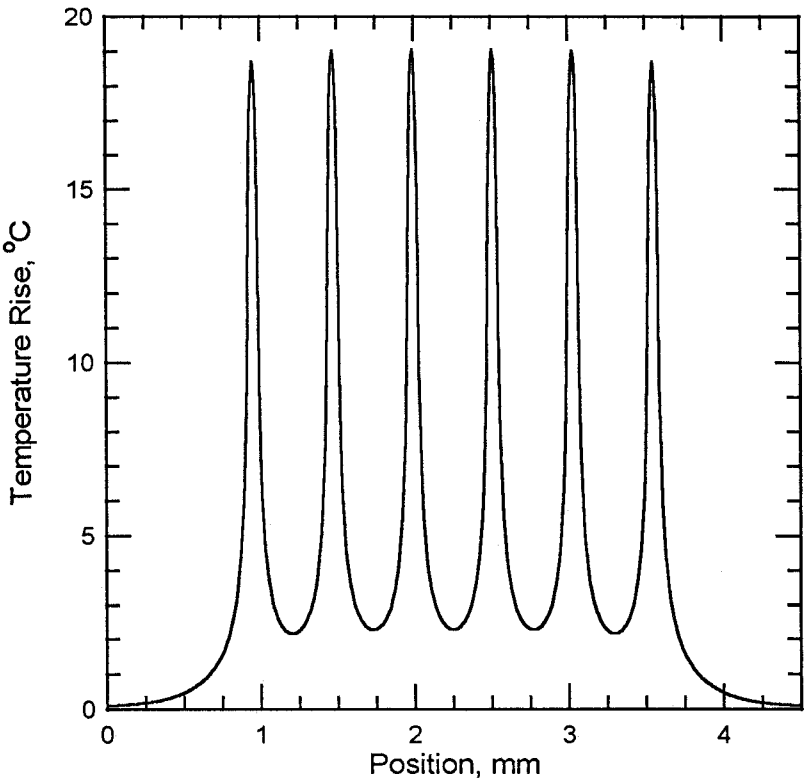

Fig. B.5. Temperature profile for a section through a central row of the array. The peak temperature rise is 19° C, assuming each transistor dissipates 50 mW.

For the special case of a unit heat flux uniformly distributed over a square area of dimension w on a side and centered at (x', y'), this becomes:

$$T_{00} = \frac{cw^2}{ka^2} \tag{B.14}$$

$$T_{mn} = \frac{\epsilon_m \epsilon_n w^2}{k\gamma_{mn} a^2} \cos\left(\frac{m\pi x'}{a}\right) \cos\left(\frac{n\pi y'}{a}\right) \operatorname{sinc}\left(\frac{m\pi w}{2a}\right) \operatorname{sinc}\left(\frac{n\pi w}{2a}\right). \tag{B.15}$$

We consider the same amplifier array example as in the previous section, only with bottom heat sinking. Fig. B.5 shows the temperature profile. The peak temperature rise is 19° C, assuming each transistor dissipates 50 mW. Back-side heat sinking results in a temperature rise less than half of the rise using edge heat sinking.

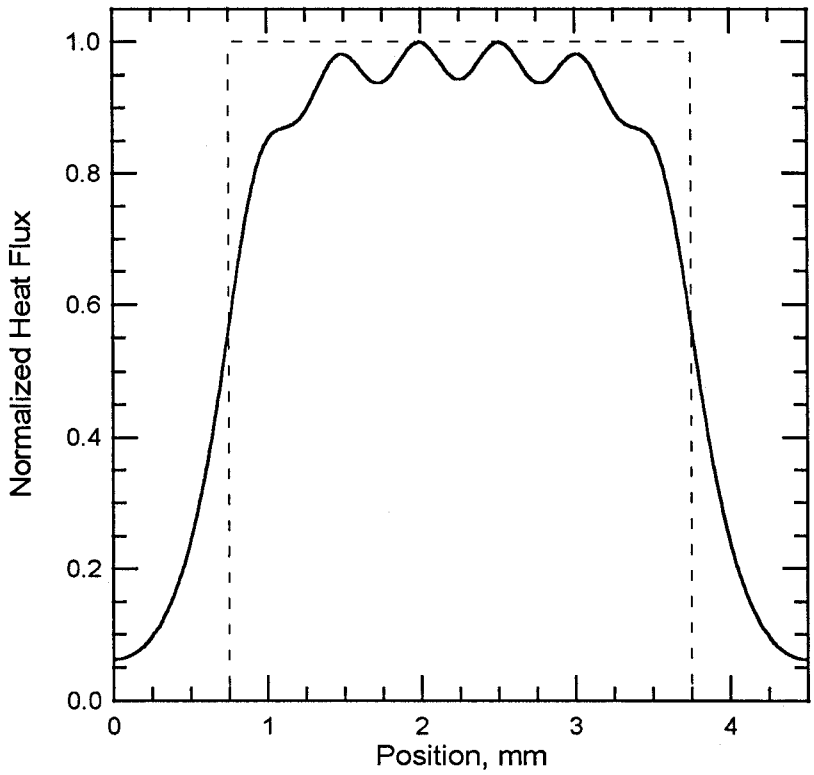

Fig. B.6. Normalized heat flux through the bottom of the array. Most of the heat flows through a square area, 3 mm on a side.

We still need to calculate the temperature rise of the carrier. This can be done using the modelling developed for edge heat sinking. The normalized heat flux through the bottom surface of the grid into the carrier is shown in Fig. B.6. A simple, yet accurate, approximation to this distribution is a uniform heat flux through a square area, 3 mm on a side. This is also plotted in Fig. B.6 for comparison. The carrier must be made out of a material that is a good thermal conductor, but a poor electrical conductor to avoid attenuating the microwave beam. An ideal candidate is diamond, which is now being commercially grown and sold at reasonable prices. Fig. B.7 shows the temperature profile at the top surface of the diamond carrier. The carrier is 5 mm on a side and 0.5 mm thick, with a thermal conductivity of 1000 W/m/°C [4]. The peak temperature rise is only 1.2° C, assuming 3.6 W of total dissipated power.

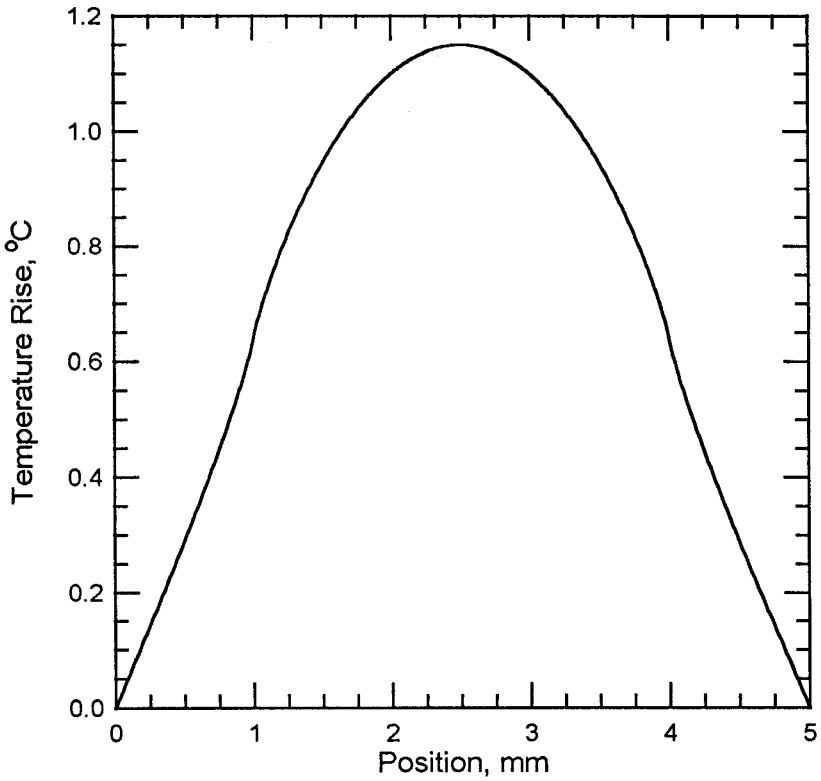

Fig. B.7. Temperature profile for a section through the center of the diamond carrier. The peak temperature is 1.2°C, assuming a total power dissipated of 3.6 W.

Material	Thermal Cond. k W/m/°C	Thickness c mm	Temp. Rise °C/W
Diamond	≈1000	0.5	0.32
Aluminum Nitride	170	1	1.1
Silicon	150	1	1.3
Quartz	12	1	15.8
Duroid 6010	0.4	1.5	386

Table B.1. Comparison of carriers using various materials. Thermal conductivity data obtained from [3–7].

Table B.1 compares the modelled temperature rises of carriers made from various materials. Assuming a total dissipation of 3.6 W, the diamond, aluminum nitride, and silicon carriers would not heat more than 5° C. This would keep the total heat rise for the grid and carrier less than 25° C. Quartz is a rather poor thermal conductor, and using Duroid is out of the question.

This simple example illustrates an important point. Thermal issues need to be considered in the design of quasi-optical devices, even for relatively small arrays. For large grids, incorporating hundreds or thousands of devices, these issues will become paramount.

References

[1] J.B. Hacker, M.P. DeLisio, M. Kim, C.-M. Liu, S.-J. Li, S.W. Wedge, D.B. Rutledge, "A 10-Watt X-Band Grid Oscillator," *1994 IEEE MTT-S Int. Microwave Symp. Dig.*, pp. 823–826, 1994.

[2] R.P. Feynman, R.B. Leighton, M. Sands, *The Feynman Lectures on Physics*, vol. II, Addison-Wesley Publishing Co., Reading, MA, 1964, chap. 3.

[3] S.M. Sze, *Physics of Semiconductor Devices*, second ed., John Wiley & Sons, Inc., New York, 1981, pp. 850–851.

[4] Norton Diamond Film Corp., *Diamond Film Specifications*, Northboro, MA.

[5] Carborundum Microelectronics, *Aluminum Nitride Specifications*, Phoenix, AZ.

[6] Rogers Corp., Microwave Materials Division, *Product Selector Guide*, Chandler, AZ.

[7] L.H. Van Vlack *Elements of Materials Science and Engineering*, fifth ed., Addison-Wesley Publishing Co., Reading, MA, 1985, pp. 612–613.